AFRL-MN-EG-TR-1998-7044

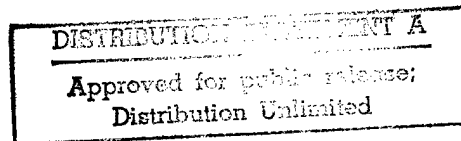# Analytical Modeling of High Rate Processes

Stanley E. Jones
University of Alabama
Tuscaloosa, AL 35487-0276

Peter P. Gillis
University of Kentucky
Lexington, KY 40506-0046

CONTRACT NO. F08630-93-K-0011

December 1997

FINAL REPORT FOR PERIOD December 1992- April 1996

DISTRIBUTION - Approved for public release

19980626 039

AIR FORCE RESEARCH LABORATORY, MUNITIONS DIRECTORATE

Air Force Materiel Command ■ United States Air Force ■ Eglin Air Force Base

DTIC QUALITY INSPECTED 1

NOTICE

When Government drawings, specifications, or other data are used for any purpose other than in connection with a definitely Government-related procurement, the United States Government incurs no responsibility or any obligation whatsoever. The fact that the Government may have formulated or in any way supplied the said drawings, specifications, or other data, is not to be regarded by implication, or otherwise as in any manner construed, as licensing the holder, or any other person or corporation; or as conveying any rights or permission to manufacture, use, or sell any patented invention that may in any way be related thereto.

The technical report has been reviewed and is approved for publication.

FOR THE COMMANDER

AARON D. BRINSON
Technical Director, Ordnance Division

RUSS KLUG, Program Manager
Damage Mechanisms Branch

Even though this report may contain special release rights held by the controlling office, please do not request copies from the Air Force Research Laboratory, Munitions Directorate. If you qualify as a recipient, release approval will be obtained from the originating activity by DTIC. Address your request for additional copies to:

Defense Technical Information Center
Attn: DTIC-OCA (Acquisitions)
8725 John J. Kingman Rd., Suite 0944
Ft Belvoir, VA 22060-6218

If your address has changed, if you wish to be removed from our mailing list, or if your organization no longer employs the addressee, please notify AFRL/MNMW, Eglin AFB FL 32542-6810, to help us maintain a current mailing list.

ii

REPORT DOCUMENTATION PAGE		Form Approved OMB No. 0704-0188

Public reporting burden for this collection of information is estimated to average 1 hour per response, including the time for reviewing instructions, searching existing data sources, gathering and maintaining the data needed, and completing and reviewing the collection of information. Send comments regarding this burden estimate or any other aspect of this collection of information, including suggestions for reducing this burden, to Washington Headquarters Services, Directorate for Information Operations and Reports, 1215 Jefferson Davis Highway, Suite 1204, Arlington, VA 22202-4302, and to the Office of Management and Budget, Paperwork Reduction Project (0704-0188), Washington, DC 20503.

1. AGENCY USE ONLY (Leave blank)	2. REPORT DATE 1997 December	3. REPORT TYPE AND DATES COVERED Final Report, December1992 – April 1996

4. TITLE AND SUBTITLE Analytical Modeling of High Rate Processes	5. FUNDING NUMBERS C: F08630-93-K-0011 PE: 62602F PJ: 2502 TA: 06 WU: 88
6. AUTHOR(S) Stanley E. Jones, Peter P. Gillis	

7. PERFORMING ORGANIZATION NAME(S) AND ADDRESS(ES) University of Alabama University of Kentucky Tuscaloosa, AL Lexington, KY 35487-0276 40506-0046	8. PERFORMING ORGANIZATION REPORT NUMBER

9. SPONSORING/MONITORING AGENCY NAME(S) AND ADDRESS(ES) Air Force Research Laboratory, Munitions Directorate Ordnance Division Damage Mechanisms Branch (AFRL/MNMW) 101 W. Eglin Blvd., Ste 239 Program Manager, Russ Klug Eglin AFB, FL 32542-6810 (850) 882-9643 x202	10. SPONSORING/MONITORING AGENCY REPORT NUMBER AFRL-MN-EG-TR-1998-7044

11. SUPPLEMENTARY NOTES

12a. DISTRIBUTION/AVAILABILITY STATEMENT Public release.	12b. DISTRIBUTION CODE

13. ABSTRACT (Maximum 200 words)
Modeling of terminal ballistic events requires accurate constitutive data at strain-rates exceeding 10^4/sec and at high strains. The Split-Hopkinson Pressure Bar can provide information in both tension and compression at high strains, but is limited in strain-rate by the elastic wave speed in the bars. It is generally accepted that 10^4/sec is the limit of such devices. Strain-rates that exceed 10^4/sec can be easily achieved in the Taylor impact test. The question that remains is how to best extract information from that test. The work performed on this project extends and revises prior efforts to deduce the constitutive properties of ductile metals with one-dimensional analyses. The problem is approached from several perspectives: engineering modeling, dislocation-based mechanics, shock physics, and computational mechanics. In all cases there are similar conclusions and the basis for reasonable constitutive modeling using the Taylor impact test has been established.

14. SUBJECT TERM Plasticity, High Strain Rate, Mechanical Strength, Elongation, Taylor Impact Experiments	15. NUMBER OF PAGES 141
	16. PRICE CODE

17. SECURITY CLASSIFICATION OF REPORT UNCLASSIFIED	18. SECURITY CLASSIFICATION OF THIS PAGE UNCLASSIFIED	19. SECURITY CLASSIFICATION OF ABSTRACT UNCLASSIFIED	20. LIMITATION OF ABSTRACT UL

NSN 7540-01-280-5500

Standard Form 298 (Rev. 2-89)
Prescribed by ANSI Std. 239-18

Table of Contents

1.0 Executive Summary

The most critical element in high-rate, plastic deformation of crystalline solids is the motion of dislocations. During the contract period, a great deal of attention was focused on this subject with particular emphasis on how dislocation motion should be incorporated into material constitutive equations. Results from these efforts appear in reference 1 (see Appendix A). This presents successful applications of dislocation-based, rate-dependent, plasticity theory to some simple, one-dimensional problems. It is suggested that such theory be incorporated into a finite element code such as EPIC so that more complex problems could be treated in the future.

Most of the work performed under this contract involved novel analytical models to interpret the results from Taylor impact tests. In reference 2 (see Appendix B), the difference between the original Taylor theory and the so-called "alpha-beta theory" is examined. The latter requires solving a highly complex, transcendental equation in order to obtain a flow stress estimate from the Taylor test. Reference 2 establishes an empirical constant that simplifies the "alpha-beta theory" to a formula comparable to that of Taylor. This makes it simple to now estimate the flow stress from an ordinary Taylor test using the "alpha-beta theory."

A trilogy of papers by: Foster, Maudlin, and Jones (reference 3, see AppendixC), Jones, Maudlin, and Foster (reference 4, see AppendixD), and Maudlin, Foster, and Jones (reference 5, see AppendixE) present analyses of the Taylor test from three

different viewpoints. Reference 3 examines the Taylor test from the viewpoint of one-dimensional shock wave propagation. Reference 4 considers the Taylor test as a one-dimensional engineering problem. Reference 5 presents a computational approach to the problem based on a finite element code. These three views and their outcomes are compared and contrasted in the papers. Remarkably, the elementary shock physics and engineering modeling produce identical results and the computational mechanics code analysis confirms these conclusions.

Within the aforementioned papers are the elements of a theory that is capable of describing material behavior at very high strain-rates and strains. This information is required for the successful simulation of terminal ballistic events. In these papers are representations for stress

$$\sigma = (1+e)(\sigma_0 + \frac{\rho}{e}(v_0^2 - u)^2)$$

and an equation of motion for the undeformed section of the Taylor specimen

$$\rho \ell \dot{v} = \sigma_0$$

that were not previously reported in their present forms. The definitions and interpretations of all of the symbols appearing in these equations are given in Appendices C, D, or E. The potential application of these results and some of the

companion kinematical equations to constitutive modeling of high strain-rate behavior of ductile materials is enormous.

A summary, and an example, of the one-dimensional analysis is given in reference 6 (see Appendix F). At the same time, a new estimate for the maximum strain-rate achieved in the test after initial transient behavior is completed is also included. Estimating the strain-rate from test data is the most challenging aspect of the modeling effort. Work continues on this problem and the results of reference 7 give some indication of the ultimate reward that is possible from these efforts. Jones, Allen, Sharp, and Foster (reference 7, see Appendix G) present an implicit, parametric representation of the constitutive equation for ductile isotropic metals. The parameter in the representation was the undeformed section speed in the Taylor specimen. The methods presented in these papers show great promise for mapping Taylor test results that are recorded by high speed photography, into stress, strain, strain-rate information. This would facilitate the construction of accurate material constitutive relations for use in numerical design simulations.

Reference 8 (see Appendix H) provides internal void formation data from actual Taylor tests. This, in turn, provides a physical foundation for constitutive models that include material damage parameters. It would be very worthwhile to extend this work to other materials in addition to copper.

Besides the Taylor test effort, analytical modeling of penetration experiments was emphasized. In references 9-12 (see Appendices I-L), the Alekseevskii-Tate theory of long rod penetration into a semi-infinite target was perturbed in several novel and interesting ways to improve the degree of agreement with previously reported experimental results. The emphasis in all of these papers was the simplicity of an engineering model. In some instances, the interpretation was through transient rather than steady-state behavior.

The work discussed above was enhanced by presentations at national and international technical meetings. Below are listed the presentations that were made in connection with the project. The presentor is listed in parentheses after the citation.

1. "The Role of Dislocations in High Rate Plasticity," Second Wright Laboratory/Air Force Office of Scientific Research Workshop on Integrated Theory and Numerics for Design Applications, Eglin AFB, FL, June, 1994 (P.P. Gillis).

2. "An Analysis of Plastic Wave Propagation in Taylor Impact Specimens," Second Wright Laboratory/Air Force Office of Scientific Research Workshop on Integrated Theory and Numerics for Design Applications, Eglin, AFB, FL, June, 1994 (S.E. Jones).

3. "Dislocation Theories of Viscoplasticity," Symposium on Finite Deformation Viscoplasticity, International Mechanical Engineering Congress and Exposition, Atlanta, GA, November, 1995 (P.P. Gillis).

4. "Estimation of Flow Stress Under High Rate Plastic Deformation," Fall Meeting of TMS-AIME, Pittsburg, PA, October, 1993 (J.W. House).

5. "An Analysis of One-Dimensional Penetration Using a Revised Estimate for Impulse," SECTAM XVII, Hot Springs, AR, April, 1994 (S.E. Jones).

6. "An Elementary Theory of One-Dimensional Rod Penetration Using a New Estimate for Pressure," 31st Annual Technical Meeting of the Society of Engineering Science, College Station, TX, invited paper, November, 1994 (S.E. Jones).

7. "On the Taylor Test: A Continuum Analysis of Plastic Wave Propagation," APS Topical Conference on Shock Compression of Condensed Matter, Seattle, WA, August, 1995 (J.C. Foster, Jr.).

8. "Constitutive Modeling Using the Taylor Impact Test," ASME Conference and Exposition (WAM), San Francisco, CA, invited paper, November, 1995 (S.E. Jones).

9. "A Parametric Representation for the Constitutive Properties of Metals at High Strain-Rates," IMACS'94, 14th World Congress on Computational and Applied Mathematics, Atlanta, GA, July, 1994 (S.E. Jones).

As college professors, one of our most important functions is the direction of graduate student research. In this connection, three students at the University of Alabama received advanced degrees with work directly or indirectly associated with the project. One student was partially supported by project funds and another was entirely supported by funds from the Air Force Office of Scientific Research through an augmentation grant (Project ASSERT). Below is a list of the students and their degrees:

1. Dr. Ping Wang, received a Ph.D. in Engineering Science and Mechanics in May, 1994. Dr. Wang's work was in the area of one-dimensional modeling of penetration. The title of his dissertation was "An Investigation of One-Dimensional Penetration Modeling." Dr. Wang received no project support.

2. Mr. David Allen received an M.S. in Engineering Science and Mechanics in December, 1995. Mr. Allen's work was in the area of Taylor test analysis using the EPIC code. He spent a summer at Los Alamos National Laboratory. The title of his thesis was "Use of the Taylor Impact Test to Determine Constants for Material Strength Models." Mr. Allen was partially supported with project funds.

3.   Mr. Sandor Augustus received an M.S. in Engineering Science and Mechanics in May, 1996. Mr. Augustus' work was in the area of one-dimensional modeling of the Taylor test. Mr. Augustus spent a summer at Eglin AFB. The title of his thesis was "Validation of an Elementary Scaling Law in the Taylor Test for 6061-T6 Aluminum." Mr. Augustus was supported by an Air Force Fellowship from the Air Force Office of Scientific Research through an augmentation grant (project ASSERT).

THIS PAGE BLANK

2.0 Conclusions

This project has lead to some important discoveries that provide very useful tools for the determination of the high rate properties of ductile materials. Listed below are the principal conclusions and their potential use for solving the important materials characterization problem connected with high rate deformation.

1. The related papers (references 3-5) present a new set of equations that interpret the Taylor impact test from the perspective of a plastic wave propagation problem. One interpretation of these results is the propagation of waves of constant strain. When viewed in this context, the kinematical equations can be integrated and a useful scaling law is produced. This relationship takes the form

$$\frac{\ell_f}{L} = -\frac{1-\beta}{e}\frac{L_f}{L} + \frac{\bar{\ell}}{L} - \frac{1-\beta}{e}\frac{\bar{s}}{L} + \frac{1-\beta}{e}$$

where all of the parameters that appear in this equation involve post-test measurements of recovered Taylor specimens or quantities that can be determined from the theory. Mr. Sandor Augustus extensively investigated this relationship for 6061-T6 Aluminum and found that for impact velocities that are sufficiently high it is valid. The implication from this conclusion is that the important physical parameter β can now be determined from the slope of the line in the ℓ_f/L vs. L_f/L space. The details of this reasoning are contained in Mr. Augustus' thesis.

9

The work mentioned above appears to provide the framework for a theory that will be capable of estimating stress states in ductile metals at high strain-rates. It also appears that this theory will be capable of providing these estimates for other materials, such as polymers or even energetic materials, for which there is no recovered impact specimen. We recommend that this work be extended and continued.

2. A substantial effort was undertaken to develop an alternative and independent path to the state of stress in ductile materials. This involved the EPIC code. Mr. David Allen installed the EPIC code on a PC and an IBM Workstation. The purpose of this was to explore the development of new techniques for reducing Taylor test data using the code. His work concentrated on estimating Johnson-Cook strength constants using only Taylor test data. The results presented in his thesis are only preliminary, but it appears that this effort is worth pursuing and we recommend so.

3. Dr. Ping Wang thoroughly investigated alternatives in the one-dimensional mathematical modeling of penetration by eroding rods into semi-infinite targets. This work was not supported by the Air Force, but was related to their interests and is mentioned here for that reason. Dr. Wang proposed several fundamental improvements in earlier modeling efforts. These improvements concerned the impulse of the force at the interface between the deformed and undeformed sections of the rod penetrator and the pressure at the target/penetrator interface. The agreement between theory and experiment was considerably improved and his work resulted in several publications in prominent conference proceedings and a journal. This work has reached the point where it appears

that any improvements will not be substantial without some inspirational change in

thinking. We do not recommend continuing this effort any further.

THIS PAGE BLANK

References

1. Peter P. Gillis, "Dislocation Theories of Viscoplasticity," Proceedings of the ASME Materials Division, Volume 1, R.C. Batra, T.W. Wright, G.S. Bhat, and T.S. Srivatsan, eds. (Symposium on Finite Deformation Plasticity), p.493 (1995), (see also Peter P. Gillis, "The Role of Dislocations in High Rate Plasticity," Minutes of the Second WL/AFOSR Workshop on Integrated Numerics for Design Applications, Volume 1 (1994).).

2. Joel W. House, John C. Lewis, Peter P. Gillis, and L.L. Wilson, "Estimation of Flow Stress Under High Rate Plastic Deformation," *Int. J. Impact Engng.*, 16, 189 (1995).

3. J.C. Foster, Jr., P.J. Maudlin, and S.E. Jones, "On the Taylor Test: A Continuum Analysis of Plastic Wave Propagation," Proceedings of the 1995 Topical Conference on Shock Compression of Condensed Matter, Seattle, WA (1995).

4. S.E. Jones, Paul J. Maudlin, and Joseph C. Foster, Jr., "An Engineering Analysis of Plastic wave Propagation in the Taylor Test," *Int. J. Impact Engng.*, 19, 2, 95 (1997) (see also, Los Alamos National Laboratory Technical Report No. LA-12845-MS).

5. Paul J. Maudlin, J.C. Foster, Jr., and S.E. Jones, "A Continuum Mechanics Code Analysis of Steady Plastic Wave Propagation in the Taylor Test," *Int. J. Impact Engng.*, 19, 3, 231 (1997) (see also, Los Alamos National Laboratory Technical Report No. LA-12836-MS).

6. S.E. Jones, Paul J. Maudlin, and J.C. Foster, Jr., "Constitutive Modeling Using the Taylor Impact Test," ASME AD-Vol. 48, *High Strain Rate Effects on Polymer, Metal, and Ceramic Matrix Composites and Other Advanced Materials*, Y.D.S. Rajapakse and J.R. Vinson, eds. (1995).

7. S.E. Jones, David Allen, Scott Sharp, and Joseph C. Foster, Jr., "A Parametric Representation for the Constitutive Properties of Metals at High Strain-Rates," Proceedings of IMACS'94, 14th World Congress on Computational and Applied Mathematics, Atlanta, GA (1994).

8. Jessica L. Mayes, Stephen L. Hatfield, Peter P. Gillis, and Joel W. House, " Void Formation in OFE Copper," *Int. J. Impact Engng.*, 14, 503 (1993).

9. P. Wang and S.E. Jones, "An Elementary Theory of One-Dimensional Rod Penetration Using a New Estimate for Pressure," *Int. J. Impact Engng.*, 18, 3, 265 (1996).

10. Ping Wang and S.E. Jones, "An Analysis of One-Dimensional Penetration Using a Revised Estimate for Impulse," Proceedings of SECTAM XVII, Hot Springs, AR (1994).

11. S.E. Jones, Rhett B. Marlow, J.W. House, and L.L. Wilson, "A One-Dimensional Analysis of the Penetration of Semi-Infinite 1100-0 Aluminum Targets by Rods," *Int. J. Impact Engng.*, 14, 407 (1993).

12. Ping Wang and S.E. Jones, "An Elementary Theory of One-Dimensional Rod Penetration Using a New Estimate for Pressure," abstract in *Recent Advances in Engineering Science*, Proceedings of the 31st Annual Technical Meeting of the Society of Engineering Science, College Station, TX, p369 (1994).

APPENDIX A

DISLOCATION THEORIES OF VISCOPLASTICITY

Peter P. Gillis
Department of Chemical & Materials Engineering
University of Kentucky
Lexington, Kentucky

Crystalline materials that deform plastically do so mainly by the movement of line defects known as crystal dislocations. At high rates of deformation this is especially true. Grain boundary sliding may contribute a small amount of viscoplastic deformation in polycrystalline materials. However, when deformation rates are as high as in most technologically important processes (e. g., rolling, forging, stamping and extrusion), almost all of the deformation is accommodated by the motion of dislocation.

Two fundamental processes are important in crystal plasticity. The spatial and velocity configurations of the dislocation population determine local values of the plastic portion of the rate of deformation tensor. Also, the accumulation of plastic deformation reorients the polycrystalline grain structure. Thus, the accumulated motion of dislocations usually leads to texture formation in initially isotropic materials and texture redevelopment in anisotropic materials.

In the present paper these two processes are reviewed. Experimental evidence that relates the motion and number of dislocations to stress and strain is presented. With this background developed, analytic solutions incorporating dislocation dynamics, are reviewed for some simple, one- and two-dimensional problems. Finally, author suggests some general features for a computational scheme to incorporate the essential results of dislocation theory into multidimensional computer codes.

INTRODUCTION

Seminal papers by Taylor (1934), Orowan (1934), and by Polanyi (1934), introduced the concept of crystal dislocations into the science of the mechanics of deformable solids. Since then dislocation theory has become an important area of study by itself and has motivated many important advances in continuum mechanics.

One such advance has been to emphasize the intrinsically viscous nature of plastic deformation. Crystalline materials that deform plastically do so mainly by the glide movement of dislocations. At high rates of deformation this is especially true. It is simple to show geometrically that local plastic strain is the time integral of local dislocation flux. Because this flux is always finite, the accumulation of plastic strain is time dependent or viscous. The characteristic time associated with this viscosity has been so small that at low rates of deformation inviscid theories have successfully described the resulting plasticity. However, such theories become less successful as deformation rates increase.

Even before the concept of dislocations arose, the notion of slip band formation was associated with the plastic deformation of crystals. It was shown geometrically that homogeneous accumulation of strain on a single slip system reorients the crystal with respect to the loading direction (Schmid and Boas, 1935). A natural coupling should occur here with dislocation theory. In the many situations when slip is attributable to dislocation glide, the flux of glide dislocations then determines the rate of crystallographic reorientation as well as the rate of plastic straining. In principle, this would allow texture changes to be calculated from dislocation kinematics. In practice, no one seems to have attempted such a computation.

Local dislocation flux is a summation over all the different dislocation families of the product of density times velocity. The speeds are highly sensitive to the local stress state. The densities require evolutionary equations (Kelly and Gillis, 1974a) that account for cross glide multiplication events and stalemating of dislocations of one family by those of another as well as by grain and sub-grain boundaries and other crystal defects. Combine all this with compatibility and equilibrium conditions all the grain boundaries in polycrystal and an enormous computational problem results.

REVIEW
Dislocation Flux

The Burgers vector is the relative displacement produced by the motion of a dislocation across a glide plane. Figure 1 (taken from Gilman, 1969) shows a crystal element being traversed by a dislocation line. The upper portion of the element is being displaced relative to the lower portion by some natural crystallographic spacing, denoted by b. As the dislocation line sweeps out an ever increasing area of the glide plane the average displacement of the top surface of the element increases. When the entire area has been traversed the relative displacement is uniformly b. The plastically deformed configuration corresponds to a simple shear strain with respect to the coordinate directions b and n where n is normal to the plane of the dislocation. The plastic strain-rate is proportional to the rate at which the dislocation sweeps out area. In turn, this depends upon the length of the dislocation line and its average speed. The product of these two quantities is the dislocation flux. Its two components are extremely difficult quantities to probe experimentally.
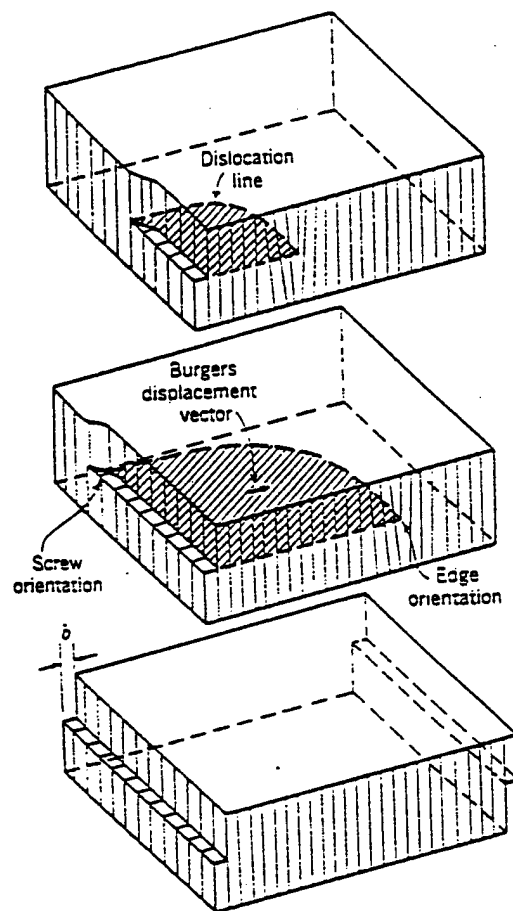
Figure 1. Spread of a glide dislocation across a crystallographic plane. (Gilman, 1969)

Dislocation Density

The length of dislocation line per unit volume of material is called dislocation density. The total dislocation density is often largely composed of dislocations whose motion is impeded by barriers of the types mentioned above. These are called immobile dislocations. Thus an important quantity in describing the plastic strain-rate is the mobile fraction of the total dislocation density.

Measurements of total dislocation density have been made using such techniques as electron microscopy , etch pits , and x-ray topography. See, for example, Eddington (1968), Johnston and Gilman (1959) and Pope, et al. (1967). Figure 2 shows experimental data of Eddington (1968) relating total dislocation density to plastic deformation from tension tests of niobium monocrystals. The density
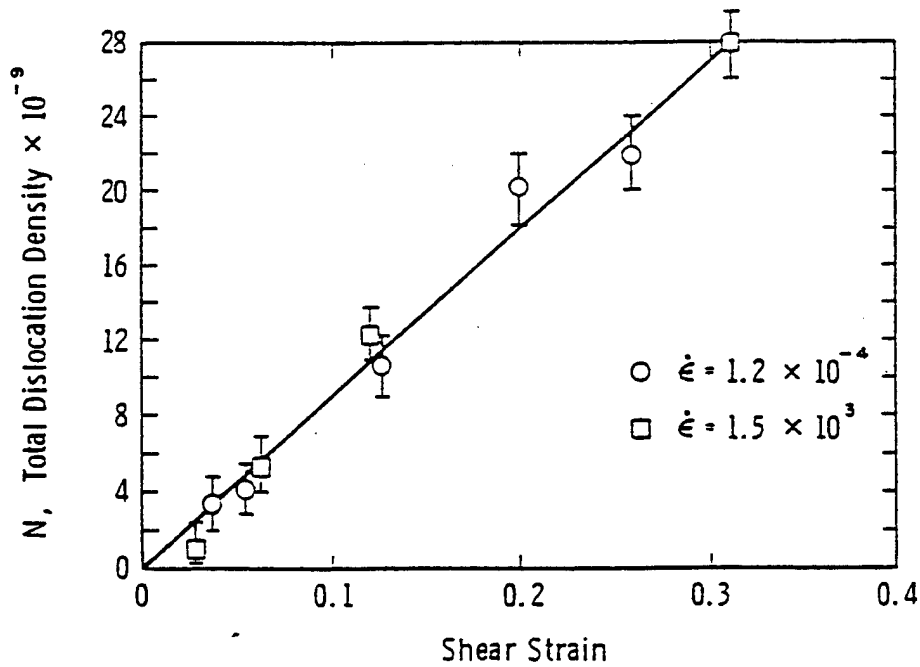
Figure 2. Dislocation density as a function of plastic deformation. (Eddington, 1968)

units in this figure are cm^{-2} or cm/cm^3. The data points near $10 \times 10^9 \, cm^{-2}$ represent dislocation line lengths of about 6,000 miles per cubic centimeter! The figure purports to show that for these experiments density varied with plastic strain but not with strain-rate. Analysis of some dozen other data sets by Keshavan and Gillis (1975) suggest that a simple linear dependence of density upon plastic strain is reasonably appropriate for other materials, including polycrystals.

Dislocation Speed

Measurements of mobile dislocation speeds have been made using etch pit and x-ray techniques. Figure 3 (due to Gilman, 1969) shows a compilation of speed versus applied stress for eight different

Figure 3. Some typical data showing the dependence of dislocation velocities on applied shear stress. (Gilman, 1969)

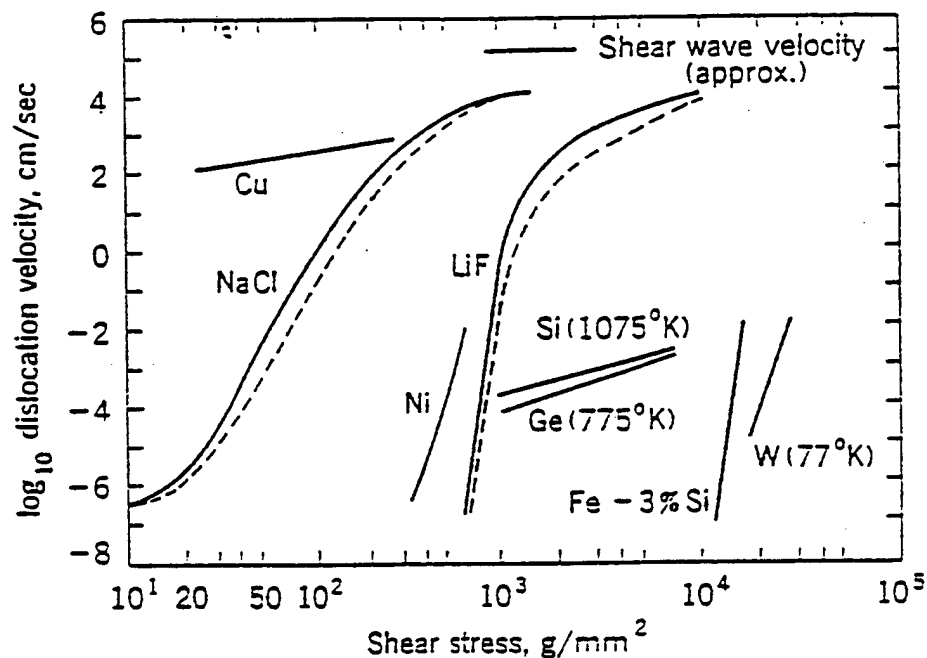materials in monocrystal form. The stress values represent shear on the glide plane in the direction of the Burgers vector. Note that both axes are scaled logarithmically. For germanium, silicon and copper the slopes are near unity while for the other five materials the slopes are extremely steep at low velocities. The alkali halides tend to level off as the shear wave velocity is approached.

High speed dislocations present a special challenge experimentally. Even as low as 100 cm/s a stress pulse duration of 0.1 s will displace a dislocation 10 cm which usually means it has passed out of the test specimen altogether. In order to retain the dislocations within the specimen so that changes of position can be measured, extremely short, dynamic stress pulses are required. The rise and decay times of these pulses then become important quantities that are especially difficult to assess.

Two features that characterize the data shown in Figure 3 are a limiting speed in the vicinity of the elastic shear wave velocity which dislocation speeds do not exceed, and a cut-off stress below which dislocations do not move. This second feature roughly corresponds to the yield strength of the material. Plastic deformation does not occur at stress levels below this cut-off stress. Furthermore, the yield strength at low deformation rates is not sensitive to the rate. In nickel, for example, according to the figure, dislocation speeds increase by about a factor of 35 as the stress increases from 400 to 500 (25 percent). For this stress increase the dislocation flux will increase more than 35 times because the slightly higher stress will drive additional dislocations into the initial mobile population and the already

higher flux will produce more new dislocations faster through the strain dependence of the dislocation density. Therefore, the yield stress will increase only moderately in response to very large increases in deformation rate.

On the other hand, at sufficiently high deformation rates the first feature mentioned above comes into play. At high dislocation speeds an asymptotic approach is made to the limiting speed. then the sensitivity of dislocation speed to stress rapidly declines. Larger stress increments are required for successive, equal increments of dislocation speed. As tests are conducted at higher deformation rates, significantly higher stresses are required to produce plastic deformation. Experimental results for plain carbon steels (taken from Kanninen et al., 1968) are shown in Figure 4 which illustrate this behavior. Figure 5 shows a theoretical calculation by Gillis (1965) based on a limiting-dislocation-speed model and it qualitatively reproduces the experimental trend.
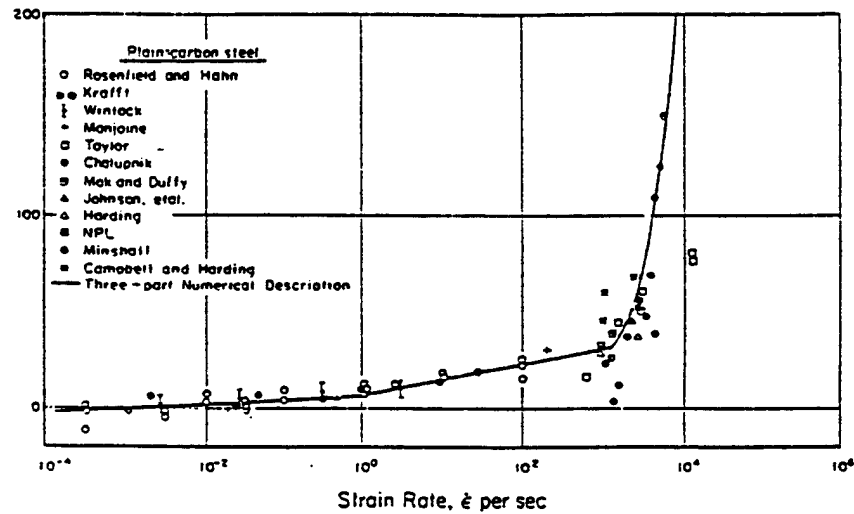

Figure 4. Data showing the strain rate dependence of the yield stress of steel at room temperature. (Kanninen et al., 1968)
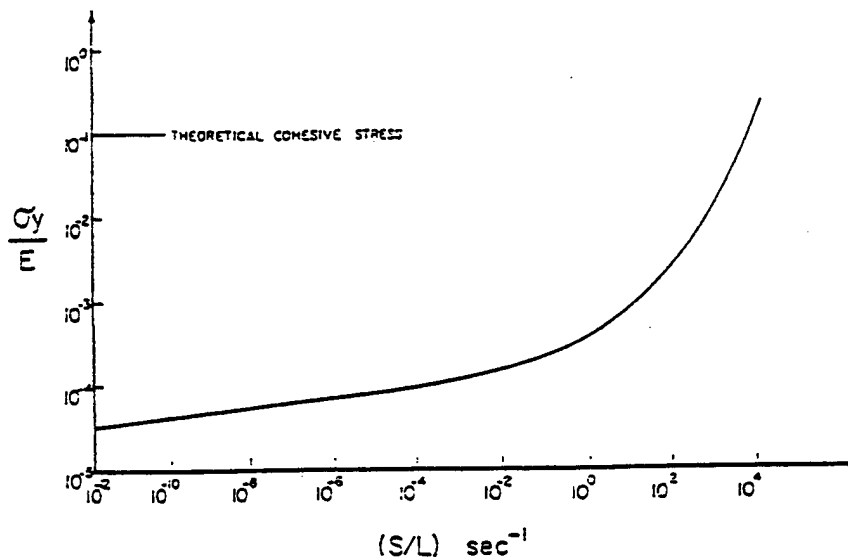
Figure 5. Calculated non-dimensional yield stress versus specific crosshead rate. (Gillis, 1965)

APPLICATIONS

The forgoing physics was the basis for several idealized descriptions of viscoplastic deformation (Gillis and Gilman, 1965, Gillis and Kelly, 1972). Several one dimensional problems were solved (Gillis and Kelly, 1973, Kelly and Gillis, 1967, 1974b, 1975, & 1977, Sackett et al., 1977, Gillis and Jones, 1977, Jones and Gillis, 1978) analytically or with computational schemes of varying degrees of complexity. Although inertia effects were not considered, some aspects of wave propagation were treated through elastic precursor decay and steady-state assumptions. These computations were all reasonably successful.

More modern trends are towards using finite element calculations to solve problems in plasticity and to employ dynamic codes whenever necessary. In these codes two requirements arise that could be naturally satisfied by a dislocation-based material constitutive relation. First is a natural viscosity that results from plastic strain requiring a finite time to accumulate. Potentially this could replace the artificial viscosity introduced into current codes arbitrarily to stabilize numerical wave fronts. Second is a natural method for calculating finite rotations as discussed in the foregoing Introduction.

An even more important computational concept coming from dislocation theories relates to the yield surface. Figure 3 shows that above the cut-off stress, the higher the applied stress the faster dislocations glide. And the faster they glide the larger is the plastic strain-rate. This suggests that the yield surface represent the cut-off stress, at or below which dislocations remain stationary. Plastic deformation then would require a stress state outside of the yield surface. The further outside, the larger would be the dislocation speed contributing toward plastic strain that would tend to relax the stress back into the yield surface. Everyone knows that is exactly what happens in reality. Dislocation dynamics merely provides a basis for assigning rates to these relaxation processes.

A-7

REFERENCES

Eddington, J.W., 1968, "Effect of Strain Rate on the Dislocation Substructure in Deformed Niobium Single Crystals," Mechanical Behavior of Materials Under Dynamic Loads, U.S. Lindholm, Editor, Springer-Verlag , New York, pp. 191-240.

Gillis, P.P.,1965, "Dislocation Dynamics and Strain Rate Effects," Journal of Applied Polymer Science, Applied Polymer Symposia, Vol 1, pp. 1-12.

Gillis, P.P., and Gilman, J.J., 1965, "Dynamical Dislocation Theory of Crystal Plasticity," Journal of Applied Physics, Vol. 36, pp. 3370-3386.

Gillis, P.P., and Jones, S.E., 1977, "Linearly Viscoplastic Material," Journal of Applied Physics, Vol. 48, pp. 2845-2849.

Gillis, P.P., and Kelly, J.M., 1972, "Ideal Viscoplasticity," Acta Metallurgica, Vol. 20, pp. 947-951.

Gillis, P.P., and Kelly, J.M., 1973, "An Ideally Viscoplastic Analysis of the Yield Point Phenomenon," Acta Metallurgica, Vol. 21, pp. 343-346.

Gilman, J.J., 1969, Micro Mechanics of Flow in Solids, McGraw-Hill.

Johnston, W.G., and Gilman, J.J., 1959, "Dislocation Velocities, Dislocation Densities and Plastic Flow in Lithium Fluoride Crystals," 1959, Journal of Applied Physics, Vol. 30, pp. 129-144.

Jones, S.E., and Gillis, P.P., 1978, "Upper Yield Points of Non-Linear Viscoplastic Materials," International Journal of Non-Linear Mechanics, Vol. 13, pp. 117-123.

Kanninen, M.F., Mukherjee, A.K., Rosenfield, A.r., and Hahn, G.T., 1968, "The Speed of Ductile Crack Propagation and the Dynamics of Flow in Metals," Mechanical Behavior of Materials Under Dynamic Loads, U.S. Lindholm, Editor, Springer-Verlag, New York, pp. 96-133.

Kelly, J.M., and Gillis, P.P., 1967, "Dislocation Dynamics and Precursor Attenuation," Journal of Applied Physics, Vol. 30, pp. 4044-4046.

Kelly, J.M., and Gillis, P.P., 1974a, "Thermodynamics and Dislocation Mechanics," Journal of the Franklin Institute, Vol. 297, pp. 59-74.

Kelly, J.M., and Gillis, P.P., 1974b, "Continuum Descriptions of Dislocations Under Stress Reversals," Journal of Applied Physics, Vol. 45, pp. 1091-1096.

Kelly, J.M., and Gillis, P.P., 1975, "The Influence of Limiting Dislocation Flux on the Mechanical Response of Polycrystalline Metals," International Journal of Solids and Structures, Vol 10, pp. 45-59.

Kelly, J.M., and Gillis, P.P., 1977, "An Ideally Viscoplastic Analysis of Shock Profiles,: Acta Mechanica, Vol 26, pp. 47--57.

Keshavan, M.K., and Gillis, P.P., 1975, "On Dislocation Multiplication," Journal of Physics F: Metal

Physics, Vol. 5, pp. 903-907.

Orowan, E , 1934, "Crystal Plasticity III, On the Mechanism of the Glide Process,: Zeitschrift for Physik, Vol 89, pp. 634-659.

Polanyi, M., 1934, "On a Kind of Glide Disturbance that Could Make a Crystal Plastic," Zeitschrift for Physik, Vol. 89, 660-664.

Pope, D. P., Vreeland, T. Jr., and Wood, D.S., 1967, "Mobility of Edge Dislocations in the Basal-Slip System of Zinc," Journal of Applied Physics, Vol. 38, pp. 4011-4018.

Sackett, S.J., Kelly, J.M., and Gillis, P.P., 1977, "A Probabilistic Approach to Polycrystalline Plasticity," Journal of the Franklin Institute, Vol. 304, pp. 33-63.

Schmid, E., and Boas, W., 1935, Kristallplastizitat, Springer Verlag, Berlin.

Taylor, G.I., 1934, "Mechanism of Plastic Deformation of Crystals," Proceedings of the Royal Society, Vol. A145, pp. 362-387.

APPENDIX B

Pergamon

ESTIMATION OF FLOW STRESS UNDER HIGH RATE PLASTIC DEFORMATION

JOEL W. HOUSE,† JOHN C. LEWIS,‡ PETER P. GILLIS‡
and L. L. WILSON†

†Wright Laboratory, Armament Directorate, Eglin Air Force Base, FL 32542 and ‡Materials
Science & Engineering, University of Kentucky, Lexington, KY 40506, U.S.A.

Summary—The impact of a cylindrical specimen against a rigid anvil was analysed in 1948 by G. I. Taylor. In 1987, Jones, Gillis and Foster proposed a modification to Taylor's analysis. This modification included a new equation of motion for the undeformed section of the specimen and relaxed one of the assumptions of Taylor's original work. While Jones and co-authors were able to show the existence of an exact solution. the utility of the analysis was severely limited by its complexity. The present paper introduces an approximation into this model which produces a simple algebraic formula to estimate its exact solution. Results of 92 tests of copper, aluminum and steel specimens are reported and used to evaluate this new approximation to the Jones, Gillis and Foster analysis.

NOTATION

A_0 cross-sectional area of the undeformed section
A cross-sectional area of the specimen just inside the plastic zone
C constant plastic wave speed
f experimentally determined parameter
F force exerted by the deformed material
h distance from the anvil face to the plastic wave front
H distance from the anvil face to the plastic wave front at final time
L original specimen length
L_1 final specimen length
S constant flow stress
t time
T final time
u undeformed section speed
U impact speed
u_p particle velocity just inside the plastic region
v speed of the plastic wave front
x length of the undeformed region
X final undeformed section length
ρ mass density of specimen
ψ function representing t as a function of u
$\cdot$ differentiation with respect to time

INTRODUCTION

In 1948 an analysis of the impact of a long rod on a rigid boundary was presented by Taylor [1]. His simple, one-dimensional analysis produced an approximation to the plastic flow stress in what is often called the Taylor anvil test. This test consists of launching a cylindrical projectile and having it impact normally against a hardened, massive target. Today, researchers are using complex continuum codes to simulate this test, calculating the large plastic deformations occurring in the rod and the elastic deformations occurring in the rod and anvil. Despite this fact, simple models such as Taylor's are still in use because their simplicitiy provides a special insight into how the physical parameters affect the event.

For this reason, they can be used to provide a basis for the improvement of continuum code calculations and for devising test matrices.

Since his original analysis, many attempts have been made to improve upon Taylor's one-dimensional theory. Hawkyard [2] for example, replaced one of Taylor's momentum equations by an energy balance, leading to somewhat different features in his final results. A fairly concise review of work up to 1983 can be found in the second half of a paper by Hutchings [3]. A more recent modification proposed in 1987 by Jones *et al.* [4] may be referred to as the "$\alpha\beta$ model". This analysis showed that it was possible to relax one assumption made by Taylor and to carry the algebra through to a solution that was "exact" within the framework of the remaining Taylor postulates. However, its usefulness is severely limited by its greater complexity. Unlike the simple algebraic formula obtained by Taylor, the $\alpha\beta$ computational procedure requires finding the solution to a highly non-linear, transcendental equation. The present paper introduces an approximation into the $\alpha\beta$ model that reproduces the simplicity of an algebraic formula achieved by Taylor and provides an exellent approximation to the exact $\alpha\beta$ solution.

THEORY

The notation used in this paper follows that of Taylor [1] wherever possible. Jones *et al.* [4] adopted different notation for the same quantities. With this in mind, consider a rod, initially circularly cylindrical with cross-sectional area A_0 and length L, impacting a massive anvil at an initial longitudinal velocity U. Assume that the rod material is rigid, perfectly plastic with a flow stress S, and that the anvil is rigid. This situation is shown schematically in Fig. 1. Part (a) shows the rod at the moment of impact (time, $t = 0$). Part (b) shows the rod at some later time as it is deforming against the anvil. Here, the plastic wave front (which is shown in the figure as a discontinuity in the cross-section of the rod) has moved a distance h from the anvil, the undeformed rod length is now x, and the remaining velocity of this undeformed section is u. Part (c) shows the rod at the conclusion of the event (time, $t = T$). Here, h and x have reached their final values of H and X, respectively; the rod cross-section no longer has a discontinuity; and the undeformed section of the rod has just come to rest ($u = 0$). The final overall length of the rod is denoted by L_1, where
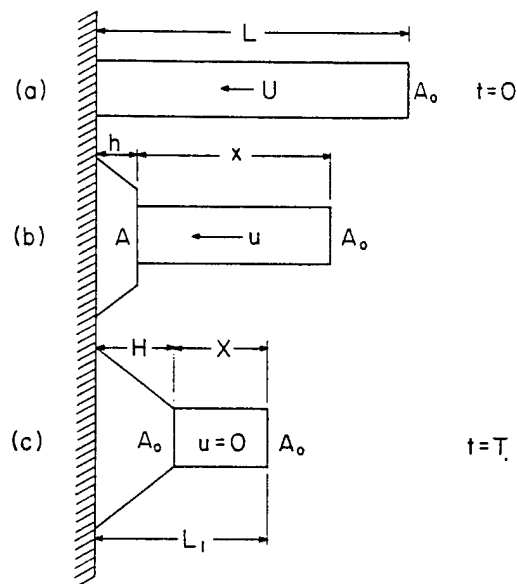
$$L_1 = H + X. \tag{1}$$

Fig 1. Schematic illustration of a projectile impacting a rigid anvil. The notation used in the paper is indicated in the figure.
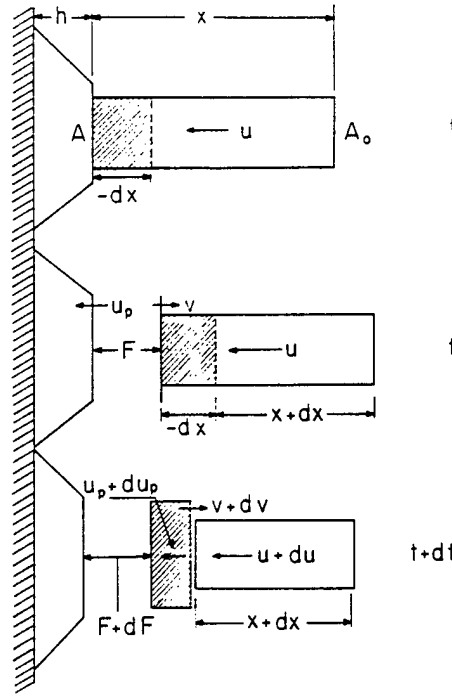
Fig. 2. Schematic illustration of a Taylor impact specimen at two different times during impact. The notation used for velocities and forces are indicated.

With reference to Fig. 2, consider the foremost section of undeformed rod of length $-dx > 0$ at some time t ($0 < t < T$). This rod element passes from the rigid portion into the plastic zone during a time interval dt and it undergoes discontinuous changes: velocity from u to u_p and cross-sectional area from A_0 to A. Here u_p is the particle velocity of the material just inside the plastic zone. Denote the mass density of the material by ρ, which is assumed to remain constant during plastic deformation. Denote the Eulerian velocity with which the plastic wave front is moving away from the anvil by $v = dh/dt$, and denote the force exerted by the previously deformed material as F.

During the time interval dt, the change in linear momentum of the previously undeformed rod must equal the net impulse. Thus

$$\rho A_0 x u - \rho A_0 (x + dx)(u + du) + \rho A_0 dx(u_p + du_p) = 1/2(2F + dF)dt. \tag{2}$$

Dividing through by $\rho A_0 dt$ and eliminating higher order differential terms gives

$$-x\dot{u} - \dot{x}u + \dot{x}u_p = F/(\rho A_0), \tag{3}$$

where superposed dots signify first derivatives with respect to time. Denote the dynamic flow stress of the rod material by S, then $F = SA$ and Eqn (3) can be rewritten

$$-(S/\rho)(A/A_0) = \dot{x}(u - u_p) + \dot{u}x. \tag{4}$$

Equation (4) may be further modified by taking into account conservation of mass. Consider again the foremost rod element originally shown in Fig. 2. Now, with reference to Fig. 3, the initial length of this element can be written $-dx = (u + v)dt$. This leads to the kinematic relation
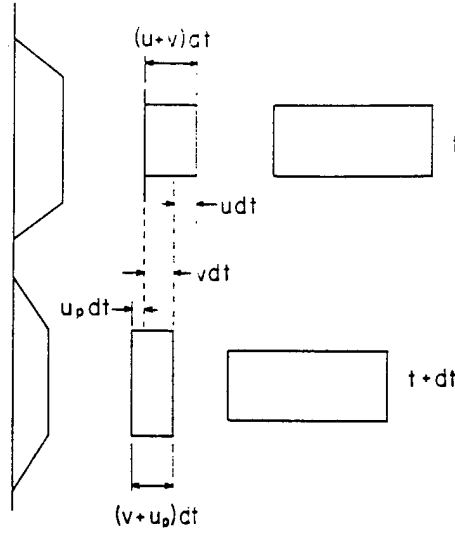
$$\dot{x} = -(u + v). \tag{5}$$

B-3

Fig. 3. Schematic illustration of a Taylor impact specimen at two different times during impact. Changes in the rod position are indicated.

From the figure, it is clear that the deformed length of the rod element is $(v + u_p)dt$. Thus, conservation of mass requires that

$$\rho A_0(u + v)dt = \rho A(v + u_p)dt, \tag{6}$$

which gives the relation

$$A/A_0 = (u + v)/(v + u_p). \tag{7}$$

Using Eqns (5) and (7) in Eqn (4) leads to the expression

$$-(S/\rho)(u + v)/(v + u_p) = -(u + v)(u - u_p) + \dot{u}x. \tag{8}$$

In the $\alpha\beta$ model, as well as in the Taylor model, the rod material is assumed to come to rest immediately upon entering the plastic zone, $u_p = 0$, and the plastic wave speed is assumed to be a constant, $v = C$. Making these changes in Eqn (8) and rearranging gives

$$x\dot{u} = u(u + C) - (S/\rho)(u + C)/C. \tag{9}$$

This equation is precisely the same (except for notation) as Eqn (15) of the $\alpha\beta$ analysis.

Time can be eliminated from Eqn (9) as the independent variable by using the chain rule of differentiation and Eqn (5) to obtain

$$x\,du/dx = -u + S/(\rho C). \tag{10}$$

In this form the variables are easily separated to give the following integral form

$$\int_L^x dx/x = -\int_U^u du/[u - S/(\rho C)]. \tag{11}$$

This equation is equivalent to the $\alpha\beta$ Eqn (20).

The $\alpha\beta$ solution is obtained as follows. First, solve Eqn (11) for x as a function of u (noting that S is a constant due to the assumed material characterization). Use the resulting function to eliminate x from the differential Eqn (9) in which the variables u and t are then

separable, so the equation can be integrated to obtain t as a function of u, say $\psi(u)$. Set $u=0$ in that equation to obtain the final time $T=\psi(0)$. Lastly, note that (for constant plastic wave velocity) $H=CT$ so that from Eqn (1)

$$T=(L_1-X)/C. \tag{12}$$

Equating $\psi(0)$ to Eqn (12) enables C to be determined. However, it is a complex procedure because C appears in $\psi(0)$ in quadratic and logarithmic forms. Thus, the solution procedure requires lengthy numerical calculations based upon some procedure such as interval halving. This paper will not discuss the $\alpha\beta$ solution in any additional detail. Instead, a simplified approximate solution will now be presented.

ANALYSIS

As in the $\alpha\beta$ solution, integrate Eqn (11) to obtain the following expression for x as a function of u:

$$\ln(x/L)=\ln\left[(S/(\rho C)-U)/(S/(\rho C)-u)\right]. \tag{13}$$

At the final time T, $u=0$ and $x=X$; thus

$$X/L=1-\rho UC/S, \tag{14}$$

which can be rearranged and written as

$$S/\rho=UC/(1-X/L). \tag{15}$$

In Eqn (15), ρ, U, X and L are known, but it would be difficult to guess the value of C. It proves somewhat easier to deal with the final time T. To this end, rearrange Eqn (12) to obtain

$$C=(L_1-X)/T. \tag{16}$$

Substitution into Eqn (15) yields

$$S/\rho=(U/T)L(L_1-X)/(L-X), \tag{17}$$

with only the time of the event, T, being unknown.

A fundamental geometric relation that involves the time of the event is

$$L-L_1=\int_0^T u(t)\,dt. \tag{18}$$

A simple approach to solving this integral is to assume linear deceleration of the impacting rod, $u(t)=U(1-t/T)$, which yields the solution $L-L_1=UT/2$. Taylor used this approach in his first approximate solution. Another approach is to use Eqns (5), (9) and (12) to determine the exact solution. But this leads to the complex $\alpha\beta$ result. An intermediate approach is to represent the integral in Eqn (18) by the expression

$$\int_0^T u(t)\,dt=fUT, \tag{19}$$

where f is some fraction such that $0<f<1$. In the case of linear deceleration, $f=1/2$. This representation is shown as the center curve in Fig. 4. On physical grounds, it is assumed $u(t)$ is a monotonically decreasing function in the interval $(0,T)$ with no points of inflection.
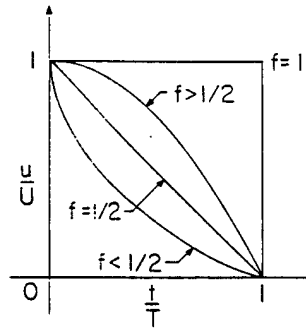
Fig. 4. Possible shapes of the remaining rod velocity vs time curve for different values of f.

Table 1. Static material properties

Material	Density $(g\,cm^{-3})$	Yield strength (MPa)	Ultimate strength (MPa)	Strain failure $(\%)$
OFE Copper (as received)	8.95	—	350	17
DPTE Copper (as received)	8.95	—	300	13
6061-T6 Aluminum	2.70	315	340	18
2024-T4 Aluminum	2.70	400	500	23
4340 Low strength steel	7.86	830	—	24

Two other curves are shown in the figure corresponding to $f<1/2$ and $f>1/2$. Also shown is the limiting case $f=1$.

Substituting from Eqn (19) for the integral in Eqn (18) leads to

$$T=(L-L_1)/(fU). \tag{20}$$

This expression for the time of the event can then be substituted into Eqn (17) to obtain the final relation

$$S/(\rho U^2)=f[L(L_1-X)]/[(L-X)(L-L_1)]. \tag{21}$$

This relation will reproduce the $\alpha\beta$ solution for a given impact test if the correct value of f is known.

EXPERIMENTAL

Five materials were tested in a matrix which included 92 experiments. These materials are listed in Table 1 with their statically measured mechanical properties and densities. Rod stock of each material was machined to a diameter of 7.595 mm. Various lengths were cut giving L/D ratios ranging from 1.5 to 10. These specimens were launched from a powder gun at a stand-off distance of 50–100 mm from the target. The target was a right circular cylinder with a diameter of 22.9 cm constructed of 4340 steel heat-treated to a hardness of R_c 58.

The experiments were instrumented to determine the velocity of impact by three different techniques. One method involved using pressure taps along the barrel to measure time of arrival at points near the muzzle. Knowing the distance between pressure tap locations and the difference in times of arrival, the projectile velocity was determined. The second technique relied on two parallel laser beams and detectors positioned on opposite sides of the projectile's flight path. Again, knowing the distance between the beams and monitoring

times of arrival. the velocity is easily determined. The last method was to construct a position history of the projectile based on analysis of a high-speed film record. Typically, these three measurements gave impact velocities that agreed to within 5%.

After an experiment, the specimen is recovered and subjected to a post-mortem analysis. This analysis includes measuring the mushroom diameter, the final length and the length of residual rod that remains undeformed. The latter was determined by a gauge used to locate the final position of the plastic front. The test identification number, specimen geometry, impact velocity and post-test measurements are given for each of the five different materials in Tables 2a–e. Additional experimental details are given in House [5] and Wilson et al. [6].

Table 2a. Experimental data for oxygen-free electronic (OFE) copper

Shot No	L/D	U (m s^{-1})	L_1 (mm)	X (mm)	Mushroom diameter (mm)
128	1.5	168	9.1	3.8	11.5
55	1.5	191	8.9	4.1	12.0
127	2	161	12.4	5.5	11.7
147	2	169	12.1	5.5	12.1
64	2	215	10.8	4.7	14.0
129	3	162	18.3	7.8	12.4
63	3	200	16.9	6.2	14.2
65	4	170	24.3	10.3	12.7
126	4	175	23.6	9.3	13.2
16	5	182	28.1	8.3	13.2
133	5	200	27.4	10.4	14.7
73	7.5	153	47.3	22.1	11.8
72	7.5	156	47.3	21.4	11.9
146	7.5	180	42.8	17.1	14.1
57	7.5	188	41.9	16.0	14.4
145	7.5	189	41.7	16.3	14.7
74	10	123	66.4	32.5	10.7
75	10	127	66.6	33.3	10.5
21	10	156	62.3	28.0	12.5
23	10	166	60.6	27.1	13.1
144	10	158	61.0	25.3	12.0
143	10	168	58.8	24.8	13.3
139	10	170	58.5	24.7	13.4
141	10	176	58.7	24.5	13.0
142	10	176	58.3	24.3	13.3
140	10	184	57.9	23.6	13.5

Table 2b. Experimental data for phosphorous deoxidized, tellurium bearing (DPTE) copper

Shot No.	L/D	U (m s^{-1})	L_1 (mm)	X (mm)	Mushroom diameter (mm)
138	1.5	132	9.9	5.0	10.2
79	1.5	139	9.7	4.5	10.2
118	2	138	12.8	6.0	10.8
97	3	136	19.2	8.4	11.2
109	4	141	25.3	11.2	11.4
100	5	152	31.4	13.2	11.5
105	7.5	144	46.7	19.9	11.7
93	7.5	154	46.4	19.8	11.6
86	10	150	61.9	26.7	11.6
87	10	158	60.6	24.7	12.0

J. W. House *et al.*

Table 2c. Experimental data for aluminum alloy 6061-T6

Shot No.	L/D	U (m s^{-1})	L_1 (mm)	X (mm)	Mushroom diameter (mm)
28	1.5	227	10.2	5.2	9.9
69	1.5	235	9.9	4.4	9.9
76	1.5	339	8.3	2.8	12.8
50	2	212	13.6	6.5	9.7
51	2	224	13.3	6.2	10.3
114	2	240	12.9	5.7	10.6
112	2	263	12.5	5.6	11.4
113	2	328	11.4	4.8	13.1
49	3	248	19.4	8.3	11.1
119	3	279	18.5	7.4	12.2
52	4	226	26.5	13.0	10.8
47	4	231	25.9	11.8	11.4
120	4	282	24.6	10.4	12.5
17	5	170	34.8	18.3	9.7
67	5	244	32.7	15.1	11.2
18	5	295	29.9	12.2	13.5
43	7.5	236	49.5	24.1	11.3
45	7.5	242	48.5	22.0	11.9
46	7.5	251	48.5	22.4	11.2
121	7.5	276	46.4	20.0	12.4
71	10	235	66.5	33.5	10.9
68	10	256	63.8	28.7	11.9
19	10	271	63.0	28.2	12.8

Table 2d. Experimental data for aluminum alloy 2024-T4

Shot No.	L/D	U (m s^{-1})	L_1 (mm)	X (mm)	Mushroom diameter (mm)
27	1.5	163	10.9	5.5	8.6
81	1.5	199	10.6	4.7	8.6
83	1.5	283	9.9	3.8	10.0
77	2	221	14.1	7.0	9.0
115	2	250	13.5	4.8	9.7
82	2	289	13.1	4.6	10.3
84	3	266	19.9	7.2	10.0
102	3	297	19.3	6.7	10.9
85	4	248	26.9	10.8	9.8
104	4	282	26.2	9.8	10.4
7	5	195	35.2	16.4	8.9
106	5	289	31.9	11.5	11.3
42	7.5	192	52.6	25.0	9.0
41	7.5	266	49.2	18.8	10.4
122	7.5	270	48.9	18.0	10.3
123	7.5	290	47.8	17.1	11.2
22	10	250	66.6	26.7	10.3
124	10	270	65.0	24.0	10.5
125	10	290	63.7	22.5	11.0

Table 2e. Experimental data for 4340 low strength steel

Shot No.	L/D	U (m s^{-1})	L_1 (mm)	X (mm)	Mushroom diameter (mm)
203	1.5	285	9.2	3.2	10.9
196	2	234	13.1	5.6	10.2
190	2	275	12.4	5.2	11.2
191	2	302	12.0	5.2	12.2
6	3.33	170	23.4	11.2	9.2
4	3.33	215	22.4	10.0	10.3
40	5	181	34.6	15.5	9.5
14	5	183	34.7	15.3	9.8
151	5	224	33.0	11.9	10.5
35	5	234	33.1	13.3	10.6
13	5	270	31.3	11.8	12.1
204	7.5	242	47.8	17.5	11.6
212	10	215	65.7	24.1	10.6
213	10	240	64.4	23.2	11.2

Table 3a. Flow stress for oxygen-free electronic (OFE) copper

Shot No.	S_{Taylor} (MPa)	$S_{z\beta}$ (MPa)	f	S_{ave} (MPa)	$\|\Delta\|$ (%)
128	379	559	0.64	559	0.13
55	455	582	0.62	603	3.62
127	387	551	0.63	561	1.97
147	387	516	0.62	532	3.06
64	421	533	0.64	537	0.88
129	359	518	0.63	523	0.95
63	384	583	0.66	563	3.47
65	389	562	0.64	566	0.76
126	358	541	0.65	532	1.57
16	290	528	0.70	482	8.81
133	356	517	0.66	501	2.93
73	390	535	0.62	556	3.93
72	401	568	0.62	584	2.79
146	336	481	0.65	475	1.32
57	336	490	0.66	478	2.50
145	336	478	0.65	468	1.99
74	354	496	0.61	522	5.24
75	390	539	0.61	570	5.90
21	378	530	0.62	544	2.62
23	374	512	0.63	524	2.41
144	338	502	0.64	502	0.05
143	332	466	0.64	468	0.46
139	334	466	0.64	469	0.48
141	363	513	0.64	514	0.22
142	353	497	0.64	497	0.10
140	371	528	0.64	525	0.52

RESULTS AND DISCUSSION

A value for the parameter f was determined from each test in the data set (Tables 2a–e). The procedure involved first calculating the $\alpha\beta$ solution ($S_{z\beta}$) and then using it to back out a corresponding value of f from Eqn (21). Results of these calculations and, for comparison, the flow stress from Taylor's original analysis, are given in Tables 3a–e.

The values of f for all five materials ranged from 0.58 to 0.70 which correspond to a

Table 3b. Flow stress for phosphorous deoxidized, tellurium bearing (DPTE) copper

Shot No.	S_{Taylor} (MPa)	$S_{\alpha\beta}$ (MPa)	f	S_{ave} (MPa)	$|\Delta|$ (%)
138	391	530	0.60	554	4.40
79	367	516	0.62	528	2.33
118	351	493	0.62	504	2.18
97	326	486	0.63	486	0.17
109	330	483	0.63	485	0.36
100	360	542	0.64	537	0.91
105	310	457	0.63	455	0.58
93	350	513	0.63	510	0.58
86	332	482	0.63	480	0.26
87	325	487	0.65	476	2.44

Table 3c. Flow stress for aluminum alloy 2024-T4

Shot No.	S_{Taylor} (MPa)	$S_{\alpha\beta}$ (MPa)	f	S_{ave} (MPa)	$|\Delta|$ (%)
27	548	853	0.61	912	6.88
81	511	854	0.63	881	3.19
83	524	897	0.65	894	0.25
77	680	1033	0.61	1102	6.65
115	460	857	0.66	838	2.23
82	486	889	0.67	864	2.80
84	465	848	0.66	830	2.12
102	463	841	0.67	815	3.10
85	466	791	0.65	797	0.71
104	481	834	0.66	826	1.04
7	490	779	0.62	816	4.80
106	424	738	0.66	723	2.10
42	444	691	0.62	728	5.41
41	441	756	0.65	752	0.54
122	426	747	0.66	736	1.52
123	427	750	0.67	733	2.34
22	440	739	0.65	744	0.70
124	423	742	0.66	730	1.56
125	421	747	0.67	727	2.68

curve of the type $f > 1/2$ shown in Fig. 4. Average f-values for each material were determined and are given in Table 4. The values in Tables 3a–e under the column heading, S_{ave}, are calculated based on Eqn (21) and the material average value of f. The last column in Tables 3a–e shows the absolute value of the per cent difference between $S_{\alpha\beta}$ and S_{ave}. These differences are less than 5% in 84 of the 92 tests and, remarkably, less than 1% in more than a third of the tests.

CONCLUSIONS

This paper introduces an approximation into the $\alpha\beta$ analysis of the Taylor impact test that produces a simple algebraic formula to estimate the dynamic flow stress. This formula is given as Eqn (21) and produces an excellent approximation to the $\alpha\beta$ solution. By using the material-specific f-values given in Table 4, flow stress estimates within 5% of the $\alpha\beta$ solution can be expected. For even greater simplicity, an overall average f-value of 0.63 can be used in Eqn (21) for all materials. This will produce flow stress estimates that are generally within 10% of the more complex $\alpha\beta$ solution.

Table 3d. Flow stress for aluminum alloy 6061-T6

Shot No.	S_{Taylor} (MPa)	$S_{z\beta}$ (MPa)	f	S_{ave} (MPa)	$|\Delta|$ (%)
28	468	653	0.60	672	2.91
69	388	593	0.61	586	1.09
76	318	516	0.68	470	9.07
50	404	600	0.61	606	0.90
51	379	557	0.58	559	0.42
114	344	516	0.63	509	1.37
112	356	505	0.62	501	0.74
113	361	494	0.64	479	3.03
49	367	568	0.64	555	2.39
119	347	533	0.65	512	3.89
52	380	534	0.61	544	1.78
47	328	475	0.62	474	0.23
120	364	538	0.64	523	2.70
17	335	467	0.60	487	4.15
67	392	569	0.62	569	0.07
18	348	513	0.64	495	3.57
43	396	554	0.61	563	1.72
45	356	519	0.62	516	0.51
46	385	551	0.62	551	0.14
121	358	522	0.63	511	2.05
71	422	577	0.60	593	2.72
68	365	528	0.62	524	0.70
19	386	552	0.63	548	0.83

Table 3e. Flow stress for 4340 low strength steel

Shot No.	S_{Taylor} (MPa)	$S_{z\beta}$ (MPa)	f	S_{ave} (MPa)	$|\Delta|$ (%)
203	1057	1594	0.67	1523	4.45
196	1097	1497	0.64	1508	0.75
190	1123	1476	0.64	1481	0.37
191	1169	1424	0.63	1451	1.84
6	1164	1576	0.61	1659	5.27
4	1160	1575	0.62	1622	3.00
40	1049	1473	0.63	1506	2.24
14	1099	1571	0.63	1598	1.74
151	982	1559	0.66	1504	3.56
35	1153	1691	0.65	1676	0.88
13	1076	1561	0.66	1522	2.52
204	936	1419	0.66	1372	3.28
212	889	1388	0.66	1343	3.18
213	976	1515	0.66	1459	3.67

Table 4. Average value of f

Material	$f_{average}$
OFE copper	0.64
DPTE copper	0.63
2024-T4 aluminum	0.65
6061-T6 aluminum	0.62
4340 Low strength steel	0.64

REFERENCES

1. G. I. Taylor, The use of flat-ended projectiles for determining dynamic yield stress: I. Theoretical considerations. *Proc. R. Soc. Lond. Ser. A.* **194**, 289–300 (1948).
2. J. B. Hawkyard, A theory for the mushrooming of flat-ended projectiles impinging on a flat rigid anvil, using energy considerations. *Int. J. Mech. Sci.* **11**, 313–333 (1969).
3. I. M. Hutchings, The behavior of metals under ballistic impact at sub-ordnance velocities. In *Material Behavior Under High Stress and Ultrahigh Load Rates* (Edited by John Mescall and Volker Weiss), p. 161. Plenum Press, New York (1983).
4. S. E. Jones, P. P. Gillis and J. C. Foster, Jr. On the equation of motion of the undeformed section of a Taylor impact specimen. *J. Appl. Phys.* **61**, 499–502 (1987).
5. J. W. House, Taylor impact testing. AFATL-TR-89-41, Air Force Armament Laboratory, Eglin AFB, September (1989).
6. L. L. Wilson, J. W. House and M. E. Nixon, Time resolvable deformation from the cylinder impact test. AFATL-89-76, Air Force Armament Laboratory, Eglin AFB, November (1989).

APPENDIX C

ON THE TAYLOR TEST: A CONTINUUM ANALYSIS OF PLASTIC WAVE PROPAGATION

J. C. Foster, Jr.[*], P. J. Maudlin[+], and S. E. Jones[**]

Wright Laboratory/Armament Directorate, Eglin AFB, Florida 32542
+ Los Alamos National Laboratory, Los Alamos, New Mexico 87545
*** Department of Mechanical Engineering, University of Alabama, Tuscaloosa, Alabama 35487*

The determination of the mechanical properties of materials is the foundation of many engineering design problems. Numerous test methods have evolved as standards for the determination of these properties. Design problems which require inelastic behavior of the material are unique because the test methods must provide a detailed knowledge of the evolution of the yield behavior. High rate problems represent a special class of inelastic engineering design problems and the interpretation of test methods used to determine material's behavior for these problems are an important research topic. The Taylor Anvil or Taylor Impact test is a test commonly employed to determine the mechanical properties of materials for this important class of engineering design problems. A continuum approach based on jump discontinuities at the plastic wave front is developed which can be used as the basis for advanced engineering models of the experiment and analysis of the numerical method used to incorporate various constitutive relationships into continuum codes.

INTRODUCTION

Taylor Anvil Experiment

The determination of the inelastic behavior of metals subjected to high rates of loading is a subject of continued interest to a wide range of engineering problems. Examples of these include metal forming, high velocity impact, and explosive/metal design. One experimental technique in common use is the Taylor Impact test.(1) The test consists of impacting a right circular cylinder specimen against an anvil which represents a rigid semi-infinite plane. Taylor's model of the experiment is a one-dimensional rigid plastic formulation which utilizes post test measurements to determine a strength characteristic for the specimen material. This characteristic is generally interpreted as a saturation flow stress such as might be used in a perfectly plastic constitutive rule. The test is widely used to evaluate more complex constitutive descriptions used in continuum mechanics computer codes.(2,3,4) Most comparisons are limited to the final geometric parameters. This approach, although more detailed than that used in Taylor's model, lacks a clear description of the relationship between the constants in the constitutive equation used in the code and the particular mechanical parameter measured from the recovered specimen. Recent refinements of the experimental techniques have significantly expanded the data which can be obtained from the experiment.(5,6,7) Data is obtained from high speed cameras (2 Mfps) and imbedded gages which measure stress wave arrival and amplitude time signatures. These additional data permit the refinement of the analytical models used to describe the experiment and the development of algorithms to interpret the data in terms of constitutive constants where the relationship between the constitutive parameter and the data is

explicitly described in the formulation of the engineering model of the experiment.

Engineering Models vs. Data Recovered

The simplifying assumptions used in Taylor's original formulation have been re-evaluated in terms of the expanded data base obtained from the experiment. The equation of motion of the rigid rod section has been formulated to include mass loss from the undeformed specimen length and a strain discontinuity at the plastic wave front.[8] This model uses post test measurements of the specimen overall length (L_f) and the undeformed section length (l_f) to correlate the deformation in the specimen with an improved estimate of the flow stress (σ). The boundary conditions at the specimen-anvil interface at $t = 0$ have been formulated in terms of one dimensional shock jump conditions which when combined with Hugonoit data[9] for the anvil and the specimen material provide a relationship between the impact velocity and the particle velocity behind the plastic wave. This approach has identified two distinct phases in the deformation of the specimen. An early short duration phase which is characterized by the initial shock transients and relaxation to a quasi-steady plastic wave (phase I). The initial phase can be used to access the rate dependency in the constitutive properties of the material. The later phase (phase II) is being used to access the stress/strain/strain rate history of the specimen deformation.[10,11]

CURRENT DEVELOPMENTS

Most recently, a continuum analysis of the propagation of a plastic wave on a right circular cylinder of finite dimensions has been developed which yields insight as to how the parameters in the constitutive equation relate to the dynamics of the wave propagation and aids in the development of an algorithm for determining constants which characterize the mechanical behavior of the material consistent with a specific form of the constitutive equation.

Jump Conditions

The problem of a plastic wave propagating on a right circular cylinder of finite dimensions is formulated in terms of jump discontinuities associated with the wave front after the approach used by Rankine.[12] An essential element in the formulation of a continuum analysis of the plastic wave propagation is a recognition that the wave is propagating in the rest frame of the specimen(u_w). The problem can then be formulated in terms of the stress (σ), strain (ε), density (ρ), particle velocity (u), and internal energy (i) as state variables (see Figure 1). Conservation of mass, momentum, and energy combined with the equation of state and the constitutive equation of the mechanical behavior constitute a complete set of equations.
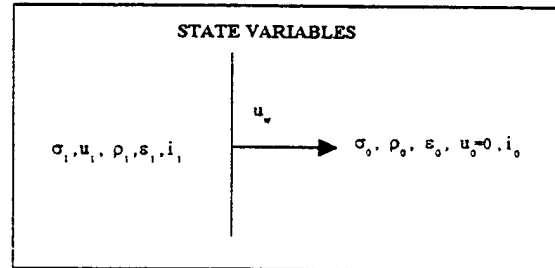

Figure 1. Variables relative to the plastic wave front. Variables with subscript 0 are up stream of the wave and subscript 1 are downstream.

The conservation of mass, momentum, and energy equations for a steady plastic wave propagating on a right circular cylinder are initially expressed in terms of the wave velocity (u_w), the cross sectional area (A), the density (ρ), the specific energy density (i), and the particle velocity behind the wave (u_1) as

$$\rho_0 A_0 u_w = \rho_1 A_1 (u_w - u_1) \qquad (1)$$

$$\sigma_1 A_1 - \sigma_0 A_0 = -\rho_0 A_0 u_w u_1 \qquad (2)$$

and

$$i_1 - i_0 = \frac{1}{2}\left[u_w^2 - (u_w - u_1)^2\right] + \frac{\sigma_1}{\rho_1} - \frac{\sigma_0}{\rho_0} \qquad (3)$$

respectively.

Now equation 1 can be rearranged to yield

$$\left(\frac{\rho_0 A_0}{\rho A} - 1\right)u_w = -u_1 \qquad (4)$$

by subtracting and adding $\frac{A_0}{A}$ to the expression in the brackets,

$$\left(\frac{\rho_0 A_0}{\rho A} - 1\right) = \frac{A_0}{A}\left(\frac{\rho_0}{\rho} - 1\right) + \left(\frac{A_0}{A} - 1\right) \qquad (5)$$

Now, using $\rho \equiv \frac{1}{v}$,

$$\frac{\rho_0}{\rho} - 1 = \frac{\frac{1}{v_0} - \frac{1}{v}}{\frac{1}{v}} = \frac{v - v_0}{v_0} \qquad (6)$$
$$= \frac{\Delta v}{v_0} \equiv \varepsilon_v$$

In the limit of incompressible flow for phase I, $A_0 L_0 = AL$. Then,

$$\frac{A_0}{A} = \frac{L}{L_0} = \frac{L_0 + \Delta L}{L_0} = 1 + e \qquad (7)$$

where e is the one dimensional engineering strain. Now equation (5) can be written as

$$\frac{\rho_0 A_0}{\rho A} - 1 = e + e\varepsilon_v + \varepsilon_v \qquad (8)$$

and the conservation of mass equation becomes

$$u_w = -\frac{u_1}{e(\varepsilon_v + 1) + \varepsilon_v} \qquad (9)$$

Similar algebraic manipulations will yield conservation of momentum written in the same state variables as

$$\frac{\sigma_1}{1 + e} - \sigma_0 = -\rho_0 u_w u_1 \qquad (10)$$

The development now follows the method of using shock jump conditions to isolate kinematic and thermodynamic variables to formulate the Hugoniot equation. The conservation of mass equation can then be used to eliminate the particle velocity (u_1) from equation (10), to give

$$\frac{\sigma_0 - \frac{\sigma_1}{1 + e}}{\left[\varepsilon_v(e + 1) + e\right]} = -\rho_0 u_w^2 \qquad (11)$$

which reduces to the equation for the classical Rayliegh line in shock physics for e=0.

The wave velocity (u_w) can next be eliminated from (10), to give

$$\left[\sigma_0 - \frac{\sigma_1}{1 + e}\right]\left[\varepsilon_v(e + 1) + e\right] = -\rho_0 u_1^2 \qquad (12)$$

which is the equation for the constant particle velocity curve in terms of stress and strain criteria for the jump across the wave front.

Finally, the conservation of mass and momentum equations can be used to rewrite the conservation of energy equation,

$$\rho_0(i - i_0) = \frac{1}{2}\left[\varepsilon_v(e + 1) + e\right]\left[\sigma_0 + \frac{\sigma_1}{1 + e}\right] \qquad (13)$$

in terms of stress and strain which is a form of the Hugoniot equation. Equations (11), (12), and (13) in general require an equation of state and a constitutive equation to completely specify the curves in stress/strain space. This is a specific problem solution and is the subject of Maudlin, Foster, and Jones.(14)

CONCLUSIONS

We have presented an approach to understanding and analyzing time resolved data that results from impact experiments such as the classical Taylor

anvil test. The approach provides a local analytical solution to the equation of motion for a plastic wave propagating on a finite diameter right circular cylinder. In addition to providing insight into the development of the constitutive properties of the rod material from such data, the analysis provides a means of locally assessing the accuracy of continuum mechanics based codes on a relatively inexpensive problem.(14) Futher, this analysis can be transformeded to produce results that are completely equivalent to those developed by an alternative engineering approach.(15) It is obvious that the method can be extended along the development lines of the classical shock problem to provide even greater insight into this classical problem.

ACKNOWLEDGMENTS

REFERENCES

1. Taylor, G. I., *Proc. R. Soc. London Ser. A*, 194, 289, 1948.

2. Johnson, G. R., and Holmquist, T. J., *J. Appl. Phys.*, 64, 8, 1988.

3. Holmquist, T. J., and Johnson, G. R., *Proc. DYMAT 91 Conference*, Strasbourg, France, October 1991

4. Rajendran, A. M., and Groves, D. J., "Bodner-Partom Viscoplastic Model in STEALTH Finite Difference Code," *Air Force Material Laboratory Report*, AFWAL-TR-86-4098, 1986.

5. Wilson, L. L., House, J. W., and Nixon, M. E., "Time Resolved Deformation from the Cylinder Impact Test," *Air Force Armamnet Laboratory Report*, AFATL-TR-89-76, 1989.

6. Synder, D. R., Wilson, L. L., and House, J. W., "Analysis of High Speed Framing Camera Data for the Development of Material Models used in Penetration Mechanics," *Proceedings of SPIE Conference on Ultrahigh Speed and High Speed Photography, Photonics and Videography '89* San Diego, CA, August 7-9, 1989.

7. House, J. W., Wilson, L. L., and Nixon, M. E., *Mechanical Behavior of Material --VI. Vol. 1, Kyoto, Japan, 29 July - 2 Aug. 1991*, Oxford, U. K., Pergamon Press, 1991.

8. Jones, S. E., Gillis, P. P., and Foster, J. C., Jr., *J. Appl. Phys.*, 61, 2, 1987.

9. Marsh, S. P., *LASL Shock Hugonoit Data*, University of Calif. Press, 1980.

10. Jones, S. E., Gillis, P. P., Foster, Jr., J. C., and Wilson, L. L., *Journal of Engn. Matl. and Tech.* 113, 1991.

11. Cinnamon, J. D., Jones, S. E., Foster, Jr., J. C., and Gillis, P. P., "An Analysis of Early Time Deformation Rate and Stress In the Taylor Impact Test," *Proceedings of the Sixth International Conference on Materials Science (Mechanical Behaviour of Materials-VI)*, Kyoto, Japan, 29 July-2 August 1991.

12. Rankine, W.J.M., "On the Thermodymanic Theory of Waves of Finite Longitudinal Disturbance," Phil. Trans. Roy. Soc. London, 160, 277, 1867.

13. M°Clintock, F. A., and Argon, A. S., *Mechanical Behavior of Materials*, ISBN 1-8789907-71-9, Addison-Wesley Publishing Company.

14 Maudlin, P. J., Foster, Jr., J. C., and Jones, S. E., "On the Taylor Test, Part III: A Continuum Mechanics Code Analusis of Steady Plastic Wave Propagation," Los Alamos National Laboratory report LA-12836-MS,1994.

15 Jones, S.E, Maudlin, P. J., Foster, Jr., J. C., and Kazmeir, M., "On the Taylor Test, Part II: An Engineering Analysis of Plastic Wave Propagation," Los Alamos National Laboratory report LA-12845-MS, 1994.

APPENDIX D

AN ENGINEERING ANALYSIS OF PLASTIC WAVE PROPAGATION IN THE TAYLOR TEST

S. E. JONES†, PAUL J. MAUDLIN‡ and JOSEPH C. FOSTER, JR§

† Department of Aerospace Engineering and Mechanics. The University of Alabama,
Tuscaloosa. AL 35487, U.S.A.
‡ Group T-3, Theoretical Division. Los Alamos National Laboratory,
Los Alamos, NM 87545, U.S.A. and
§ Wright Laboratory, Armament Directorate. Eglin Air Force Base. FL 32542–6810, U.S.A.

Summary—A new one-dimensional analysis of the Taylor impact test is presented. This analysis differs from any previously presented in that the wave mechanics are separated from the calculation of dynamic stress. The new results utilize post test measurements to estimate key parameters in the plastic wave propagation. However, these measurements are incorporated into the analysis in a very unconventional way. A comparison with continuum code calculations shows very good agreement has been achieved. Copyright © 1996 Elsevier Science Ltd.

INTRODUCTION

The Taylor impact test [1] is a useful experiment for estimating material behavior at high strain rates. The test is reproducible and is reasonably economical after the initial investment has been made. The difficulty is to interpret the experimental data to reflect the constitutive properties of the specimen.

Originally, the one-dimensional analysis of Taylor [1] was used by Whiffen [2] to estimate the dynamic yield stress of the specimen. However, the dynamic yield stress, by itself, does not provide the information necessary for a complete description of material behavior. In succeeding years, several improvements in the interpretation of test data have been offered by Lee and Tupper [3], Hawkyard [4], Hawkyard *et al.* [5], and others. Using a double frustum approximation, Hawkyard *et al.* [5] provided estimates for mean stress, mean strain, and mean strain rate. These results apply to ductile metals. Barenblatt and Ishlinskii [6] and Ting [7] gave results that apply to viscoplastic materials, and Hutchings [8] used the test to estimate the dynamic yield stress in polymeric materials.

Modern technologies have placed demands for accurate constitutive modeling at strain rates exceeding 10^4/s. These rates are achieved in the Taylor test for even relatively low velocities but are very difficult to achieve using other methods. This makes for further development of theories with which constitutive properties of the specimen material can be deduced for useful enterprise.

High-speed photography of specimen impacts (see Wilson *et al.* [9]) has opened a new window of opportunity to study time resolved specimen behavior. Recent developments in Taylor modeling fall into two categories: improvements in one-dimensional models and the use of computer codes to deduce the free parameters in constitutive equations. Both approaches have advantages. For a discussion of the latter for example, the reader is directed to Johnson and Holmquist [10] or Maudlin *et al.* [11]. One-dimensional models have the advantage of independence from assumptions regarding the functional form of a constitutive relation. They are usually very simple and offer insights into material behavior that are often missed in more complicated models. In spite of simplicity, the prospect for fairly accurate constitutive relations using one-dimensional models is very promising.

This paper continues the spirit of Jones *et al.* [12] that proposes an equation of motion for the undeformed section which accounts for loss of mass across the plastic wave front. Later, Jones *et al.* [13] noted that a period of nonlinear initial transient behavior after impact could substantially affect estimates of plastic wave speed. A successful analysis must account for this period and the shock hardening of specimen material accompanied by it.

D-1

THEORY

In Fig. 1, the basic nomenclature for the analysis is described. The time-dependent displacements, h and s, are positive, as is the undeformed section length, l. In our previously reported work [12], an examination of the change in linear momentum for the undeformed section, the portion of it that has become plastically deformed, and the net impulse on the system lead to the equation of motion for the undeformed section.

$$l\dot{v} + l(v - u) = \frac{\sigma}{\rho(1 + e)}. \tag{1}$$

In this equation, v is the velocity of the undeformed section, u is the particle velocity of the plastic material at the wave front, σ is the engineering stress on the plastic side of the front, ρ is the density, and e is the engineering strain at the front. This equation continues to be valid. However, a more careful interpretation of the stress proves to be worthwhile.

Consider an element of the undeformed section at time t that will be fully deformed at time $t + \Delta t$ (see Fig. 2). An impulse-momentum equation can be written for the shaded and unshaded bodies over the elapsed time Δt. The impulses are estimated by averaging the forces and multiplying by the elapsed time. These equations are:

$$\rho A_0 \Delta l v - \rho A_0 \Delta l u = \frac{\sigma A + (\sigma + \Delta\sigma)(A + \Delta A) - \sigma_0 A_0 - (\sigma_0 + \Delta\sigma_0)A_0}{2} \Delta t \tag{2}$$
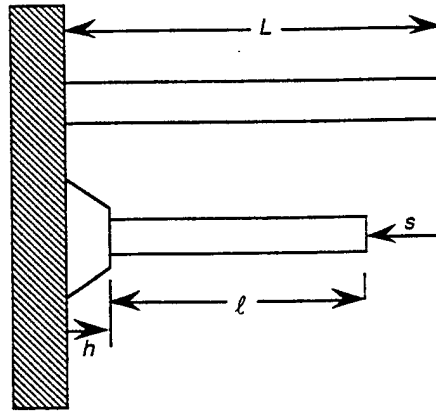
Fig. 1. Schematic view showing a Taylor specimen of original length L which undergoes plastic deformation.
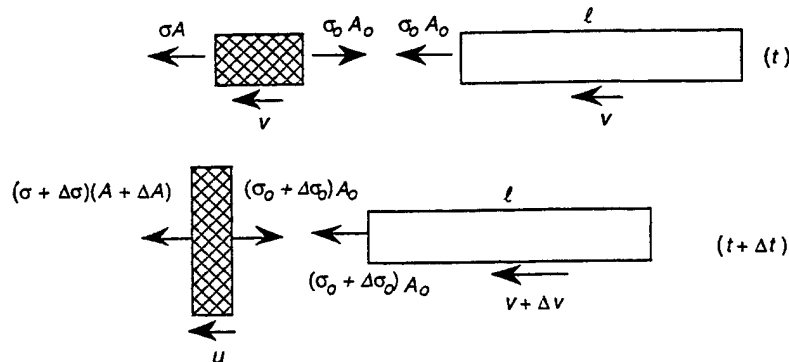

Fig. 2. Schematic view of undeformed and plastic segments over an elapsed time Δt. The shaded segment of mass $-\rho A_0 \Delta l$ has become plastically deformed at time $t_f \Delta t$ and is now moving with speed u.

and

$$\rho l A_0 (v + \Delta v) - \rho l A_0 v = \frac{(\sigma_0 + \Delta \sigma_0) A_0 + \sigma_0 A_0}{2} \Delta t. \tag{3}$$

Dividing by Δt and taking the limit as $\Delta t \to 0$, we get

$$\rho A_0 \dot{l}(v - u) = \sigma A - \sigma_0 A_0 \tag{4}$$

and

$$\rho A_0 l \dot{v} = \sigma_0 A_0. \tag{5}$$

Dividing both equations by A_0 and using

$$e = \frac{A_0}{A} - 1, \tag{6}$$

Eqns (4) and (5) reduce to

$$\rho \dot{l}(v - u) = \frac{\sigma}{1 + e} - \sigma_0 \tag{7}$$

and

$$\rho l \dot{v} = \sigma_0. \tag{8}$$

The stresses σ and σ_0 in Eqns (7) and (8) are generally both time dependent and will be interpreted later within the context of three distinct phases of deformation. Notice that Eqn (1) can be recovered by adding Eqns (7) and (8) and dividing by the density ρ.

The remaining equations for describing the motion of the specimen stem from conservation of mass [12]

$$e\dot{l} = v - u \tag{9}$$

and adding the lengths in Fig. 1

$$h + s + l = L. \tag{10}$$

The last equation can also be differentiated to give

$$\dot{h} + \dot{s} + \dot{l} = \dot{h} + v + \dot{l} = 0 \tag{11}$$

because $\dot{s} = v$.

PHASES OF DEFORMATION

Recently [13], the deformation of a Taylor specimen was characterized by two patterns of behavior. The early time behavior, denoted by Phase I, was shock dominated nonlinear motion of the plastic wave front. This was followed by steady motion of the plastic wave front, denoted by Phase II. This simple description is mostly correct, but it is evident that the velocity of the plastic wave front must come to zero at the end of the event. Hence, a description that includes nonlinear behavior of the wave front at the end of the event is appropriate.

As shown in Fig. 3, the stages of deformation of the Taylor specimen are characterized by the addition of a third regime, Phase III, in which deceleration of the plastic wave front occurs. Notice that $\dot{h}$ comes to zero at the end of the event.

PHASE I DEFORMATION

Equations (7), (9), (10) and (11) provide an adequate description of the deformation during Phase I. As we have previously observed [13], the undeformed section suffers no deceleration
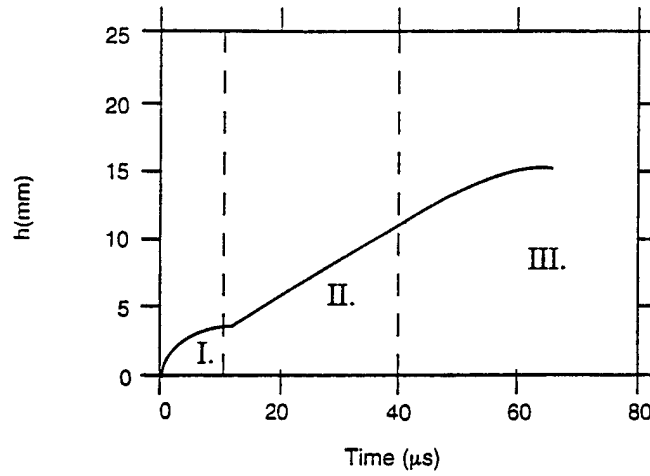
Fig. 3. Plastic wave front position as a function of time. For this test, the transition time between Phases I and II occurs at about 10 μs.

during this phase. Thus, Eqns (7), (9), (10) and (11) become

$$\rho \dot{l}(v_0 - u) = \frac{\sigma}{1 + e} - \sigma_0, \tag{12}$$

$$e \dot{l} = v_0 - u, \tag{13}$$

$$h + l + v_0 t = L, \tag{14}$$

and

$$\dot{h} + \dot{l} + v_0 = 0. \tag{15}$$

In order to meet the objection to the variable strain distribution used in [13], we shall assume that $e = $ const throughout the test. This is a questionable assumption during early time deformation, but it produces good results nevertheless.

Manipulating Eqns (12) and (13), we find the early time dynamic stress

$$\sigma = (1 \div e)\left(\sigma_0 + \frac{\rho}{e}(v_0 - u)^2\right). \tag{16}$$

This stress is expressed in terms of the unknown strain e and the particle velocity u. It is inappropriate to use Eqn (8) here. During Phase I deformation, the particle velocity is highly variable. A quadratic approximation was introduced in [15], which was shown to provide an adequate description of u,

$$u = u_0 + u_1\left(\frac{t}{\bar{t}} - \frac{t^2}{2\bar{t}^2}\right). \tag{17}$$

where u_0 and u_1 are constants to be determined and $\bar{t}$ is the time to end Phase I deformation. As noted in [13], for 30 caliber copper rods impacting 4340 steel anvils $\bar{t} \approx 10 \,\mu$s. The initial particle velocity has been estimated by elementary shock physics as $u_0 \approx v_0/2$. When $\bar{t}$ is reached, we enter the stage of quasi-steady motion; u is constant there, and thus $du/dt = 0$ at $t = \bar{t}$.

To conclude this section, we note that the motion of the plastic wave front can be estimated by Eqns (13), (15) and (17) during Phase I deformation. By combining them, we get

$$\dot{h} = -v_0 - \dot{l} = \frac{u}{e} - \frac{1+e}{e}v_0$$

$$= \frac{1}{e}\left(u_0 + u_1\left(\frac{t}{\bar{t}} - \frac{t^2}{2\bar{t}^2}\right)\right) - \frac{1+e}{e}v_0. \tag{18}$$

Integrating this equation, the time-dependent position of the plastic wave front can be found,

$$h = \frac{u_0 - (1-e)v_0}{e}t + \frac{u_1}{e}\left(\frac{t^2}{2\bar{t}} - \frac{t^3}{6\bar{t}^2}\right). \tag{19}$$

At the end of Phase I deformation, the position of the plastic wave front is given by

$$\bar{h} = \frac{u_0 - (1-e)v_0}{e}\bar{t} + \frac{u_1}{3e}\bar{t}. \tag{20}$$

PHASE II DEFORMATION

After $t = \bar{t}$, a period of quasi-steady motion occurs. The duration of this period depends on several things, but most importantly the length of the undeformed section after Phase I deformation. The longer this section, the more sustained will be the period of Phase II deformation.

All of the physical parameters in the problem are virtually constant during Phase II deformation. So, certainly the particle velocity is proportional to the undeformed section velocity. This proportionality is also maintained during the terminal transient stage, Phase III. Hence, we assume that there exists a dimensionless constant β for which

$$u = \beta v \tag{21}$$

throughout Phases II and III deformations.

When we combine Eqns (9) and (21), we get

$$el = (1 - \beta)v. \tag{22}$$

Now, this result can be used in Eqn (11) to find the plastic wave speed

$$\dot{h} = -\left(1 + \frac{1-\beta}{e}\right)v. \tag{23}$$

Because $v = \dot{s}$, this equation can be directly integrated:

$$h - \bar{h} = -\left(1 + \frac{1-\beta}{e}\right)(s - \bar{s}). \tag{24}$$

The constant of integration has been evaluated at the beginning of Phase II deformation. It is tacitly assumed that all physical variables are continuous at the interface between Phases I and II. If we extend Eqn (24) to the end of the event, we get

$$h_{\mathrm{f}} = \bar{h} = -\left(1 + \frac{1-\beta}{e}\right)(s_{\mathrm{f}} - \bar{s}), \tag{25}$$

where h_{f} and s_{f} are the final positions of the plastic wave front and back end of the specimen, respectively.

The final displacement of the back end of the specimen can be found with a high degree of certainty. The final position of the plastic wave front or, equivalently, the final undeformed section length, is a measurement wrought with uncertainty. We say this because the criterion for determining the final position is *ad hoc* at best [2]. Unfortunately, the resulting predictions for dynamic stress [1, 17] are highly dependent on this length. In the next section a new procedure for this measurement will be introduced. When used with Eqn (25), this method is shown to produce very good estimates of dynamic yield stress for OFHC copper in the annealed and unannealed states.

Now, continuing with the development of the basic equations, we assume that the particle velocity is continuous across the Phase I/Phase II interface and match Eqns (17) and (21) when $t = \bar{t}$ and $v = v_0$. This leads to

$$u_0 + \frac{1}{2}u_1 = \beta v_0. \tag{26}$$

D-5

As indicated earlier, u_0 can be found from elementary shock physics applied at the point of impact. For a copper rod impacting a 4340 steel anvil. $u_0 \approx v_0/2$ and Eqn (26) can be used to find

$$u_1 = (2\beta - 1)v_0. \tag{27}$$

When this value of u_1 is put in Eqn (20), we find

$$\frac{\bar{h}}{v_0 \bar{t}} = \frac{2\beta - 1}{3e} - \frac{1 + 2e}{2e}, \tag{28}$$

which is another independent, linear relationship between β and e. Together Eqns (25) and (28) comprise a system of two linear algebraic equations in the unknowns β and e.

POST TEST MEASUREMENTS AND THE SOLUTION FOR β AND e

Figure 4 shows time-resolved film data from a Taylor test [9]. A 30-caliber OFHC as received copper rod having a length to diameter ratio of 7.5 was impacted against a 4340 steel anvil at 176 m/s. For this test from the film record $\bar{t} \approx 10\,\mu s$. and $\bar{h} \approx 5.1$ mm. A measurement of the deformed specimen gives $s_f = 14.24$ mm. The overall undeformed length of the rod was 0.05715 m, and $\bar{s} = v_0 \bar{t} = 1.76$ mm. Now. the left-hand side of Eqn (28) is known and all but h_f is known in Eqn (25).

As indicated earlier, the measurement for h_f is very subjective. In this paper, we introduce a method for locating the undeformed section length on a Taylor specimen that is connected to the analysis and has very little uncertainty. It is evident that the final position of the plastic wave front must depend on the strain e at which the test is carried out. Since the strain is an unknown, this measurement must be incorporated into the system of Eqns (25) and (28) as a function of e. In general, $h_f = h_f(e)$ is a highly nonlinear function of the unknown strain. However, for practical purposes, the linearity of Eqns (25) and (28) can be maintained while performing a trial and error search along the deformed specimen until agreement in the unknown strain is reached.

Figure 5 shows the profile geometry of the deformed Taylor specimen mentioned in Fig. 4. The specimen was measured with a high resolution, optical comparator to achieve the position/diameter data presented in Table 1. Various undeformed section lengths were tried
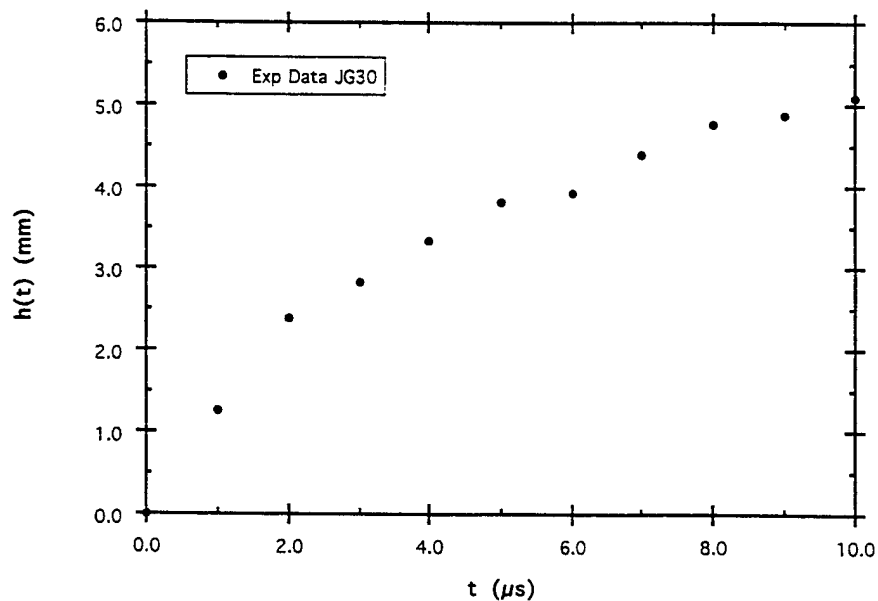

Fig. 4. Time resolved wave front versus time data for an as-received OFHC copper rod impacting a 4340 steel anvil at 176 m/s (from Wilson *et al.* [9]).
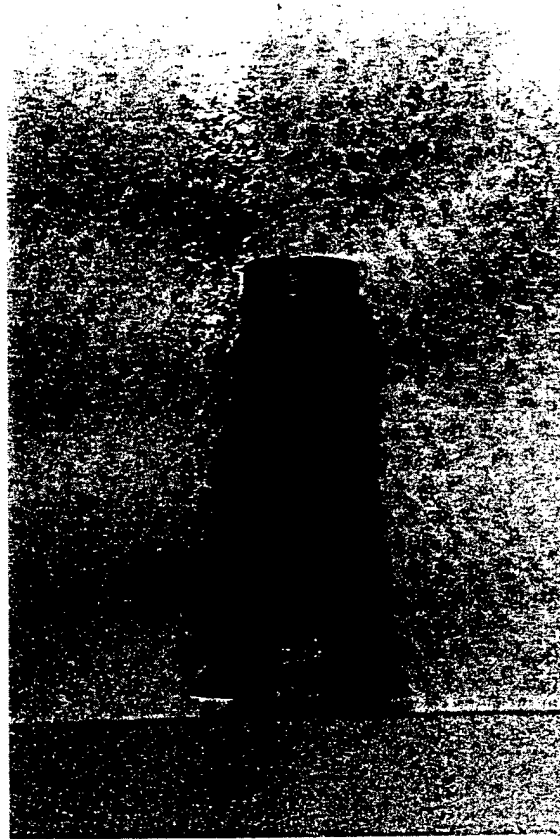
Fig. 5. Final geometry of a recovered OFHC copper impact specimen. The impact velocity was 176 m/s, and the material was as received.

Table 1.

Axial position (mm)	Rod diameter (mm)	Axial position (mm)	Rod diameter (mm)	Axial position (mm)	Rod diameter (mm)
0.00	7.62	20.32	7.82	32.39	9.65
1.27	7.62	20.96	7.87	33.02	9.75
2.54	7.62	21.59	8.00	33.66	9.86
3.81	7.62	22.23	8.08	34.29	9.96
5.08	7.62	22.86	8.15	34.93	10.14
6.35	7.62	23.5	8.23	35.56	10.26
7.62	7.62	24.13	8.31	36.20	10.29
8.89	7.62	24.77	8.46	36.83	10.39
10.16	7.62	25.40	8.56	37.47	10.47
11.43	7.62	26.04	8.69	38.10	10.41
12.70	7.62	26.67	8.79	38.74	10.39
13.97	7.62	27.31	8.89	39.37	10.39
15.24	7.66	27.94	8.97	40.06	10.59
16.51	7.67	28.58	9.09	40.64	11.18
17.15	7.70	29.21	9.17	41.28	12.09
17.78	7.72	29.85	9.27	41.91	12.98
18.42	7.72	30.48	9.37	42.55	13.59
19.05	7.77	31.12	9.47	42.85	13.74
19.69	7.82	31.75	9.55		

in Eqns (25) and (28) until agreement with the engineering strain in the specimen at that cross section was achieved. Linear interpolation between the measured cross sections was used to find the location 21.12 mm from the undeformed end. The strain at this location is about −0.071. With this undeformed section length, the final position for the plastic wave front is $h_f = 21.74$ mm. Equations (25) and (28) can now be solved simultaneously to find $e = -0.0712$ and $\beta = 0.834$.

Having found β and e, we are able to calculate all of the other physical parameters in the test. For example, the dynamic stress during quasi-steady, Phase II deformation, can be found from Eqn (7)

$$\sigma = (1 + e)\left(\sigma_0 + \frac{(1 - \beta)^2}{e} \rho v_0^2\right). \tag{29}$$

In this equation, σ_0 is some reference stress, which we will take to be $\sigma_0 = -293$ MPa, a quasi-static yield stress estimate in compression for this OFHC, as received, copper. Using the values of e and β just found in the previous paragraph, we obtain $\sigma = -371$ MPa, a dynamic increment of about 27% in compression for this material at a strain rate consistent with Phase II deformation. The results are in very good agreement with code calculations [11]. Notice that the particle velocity is $u = \beta v_0 = 147$ m/s, and the plastic wave speed is $\dot{h} = -(1 + (1 - \beta)/e)v_0 = 234$ m/s during Phase II deformation. This translates to $u_1 = v_0 - u = 29$ m/s and $u_{pw} = \dot{h} + v_0 = 410$ m/s in Ref. [16]. From Fig. II. 2 in [16] the calculated values of u_{pw} range from 490 m/s for a strain-rate of 10^4 s^{-1} to 450 m/s for 10^3 s^{-1}, assuming the MTS flow stress model results. A one-dimensional analysis cannot be expected to perform much better. But, one source of improvement can be found in the nominal stress σ_0. There is some justification for taking it higher than quasi-static yield. If this were done, somewhat better agreement would be achieved. In fact, in order to match quasi-static yield with Eqn (29) as $v_0 \rightarrow 0$, we must take $\sigma_0 = \sigma_s/(1 + e)$, where σ_s is the quasi-static yield stress for the material. Now, $\sigma = -392$ MPa, and we are very close to the intersection point predicted by the code.

AN ANNEALED COPPER EXAMPLE

Additional Taylor cylinders were fabricated from the same OFHC copper used for the previous specimen. These were annealed. The quasi-static yield stress for the annealed material was found to be only 83 MPa, only 28% of the half hard copper [9]. This soft material presents several problems for experimentalists. It is usually desirable, from an analysis point of view, to test longer cylinders. The reason for this is short cylinders of soft metal tend to be completely deformed, and there is no perceptible undeformed section length remaining. Whenever this happens, an analysis with any of the previously reported one-dimensional models is impossible because the undeformed section length usually appears in the denominator of some key fraction. Even if there is a small amount of undeformed material, there is usually too much uncertainty in the measurement to trust the results. Even minor inaccuracies in the undeformed section length can have a profound effect on the prediction of dynamic yield stress. This fact and the general uncertainty connected with the measurement of undeformed section length has caused some researchers to turn away from one-dimensional models of the Taylor test entirely.

The analysis in this paper does not suffer from the defect of being unperformable when the undeformed section length goes to zero. That does not say that the results are very good when this happens. In the example we are about to present, treating the final position of the plastic wave front as the back end of the deformed specimen produces a very poor estimate of dynamic yield stress for annealed copper. However, if we employ the technique described in the previous section for locating the final position of the plastic wave front, we get excellent results.

Figure 6 shows the time-resolved film data from a Taylor test [9] on annealed OFHC copper. The specimen is 30 caliber and is impacted at 227 m s against a 4340 steel anvil. For
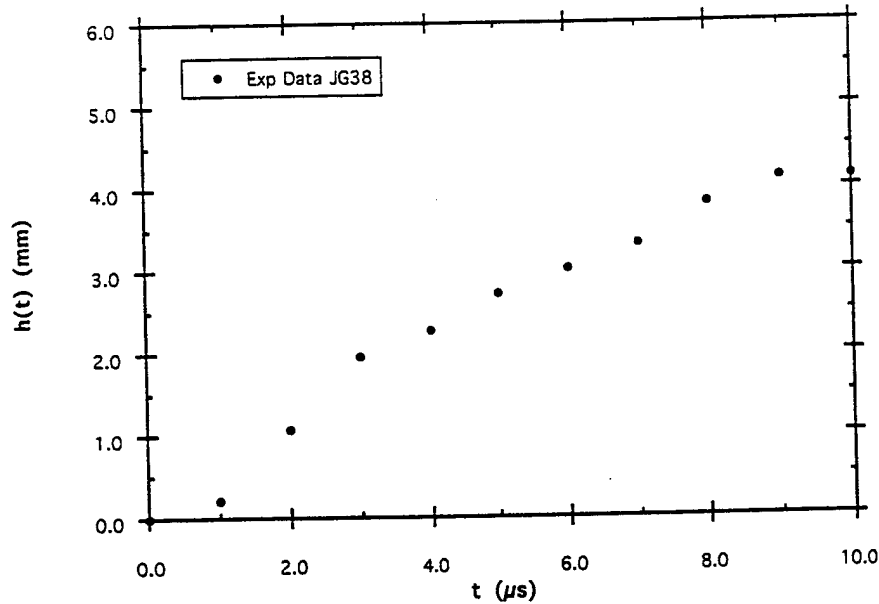
Fig. 6. Time resolved wave front versus time data for an annealed OFHC copper rod impacting a 4340 steel anvil at 227 m/s (from Wilson *et al.* [9]).

this test, $\bar{t} \approx 10\,\mu s$ and $\bar{h} \approx 4.20\,\text{mm}$. A measurement of the deformed specimen gives $s_f = 15.60\,\text{mm}$. The overall undeformed length of the rod was 38.1 mm and $\bar{s} = v_0\bar{t} = 2.27\,\text{mm}$. With these measurements, the left-hand side of Eqn (28) is known and all but h_f is known in Eqn (25).

Figure 7 shows the profile geometry of the deformed Taylor cylinder mentioned in Fig. 6. Table 2 gives the position/diameter data from optical comparator measurements. Using Eqns (25) and (28), various undeformed section lengths were tried until agreement with the engineering strain in the specimen was achieved. Linear interpolation between measured cross sections was used to find the location 3.02 mm from the undeformed end. The strain at this location is about -0.119. Equations (25) and (28) can now be used to find $e = -0.116$ and $\beta = 0.741$.

With $\sigma_0 = \sigma_s/(1 + e) = -94\,\text{MPa}$ for this annealed copper, we find a dynamic yield stress of $\sigma = -310\,\text{MPa}$. The particle velocity is $u = \beta v_0 = 168\,\text{m/s}$, and the plastic wave speed is $\dot{h} = -(1 + (1 - \beta)/e)v_0 = 267\,\text{m/s}$. The results are in very good agreement with the one-dimensional expression of conservation of mass, energy and momentum with the incorporation of mechanical threshold stress constitutive behavior and Mie–Gruniesen equation of state [16, 17].

CONCLUSION

One of the most unreliable measurements in the Taylor test is the final undeformed section length. There is so much uncertainty associated with this length that many people have concluded that it is impossible to ascertain dynamic yield stress when this measurement is involved. The analysis presented in this paper has removed some of the uncertainty associated with the undeformed section length by replacing it with a position measurement corresponding to a particular value of strain. This produces very satisfactory results on the basis of dynamic yield stress estimates.

Another standard that can be applied to the results is the comparison with early time behavior provided by the film record. Once the strain e_0 and the dimensionless constant β have been found, Eqn (13) can be used to estimate plastic wave motion during the initial transient stage of the deformation process. For the shots discussed in this paper for half-hard
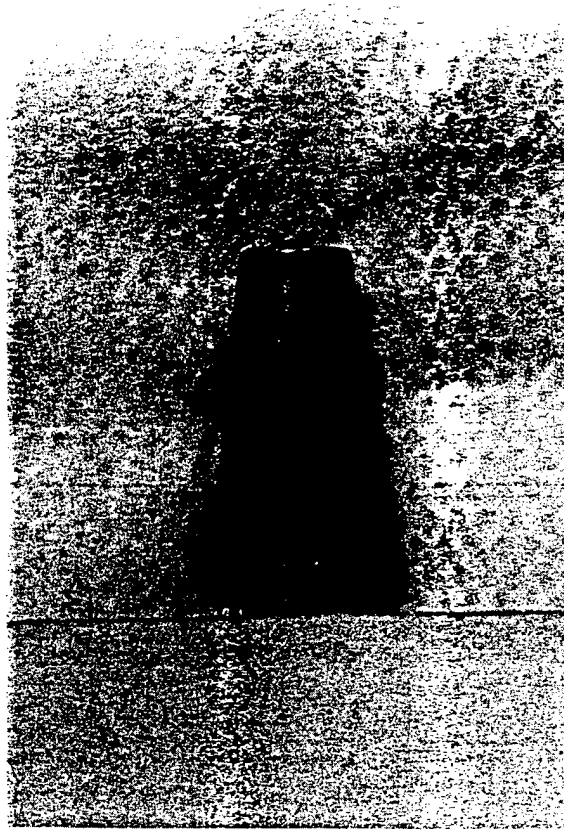
Fig. 7. Final geometry of a recovered OFHC copper impact specimen. The impact velocity was 227 m/s, and the specimen was annealed. Note the considerable distinction between this geometry and that shown in Fig. 5.

Table 2.

Axial position (mm)	Rod diameter (mm)	Axial position (mm)	Rod diameter (mm)	Axial position (mm)	Rod diameter (mm)
0.00	7.60	8.26	9.45	16.51	10.59
0.64	7.62	8.89	9.63	17.15	10.64
1.27	7.75	9.53	9.70	17.78	10.49
1.91	7.90	10.16	9.86	18.42	10.52
2.54	8.05	10.80	9.96	19.05	10.54
3.18	8.18	11.43	10.08	19.69	10.67
3.81	8.33	12.07	10.11	20.32	11.10
4.45	8.51	12.70	10.21	20.96	11.96
5.08	8.69	13.34	10.31	21.59	13.03
5.72	8.89	13.97	10.39	22.23	14.15
6.35	9.07	14.61	10.44	22.38	14.30
6.99	9.20	15.24	10.59		
7.62	9.35	15.88	10.57		

OFHC copper and annealed OFHC copper, the comparisons are shown in Figs 8 and 9. Obviously, the agreement is very favorable, indicating that the representation for early particle velocity in Eqn (17) is suitable. A more detailed discussion of the particle velocity at the plastic wave front is contained in [15].
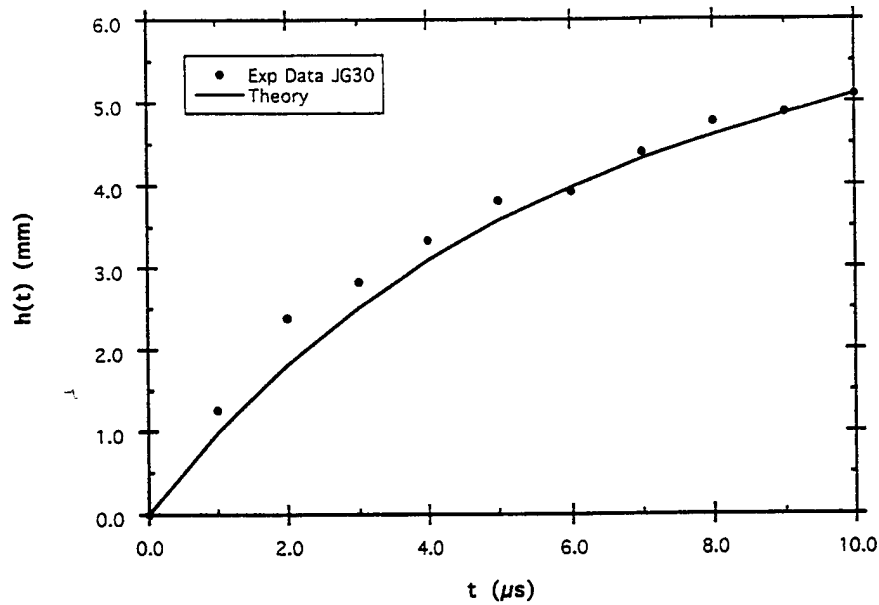
Fig. 8. Early time motion of the plastic wave front for a half-hard OFHC copper specimen.
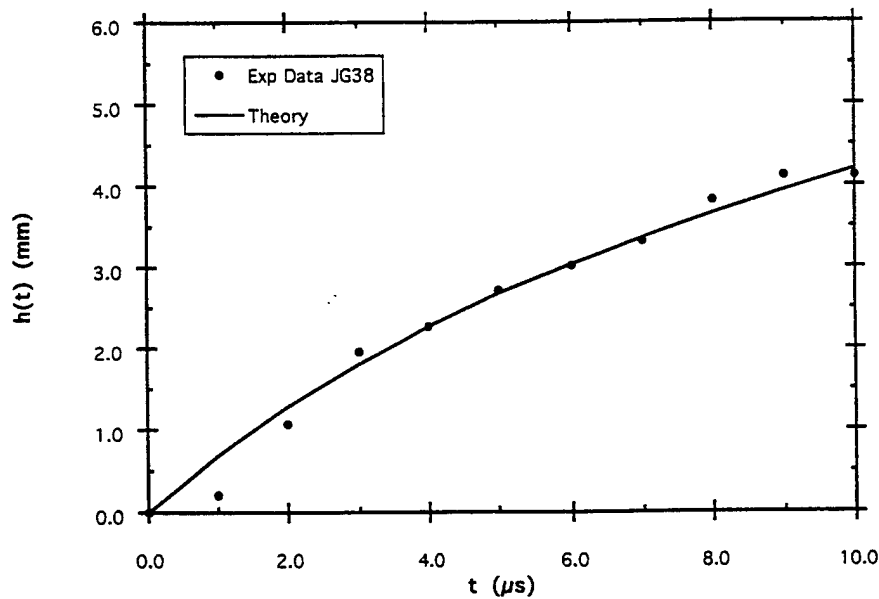
Fig. 9. Early time motion of the plastic wave front for an annealed OFHC copper specimen.

The theory introduced in this paper agrees precisely with that produced in [17] by other means. Additionally, the computational results presented in [16] lend further credibility to methods employed to reach such a satisfying conclusion. However, one important element is missing. A suitable estimate for strain-rate has not been given. Future efforts will concentrate on supplying strain-rate information and reporting results for other materials.

REFERENCES

1. Taylor. G. I., The use of flat-ended projectiles for determining dynamic yield stress I. Theoretical considerations. *Proc. Roy. Soc. London. Series A*, 1948, **194**, 289.
2. Whiffen. A. C., The use of flat-ended projectiles for determining dynamic yield stress II. Tests on various metallic materials. *Proc. Roy. Soc. London. Series A*, 1948, **194**, 300.
3. Lee. E. H. and Tupper, S. J., Analysis of plastic reformation in a steel cylinder striking a rigid target. *J. Appl. Mech., Trans. ASME*, 1954, **21**, 63.
4. Hawkyard. J. B., A theory for the mushrooming of flat-ended projectiles impinging on a flat rigid anvil. using energy considerations. *Int. J. Mech. Sci.*, 1969, **11**, 313.
5. Hawkyard, J. B., Easton, D. and Johnson. W., The mean dynamic yield strength of copper and low carbon steel at elevated temperatures from measurements of the 'mushrooms' of flat-ended projectiles. *Int. J. Mech. Sci.*, 1968, **10**, 929.
6. Barenblatt. G. I. and Ishlinskii, A. I., On the impact of a viscoplastic bar on a rigid wall. *Prikl. Math. Mekh.*, 1962, **26**, 497.
7. Ting, T. C. T., Impact of a nonlinear viscoplastic rod on a rigid wall. *J. Appl. Mech. Trans. ASME*, 1966, **33**, 505.
8. Hutchings. I. M., Estimation of yield stress in polymers at high strain-rates using G. I. Taylor's impact technique. *J. Mech. Phys. Solids*, 1979, **26**, 289.
9. Wilson, L. L., House, J. W. and Nixon. M. E., Time resolved deformation from the cylinder impact test AFATL-TR-89-76 (November 1989).
10. Johnson, G. R. and Holmquist T. J., Evaluation of cylinder-impact test data for constitutive model constants. *J. Appl. Phys.*, 1988, **64**, 3901.
11. Maudlin. P. J., Davidson, R. F. and Henninger, R. J., Implementation and assessment of the mechanical-threshold-stress model using the EPIC2 and PINON computer codes. Los Alamos National Laboratory report LA-11895-MS (September 1990).
12. Jones. S. E., Gillis. P. P. and Foster, Jr., J. C., On the equation of motion of the undeformed section of a Taylor impact specimen. *J. Appl. Phys.*, 1987, **61**, 499.
13. Jones, S. E., Gillis, P. P., Foster, Jr, J. C., and Wilson, L. L., A one-dimensional two-phase flow model for Taylor impact specimens. *J. Engr. Mat'ls. Tech., Trans. ASME*, 1991, **113**, 228.
14. Cinnamon, J. D., Jones, S. E., Foster, Jr. J. C. and Gillis, P. P., An analysis of early time deformation rate and stress in the Taylor impact test. *Mechanical Behavior of Materials—VI, Proc. of the Sixth Int. Materials Conf.*, Kyoto, Japan, July 1991, Vol. 1, eds. M. Jano and T. Inoue, p. 337 (1991).
15. Jones, S. E., Maudlin, P. J., Gillis, P. P. and Foster, Jr, J. C., An analytical interpretation of high strain rate material behavior during early time plastic deformation in the Taylor impact test. *Computers in Engineering 1992*, ed. G. A. Gabriele, Vol. 2, p. 173 ASME, New York (1992).
16. Maudlin, P. J., Foster, Jr, J. C. and Jones. S. E., On the Taylor test. Part III: a continuum mechanics code analysis of plastic wave propagation. Los Alamos National Laboratory report LA-12836-MS (November 1994).
17. Foster, Jr, J. C., Maudlin, P. J. and Jones. S. E., On the Taylor test. Part I: A continuum analysis of plastic wave propagation. *Proc. of the 1995 APS Topical Conf. an Shock Compression of Condensed Matter*, Seattle, Washington, p. 291 (August 1995).

APPENDIX E

A CONTINUUM MECHANICS CODE ANALYSIS OF STEADY PLASTIC WAVE PROPAGATION IN THE TAYLOR TEST

P. J. MAUDLIN,[†] J. C. FOSTER, JR.[‡] and S. E. JONES[§]

[†] Group T-3, Theoretical Division. Los Alamos National Laboratory, Los Alamos, NM 87545
[‡] Wright Laboratory, Armament Directorate. Eglin Air Force Base. FL 32542-6810. U.S.A., and
[§] Department of Aerospace Engineering and Mechanics. The University of Alabama. Tuscaloosa,
AL 35487, U.S.A.

Summary—Simple conservation relationships (jump conditions) in conjunction with postulated material constitutive behavior are applied to steady plastic strain waves propagating in problems of uniaxial stress and Taylor Cylinder Impact. These problems are simulated with a two-dimensional Lagrangian continuum mechanics code for the purpose of numerically validating the jump relationships as an accurate analytical representation of plastic wave propagation. The constitutive behavior used in this effort assumes isotropy and models the thermodynamic response with a Mie–Grunisen Equation-of-State and the mechanical response with the rate-dependent Johnson–Cook and MTS flow stress models. The jump relationships successfully replicate the results produced by continuum code simulations of plastic wave propagation and provide a methodology for constructing mechanical constitutive models from experimental plastic wave speed information. Comparisons are also presented between experimental speeds from Taylor Cylinder Impact tests with jump relationships and continuum code predictions. indicating that the above mentioned flow stress models may not accurately capture plastic wave propagation speeds in annealed and hardened copper. Copyright © 1997 Elsevier Science Ltd.

Keywords: plastic wave propagation. Taylor cylinder test. jump conditions

1. INTRODUCTION

For many years researchers have inferred high-rate mechanical constitutive behavior for metals from both static and dynamic plastic wave propagation data [1–6]. The cylinder impact test was first utilized by Taylor [1] to estimate an average dynamic flow stress from final recovered (static) cylinder shapes. Von Karman and Duwez [7], Kolsky [8], and Malvern [9] postulated the constitutive behavior for a uniaxial stress problem and then integrated an equation-of-motion by the method-of-characteristics in order to predict plastic strain wave profiles. These wave profiles were later compared to static experimental data, e.g. Kolsky and Douch [10], to validate the constitutive model.

More recently, time-resolved (dynamic) plastic strain wave data [4–6] obtained via high-speed photography of an impact event have been used in an attempt to validate high-rate plasticity models used in continuum mechanics codes: the work at Eglin AFB [5] focuses upon producing a propagating plastic wave in a cylindrical metallic specimen, and ideally, the test should be of sufficient duration such that a *steady* propagation can be observed. The information extracted from this dynamic test can be combined with conservation jump relationships [11] that are applied across a plastic strain wave front to map out the material's constitutive behavior in a three-dimensional stress, strain, and strain-rate space [12, 13]. In fact the constitutive behavior so determined is really a combination of the material's mechanical and thermodynamic behavior. If the material's thermodynamic behavior is assumed to be known (i.e. the jump relationships can be combined with an accepted equation-of-state, e.g. see [14]), then the theoretical analysis and comparison to experimental data can be focused solely on the material's mechanical behavior. Section 2 develops such a mathematical description of the mechanical behavior of a material that is then compared directly with uniaxial stress continuum code calculational results in Section 3, followed by Taylor Anvil calculations and experimental data in Section 4. A summary and conclusions are given in Section 5.

2. ONE-DIMENSIONAL STEADY WAVE RELATIONSHIPS

The steady state conservation jump equations developed by Foster *et al.* [12] for a control volume attached to a wave of plastic strain are repeated in this section for further development. Strength constitutive behavior and an equation-of-state (EOS) are combined with these jump equations in order to derive a set of material specific relationships. The von Mises [15] yield surface, the Johnson–Cook (JC) [16, 17] and MTS [18, 19] flow stress models. and a Mie–Grunisen [14] EOS are the constitutive equations used in this section to augment the jump relationships. Obviously this choice of constitutive behavior is not unique, but should be familiar to most readers and will illustrate the main technical points. The analysis assumes the one-dimensional steady propagation of a plastic strain wave.

2.1. *Preliminaries*

Defining σ as the Cauchy stress tensor and $d\varepsilon$ as a true incremental strain (natural strain) tensor measured in the laboratory frame and denoting the deviatoric stress and incremental strain tensors by s and de, respectively. the relationship between these is given in the usual way using indicial notation:

$$\sigma_{ij} = s_{ij} + \delta_{ij}\frac{1}{3}\sigma_{kk} \tag{1a}$$

and

$$d\varepsilon_{ij} = de_{ij} + \delta_{ij}\frac{1}{3}d\varepsilon_{kk}. \tag{1b}$$

If we now assume elastoplastic constitutive behavior and decompose the strain increment into elastic and plastic parts:

$$d\varepsilon_{ij} = d\varepsilon_{ij}^e + d\varepsilon_{ij}^p, \tag{2}$$

the same decomposition in terms of deviatoric strains is obtained after combining Eqns (1b) and (2),

$$de_{ij} = de_{ij}^e + de_{ij}^p. \tag{3}$$

If plastic volume incompressibility is assumed (i.e., $d\varepsilon_{kk}^p = 0$), then combination of the above strain relationships gives

$$d\varepsilon_{ij}^p = de_{ij}^p. \tag{4}$$

The true incremental strain tensor can be expressed in terms of the rate-of-deformation tensor (natural strain-rate tensor) multiplied by a time increment [20] as

$$d\varepsilon_{ij} = D_{ij}dt, \tag{5}$$

where the rate-of-deformation tensor is the symmetric part of the velocity gradient tensor $[L_{ij} = \partial u_i/\partial x_j]$:

$$D_{ij} = \frac{1}{2}(L_{ij} + L_{ji}). \tag{6}$$

Here x_i is the Eulerian position coordinate and u_i is the particle velocity. Usually the velocity gradient and time step information is readily available during a continuum mechanics code calculation.

Consider the axi-symmetric cylindrical geometry of radius r shown in Fig. 1. An areal strain can be defined with respect to the current configuration using a sign convention chosen to give a negative value for compression:

$$e_A \equiv \frac{A_0}{A} - 1, \tag{7a}$$

where A_0 is the initial undeformed area and A is the current area. Taking the differential of Eqn (7a) gives

$$de_A = -\frac{A_0}{A}\frac{dA}{A}, \tag{7b}$$
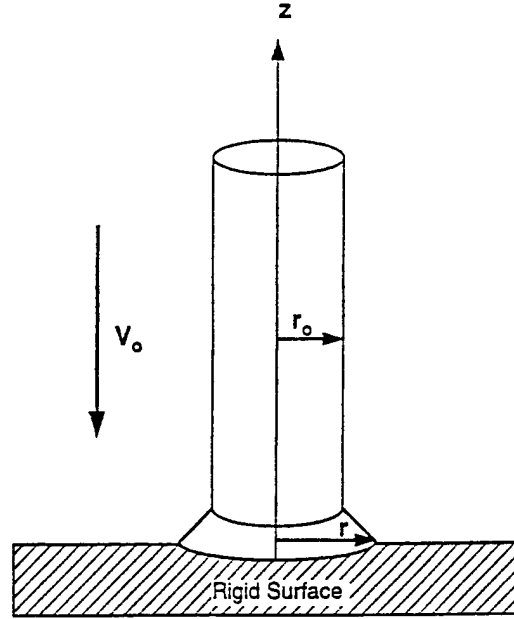
Fig. 1. Schematic of the Taylor Cylinder Impact Test.

where the circular cross-sectional differential area is

$$dA = 2\pi r dr. \tag{8}$$

Substituting Eqn (8) into Eqn (7b) and using πr^2 for A relates the areal strain to a radial strain increment, that is replaced with the radial component of the rate-of-deformation gradient from Eqn (5) [20]:

$$de_A = -2\frac{A_0}{A}\frac{dr}{r} = -2\frac{A_0}{A}d\varepsilon_{rr} = -2\frac{A_0}{A}D_{rr}dt. \tag{9a}$$

Decomposing the radial strain appearing in Eqn (9a) into elastic and plastic parts and using plastic incompressibility to relate radial and axial plastic increments (noting that for the centerline of the geometry shown in Fig. 1 the transverse strain increments $d\varepsilon_{rr}$ and $d\varepsilon_{\theta\theta}$ are equal) give for the areal strain:

$$de_A = -2\frac{A_0}{A}[d\varepsilon_{rr}^e + d\varepsilon_{rr}^p] = \frac{A_0}{A}[-2d\varepsilon_{rr}^e + d\varepsilon_{zz}^p]; \tag{9b}$$

and if the radial elastic strain increment is neglected, we obtain the statement that the areal strain increment defined by Eqn (7b) is approximately

$$de_A \cong \frac{A_0}{A}d\varepsilon_{zz}^p = \frac{A_0}{A}de_{zz}^p. \tag{10}$$

We also define a volumetric strain increment referenced to the initial configuration as

$$d\varepsilon_v \equiv \frac{dv}{v_0} = \frac{v}{v_0}\frac{dv}{v} = \frac{v}{v_0}d\varepsilon_{kk}, \tag{11}$$

where v is the specific volume, and the sign has been chosen to be positive for tension, consistent with common convention. If we decompose Eqn (11) into elastic and plastic parts, again using plastic incompressibility, the result for metals is

$$d\varepsilon_v = \frac{v}{v_0}d\varepsilon_{kk}^e. \tag{12}$$

E- 3

Integration of Eqn (11) from time t_0 to time t yields a definition of volumetric strain needed for the discussion in Section 3:

$$\varepsilon_v \equiv \int_{v_o}^{v} \frac{dv'}{v_0} = \frac{v}{v_0} - 1. \tag{13}$$

Also needed for the comparison to Kolsky's plastic wave analysis [8] discussed in Section 3 is the definition of an increment of *small Lagrangian strain*:

$$dE_{ij} = \frac{1}{2}[L_{im}F_{mj} + L_{jm}F_{mi}]dt, \tag{14}$$

where F_{ij} is the deformation gradient representing the change in the Eulerian spatial position with respect to a change in the Lagrangian coordinate:

$$F_{ij} = \frac{\partial x_i}{\partial X_j}. \tag{15}$$

Even though the definition of incremental finite Lagrangian strain would be more appropriate for the larger magnitudes of strain realized in Kolsky's plastic wave analysis, i.e.

$$dE_{ij} = F_{mi}D_{mn}F_{nj}dt. \tag{16}$$

The definition of small strain given by Eqn (14) is used in this work to be historically consistent with von Karman and Duwez [7] and Kolsky [8].

2.2. *Conservation relationships*

From Foster *et al.* [12], the jump equations [11] for mass, momentum, and energy across a one-dimensional steady strain wave from the perspective of a reference frame attached to the wave and moving with wave velocity u_w are, respectively,

$$u_w = \frac{-u_1}{(e_A + \varepsilon_v + e_A\varepsilon_v)}, \tag{17a}$$

$$\frac{\sigma_1}{(1 + e_A)} - \sigma_0 = -\rho_0 u_w u_1, \tag{17b}$$

$$\rho_0(i_1 - i_0) = (e_A + \varepsilon_v + e_A\varepsilon_v)\frac{1}{2}\left(\frac{\sigma_1}{(1 + e_A)} + \sigma_0\right), \tag{17c}$$

where Eqn (17c) has been manipulated with Eqns (17a) and (17b) to eliminate the particle and wave velocities giving the energy jump in a stress work form. In this equation set ρ is the material density, u is the material particle velocity, and i is the specific internal energy. The subscript "o" refers to quantities in front of the wave, the subscript "1" refers to quantities just behind the wave, and the subscript w denotes a wave velocity. Note that u_1 is observed with respect to the inertial reference frame moving with constant velocity u_w. Equations (17) represent three equations containing the six unknowns u_w, u_1, e_A, ε_v, σ_1, i_1.

Also from Foster *et al.* [12], if Eqns (17a) and (17b) are manipulated to eliminate first the particle velocity u_1 and then the wave velocity u_w, the following two relationships are obtained:

$$\sigma_1 = (1 + e_A)[\sigma_0 + \rho_0 u_w^2(e_A + \varepsilon_v + e_A\varepsilon_v)] \tag{18}$$

$$\sigma_1 = (1 + e_A)\left[\sigma_0 + \frac{\rho_0 u_1^2}{(e_A + \varepsilon_v + e_A\varepsilon_v)}\right]. \tag{19}$$

2.3. *Constitutive relationships*

Specification of a yield surface provides an equation relating the deviatoric stress to a yield stress or flow stress (σ). Here we use the von Mises surface [15] and a flow stress model that is

functionally dependent on equivalent plastic strain (ε^p), strain-rate $(\dot{\varepsilon}^p)$, and temperature (T):

$$\frac{3}{2} s_{ij} s_{ij} = \sigma^2(\varepsilon^p, \dot{\varepsilon}^p, T). \tag{20}$$

where the equivalent plastic strain-rate is defined as

$$\dot{\varepsilon}^p = \sqrt{\frac{2}{3} D_{ij}^p D_{ij}^p}, \tag{21}$$

and the equivalent plastic strain is the time integral of Eqn (21):

$$\varepsilon^p = \int_{t_0}^{t} \dot{\varepsilon}^p dt. \tag{22}$$

For a one-dimensional geometry (or at the centerline of the cylinder shown in Fig. 1), the deviatoric stresses s_{rr} and $s_{\theta\theta}$ are both equal to $-s_{zz}/2$. This statement plus the assumption of negligible shear simplifies Eqn (20) to

$$s_{zz} = \pm \frac{2}{3} \sigma. \tag{23}$$

Two flow stress models are investigated here: the Johnson–Cook [16, 17] model and the MTS [18, 19, 21] model. The Johnson–Cook model has the simple form

$$\sigma = [\sigma_0 + B(\varepsilon^p)^n][1 + C \ln(\dot{\varepsilon}^p)]\left[1 - \left(\frac{T - T_r}{T_m - T_r}\right)^m\right]. \tag{24}$$

The first factor in Eqn (24) represents strain hardening with σ_0 interpreted as the initial yield stress, B is a strain-hardening coefficient, and n is a strain-hardening exponent. The second factor accounts for strain-rate hardening effects with C being a strain-rate hardening coefficient. The last factor represents thermal softening relative to room temperature (T_r), decreasing to zero as the melting point (T_m) is realized; the quantity m is a softening exponent. Johnson–Cook constants for copper are given in Table 1.

The MTS model is expressed here in specific form for copper [21] (forms for other materials can be slightly more complicated):

$$\sigma = \hat{\sigma}_a + s_{th} \hat{\sigma}. \tag{25}$$

The product in Eqn (25) contains a micro-structure evolution variable, i.e. $\hat{\sigma}$, called the mechanical threshold stress, that is multiplied by a constant-structure deformation variable s_{th}; s_{th} is a function of temperature T and plastic strain-rate $\dot{\varepsilon}^p$. The athermal threshold stress $\hat{\sigma}_a$ represents dislocation interactions with long-range barriers such as grain boundaries and is typically assumed to be constant. The complementary equation to Eqn (25) is a differential hardening law representing dislocation–dislocation interaction:

$$\frac{\partial \hat{\sigma}}{\partial \varepsilon^p} = \Theta_0 \left[1 - F\left(\frac{\hat{\sigma}}{\hat{\sigma}_s}\right)\right]. \tag{26}$$

Table 1. Johnson–Cook model constants for annealed copper

Parameter	Description	Nominal value
σ_0	Initial yield stress	89.6 MPa
B	Strain hardening coefficient	292.0 MPa
C	Strain-rate hardening coefficient	0.025
n	Strain hardening exponent	0.31
m	Temperature softening exponent	1.09
T_r	Room temperature	294.0 K
T_m	Melting temperature	1356.0 K

In this equation Θ_0 represents hardening due to dislocation generation. and the product $\Theta_0 \cdot F$ represents softening due to dislocation recovery. The threshold stress at zero strain-hardening $\hat{\sigma}_s$ is called the saturation threshold stress. Relationships for F. Θ_0. $\hat{\sigma}_s$ are material specific: for copper these relationships are [21]

$$F\left(\frac{\hat{\sigma}}{\hat{\sigma}_s}\right) = \frac{\tanh(2\hat{\sigma}/\hat{\sigma}_s)}{\tanh(2)}, \tag{27}$$

$$\Theta_0 = a_0 + a_1 \ln(\dot{\varepsilon}^p) + a_2 \sqrt{\dot{\varepsilon}^p}, \tag{28}$$

$$\hat{\sigma}_s = \hat{\sigma}_{so} \left(\frac{\dot{\varepsilon}^p}{\dot{\varepsilon}_{so}}\right)^{kT/Gb^3 A} - \hat{\sigma}_a, \tag{29}$$

where (a_0, a_1, a_2) are material constants. Θ_0 has a maximum value constrained to the shear modulus. k is Boltzmann's constant $(1.36 \times 10^{-23}$ J/K), G is the shear modulus assumed to be temperature and possibly pressure dependent, b is the magnitude of Burgers vector (the inter atomic distance in the slip direction), $\hat{\sigma}_{so}$ is the saturation threshold stress at 0 K. $\dot{\varepsilon}_{so}$ is a reference strain-rate. and the quantity A is a material constant. The shear modulus appearing in these equations is assumed to be a function of temperature and given by the correlation $G = b_0 - b_1/(e^{b_2/T} - 1)$. At room temperature this equation gives a value of 42.9 GPa for copper.

If the temperature and strain-rate are both assumed to be constant and a Voce [19] law is used for the F function, then Eqn (26) can be integrated for the threshold stress giving the closed-form solution

$$\hat{\sigma} = \hat{\sigma}_s \left[1 - \left(1 - \frac{\hat{\sigma}_0}{\hat{\sigma}_s}\right)\exp\left(-\frac{\Theta_0}{\hat{\sigma}_s}\varepsilon^p\right)\right]. \tag{30}$$

This relationship can then be substituted into Eqn (25) to yield an analytical expression for the flow stress.

For *thermal-activation controlled deformation*, s_{th} is evaluated via an Arrhenius rate equation:

$$s_{th} = \left[1 - \left(\frac{kT\ln(\dot{\varepsilon}_0/\dot{\varepsilon}^p)}{Gb^3 g_0}\right)^{1/q}\right]^{1/p}. \tag{31}$$

The exponents p and q are material constants, $\dot{\varepsilon}_0$ is a reference strain-rate, and g_0 is a normalized activation energy for a given dislocation/obstacle interaction, assumed to be a constant. The reader is referred to Refs [18] and [19] for more detail concerning the development of Eqns (25)–(31). MTS constants for copper are given in Table 2.

Table 2. MTS Model constants for annealed copper

Parameter	Description	Nominal value
$\hat{\sigma}_a$	Rate independent threshold stress	40.0 MPa
g_0	Normalized activation energy	1.6
$\dot{\varepsilon}_0$	Thermal activation equation constant	10^7 s^{-1}
b	Magnitude of Burgers vector	2.55 Å
A	Saturation stress equation constant	0.312
$\hat{\sigma}_0$	Initial threshold stress	46.0 MPa
$\hat{\sigma}_{so}$	Saturation stress at zero degrees K	900.0 MPa
$\dot{\varepsilon}_{so}$	Saturation stress reference strain rate	6.2×10^{10} s^{-1}
p	Free energy equation exponent	2/3
q	Free energy equation exponent	1
a_0	Hardening function constant	2370.7 MPa
a_1	Hardening function constant	8.295 MPa
a_2	Hardening function constant	3.506 MPa
b_0	Shear modulus constant	47.3 GPa
b_1	Shear modulus constant	2.40 GPa
b_2	Shear modulus constant	130 K

The concept of a plastic wave propagation speed is used to compare the constitutive moduli to plastic wave speeds observed in continuum calculations and time-resolved tests. Therefore, we follow von Karman and Duwez [7] and Kolsky [8] by relating the wave speed to the partial derivative of the stress with respect to strain suggested by a method-of-characteristics solution of the equation of motion for the uniaxial stress problem:

$$u_x^2 = \frac{1}{\rho_0} \frac{\partial \sigma_{zz}}{\partial E_{zz}}, \tag{32}$$

where ρ_0 is the initial density and E_{zz} is the small Lagrangian strain given by Eqn (14). In order to further develop the wave speed given by Eqn (32), using either the Johnson–Cook or MTS model, the partial derivative of flow stress with respect to equivalent strain is needed. Thus we have for the former:

$$\frac{\partial \sigma_{JC}}{\partial \varepsilon^p} = Bn(\varepsilon^p)^{n-1} [1 - c \ln(\dot{\varepsilon}^p)] \left[1 - \left(\frac{T - T_r}{T_m - T_r} \right)^m \right] \tag{33}$$

and for the latter

$$\frac{\partial \sigma_{MTS}}{\partial \varepsilon^p} = s_{th} \Theta_0 \left[1 - F\left(\frac{\hat{\sigma}}{\hat{\sigma}_s} \right) \right]. \tag{34}$$

There are several approaches for combining the flow stress models represented by Eqns (24) and (25) with the jump equations given by Eqns (17). In this effort, the combination is performed using the energy jump equation, a Mie–Grunisen EOS, and a von Mises yield function. We proceed with a Mie–Grunisen EOS (or nonlinear elasticity) using the quadratic form:

$$P = (k_1 \mu + k_2 \mu^2 + k_3 \mu^3) \left(1 - \frac{\Gamma}{2} \mu \right) + i\rho_0 \Gamma (1 + \mu), \tag{35}$$

where the compression $\mu \equiv \rho/\rho_0 - 1$ can be related to the volumetric strain defined above as $\mu = -\varepsilon_v/(1 + \varepsilon_v)$, and the pressure P is the negative of one-third of the trace of the total stress tensor, i.e. in view of Eqn (1a),

$$\sigma_1 = \sigma_{zz} = s_{zz} - P. \tag{36}$$

The EOS parameters appearing in Eqn (35) are defined in Table 3.

The EOS given by Eqn (35) can be inverted for the internal energy and substituted into the energy jump Eqn (17c) to eliminate i. If we also substitute for the pressure using Eqn (36), assume Eqn (23) applies (valid for one-dimensional behavior and also along the centerline of a cylindrical two-dimensional geometry), and solve for σ_1, then we obtain an analogous Hugoniot [11] result:

$$\sigma_1 = -\frac{\frac{1}{2}(e_A + \varepsilon_v + e_A \varepsilon_v)\sigma_0 + i_0 \rho_0 + \frac{1}{\Gamma(1 + \mu)} \left[\frac{2}{3} \sigma + (k_1 \mu + k_2 \mu^2 + k_3 \mu^3) \left(1 - \frac{\Gamma}{2} \mu \right) \right]}{\frac{1}{\Gamma(1 + \mu)} + \frac{1}{2}(e_A + \varepsilon_v + e_A \varepsilon_v) \frac{1}{(1 + e_A)}}. \tag{37}$$

Table 3. MIE–Grunisen EOS constants for copper

Parameter	Description	Nominal value
k_1	Linear coefficient	137.0 GPa
k_2	Quadratic coefficient	175.0 GPa
k_3	Cubic coefficient	564.0 GPa
Γ	Grunisen coefficient	1.96
ρ_0	Initial density	8950.0 kg/m^3

If the volumetric strain is now assumed to be small, i.e., $|\varepsilon_v| \ll |e_A|$ and $|\varepsilon_v| \ll 1$, then Eqn (37) simplifies to

$$\sigma_1 = -\frac{\frac{1}{2}e_A\sigma_0 + i_0\rho_0 + \frac{1}{\Gamma}\left(\frac{2}{3}\sigma - \varepsilon_v k_1\right)}{\frac{1}{\Gamma} + \frac{1}{2}\frac{e_A}{(1 + e_A)}}. \tag{38}$$

Recalling that the flow stress σ is assumed to be a function of plastic strain, strain-rate, and temperature, the axial stress given by Eqn (38) is thus a function of plastic strain, strain-rate, temperature, and volumetric strain (assumed to be small but not zero).

Equations (17a), (17b), and (38) now represent a set of three equations containing the seven unknowns u_w, u_1, e_A, ε_v, σ_1, σ, $\dot{\varepsilon}^P$.

2.4. *Uniaxial stress*

If we now focus on the uniaxial stress problem (i.e. the long wire problem), the pressure can be easily related to the flow stress. The stress state for uniaxial stress is

$$\sigma_{rr} = 0 \Rightarrow s_{rr} = P$$

$$\sigma_{\theta\theta} = 0 \Rightarrow s_{\theta\theta} = P \tag{39}$$

$$\sigma_{zz} = s_{zz} - P.$$

Since the trace of the deviatoric stress tensor is zero, the stress components are related as

$$s_{zz} = -2s_{rr}; \tag{40}$$

and then replacing the deviatoric stress components in Eqn (40) using Eqn (23) and Eqn (39), the pressure is simply:

$$P = \frac{1}{3}\sigma. \tag{41}$$

Also for uniaxial stress the expressions for equivalent stress and strain simplify to

$$\sigma = |\sigma_{zz}| \tag{42a}$$

$$\varepsilon^P = |\varepsilon_{zz}^P|. \tag{42b}$$

Formulating wave speeds via Eqn (32) (noting Eqn 42) for the two flow stress models represented by Eqns (33) and (34) gives

$$u_{w,JC} = \sqrt{\frac{1}{\rho_0}\frac{\partial\sigma_{JC}}{\partial\varepsilon^P}\frac{\partial\varepsilon_{zz}}{\partial E_{zz}}} \tag{43}$$

and

$$u_{w,MTS} = \sqrt{\frac{1}{\rho_0}\frac{\partial\sigma_{MTS}}{\partial\varepsilon^P}\frac{\partial\varepsilon_{zz}}{\partial E_{zz}}}, \tag{44}$$

where increments of elastic strain have been assumed to be negligible in using the chain-rule on the strain partial derivative under the radicals (i.e., $\varepsilon_{zz}^P \cong \varepsilon_{zz}$). The partial derivative of natural strain with respect to small Lagrangian strain appearing in Eqns (43) and (44) is obtained using the ratio of strain increments from Eqns (5) and (14)

$$\frac{\partial\varepsilon_{zz}}{\partial E_{zz}} = \frac{d\varepsilon_{zz}}{dE_{zz}} = \frac{D_{zz}}{L_{zz}F_{zz}} = F_{zz}^{-1}. \tag{45}$$

Since the displacement is equal to the difference between the Eulerian and Lagrangian positions. it then follows that $F_{zz} = E_{zz} + 1$ [20]; and. when substituted into Eqn (45) and integrated between t_0 and t. the two strain definitions are related as

$$\varepsilon_{zz} = \ln(E_{zz} - 1) = \ln(F_{zz}).$$ (46)

Combining Eqns (46), (45), and (43) or (44) gives the wave speed in terms of either Lagrangian small strain or natural strain.

The equivalent strain ε^p appearing in the above flow stress models is related to e_A via Eqn (10) as

$$\varepsilon^p = -\varepsilon_{zz}^p = -\int_0^{e_A} \frac{A}{A_0} de_A = -\int_0^{e_A} \frac{de_A}{(1 + e_A)} = -\ln(1 + e_A),$$ (47)

and the temperature T also appearing in the flow stress models can be easily related to the internal energy i.

Note that a comparison of Eqns (46) and (47) reveals that small Lagrangian strain E_{zz} and areal strain e_A are identical if we ignore elasticity.

Figure 2 presents the wave speed for annealed copper as computed from the flow stress models Eqns (43) and (44). The wave speed is given as a function of areal strain e_A with strain-rate indicated as a parameter. In general the wave speed is seen to always decrease with increasing strain. These results also indicate a rather large difference between the models of more than 200 m/s in wave speed and also reveal the insensitivity of the Johnson–Cook model to strain-rate. Taylor Cylinder test data discussed in more detail in Section 4 indicate that a plastic wave speed at the 5% strain level to be about 400 m/s for an annealed initial material condition. Thus the two flow stress models are seen to bracket this experimental speed.

For the long wire problem the radial and axial elastic strain increments are related via Poisson's ratio v so that Eqn (12) can be rewritten as

$$d\varepsilon_v = (1 - 2v) d\varepsilon_{zz}^e \frac{v}{v_0},$$ (48)
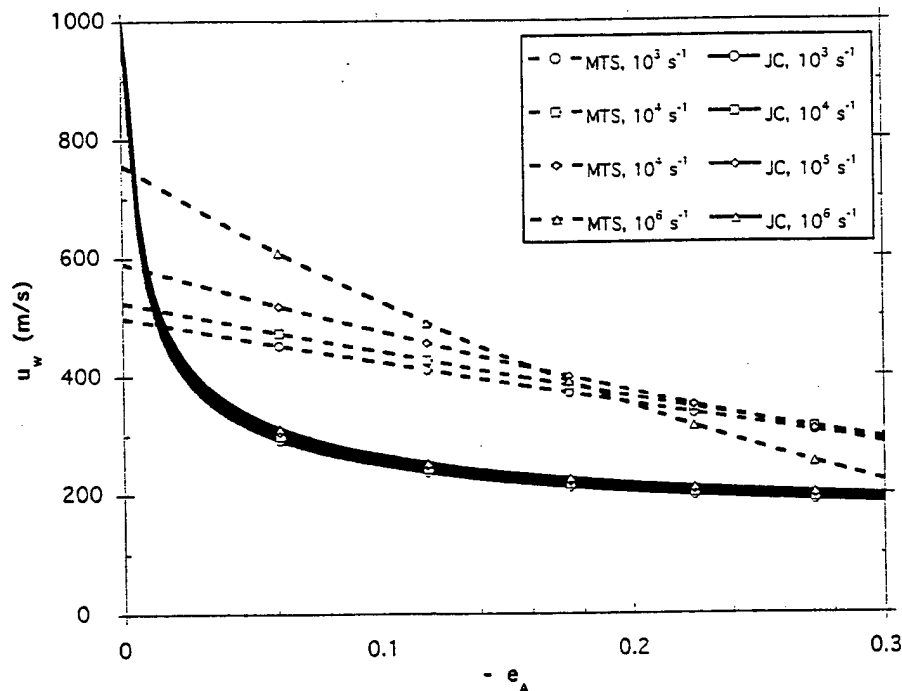
Fig. 2. Plastic wave speed shown as a function of areal strain with strain-rate indicated as a parameter. These curves are determined from a strain differential of the Johnson–Cook and MTS flow stress models. Note the deceleration trend as strain increases.

which integrates to

$$\varepsilon_v = e^{(1 - 2v)\varepsilon_a} - 1. \tag{49}$$

If this elastic axial strain is replaced with $-\sigma/E$ using Hooke's Law and Eqn (42a), the volumetric strain can be estimated for this uniaxial stress situation: taking the yield stress to be 200 MPa, Poisson's ratio to be 0.34, and Young's modulus to be 132 GPa, which are appropriate for copper, a value of -0.0485% is computed for ε_v.

Also, if we relate the change in temperature to the plastic work simply by

$$\Delta T = \frac{1}{\rho_0 C_p} \int_0^{\varepsilon^p} \sigma \, d\varepsilon^p \tag{50}$$

and say that for copper the density is 8950 kg/m^3 and the specific heat is 383 J/kg-K, then the temperature rise for a 5% plastic strain is only 3 K. Thus for plastic strain waves of roughly 5%, the thermal effect associated with the plastic work is small; and the temperature can be assumed constant for the evaluation of a flow stress.

A graphical representation of Eqn (38) is given by Fig. 3, which presents a family of stress σ_1 curves plotted as a function of strain e_A, with strain-rate $\dot{\varepsilon}^p$ indicated as a parameter ranging from 10^3 to 10^6 s^{-1}. These results are for a hardened copper having an initial yield stress of 293 MPa and a constitutive description corresponding to the MTS model. Also shown in Fig. 3 are curves of constant wave speed constructed using Eqn (18), with u_w ranging from 300 to 600 m/s, and curves of constant particle velocity constructed using Eqn (19), with u_1 ranging from 10 to 75 m/s. These curves identify the stress, strain, and strain-rate states realized behind a wave of constant plastic strain e_A. For example, say a compressive plastic strain wave of -6% is traveling along a wire with a speed of 500 m/s; from Fig. 3 the material behind this wave has a particle velocity of about 30 m/s from the perspective of the wave frame, an axial stress of -400 MPa, and a strain-rate of 10^5 s^{-1}. Figure 4 presents similar results for an annealed copper having an initial yield stress of
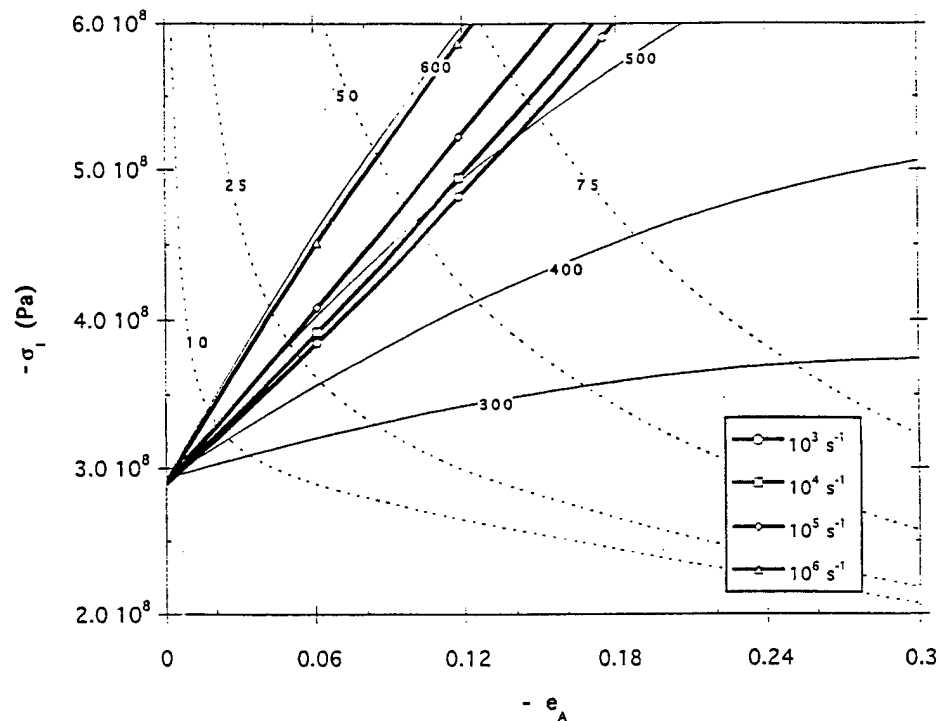

Fig. 3. Sress versus areal strain curves of constant wave speed, constant particle velocity, and analogue Hugoniots for hardened copper. Strain-rate is indicated as a parameter for the Hugoniot curves that incorporate the Mie–Grunisen EOS and MTS flow stress model. Units for the indicated speeds are in m/s.
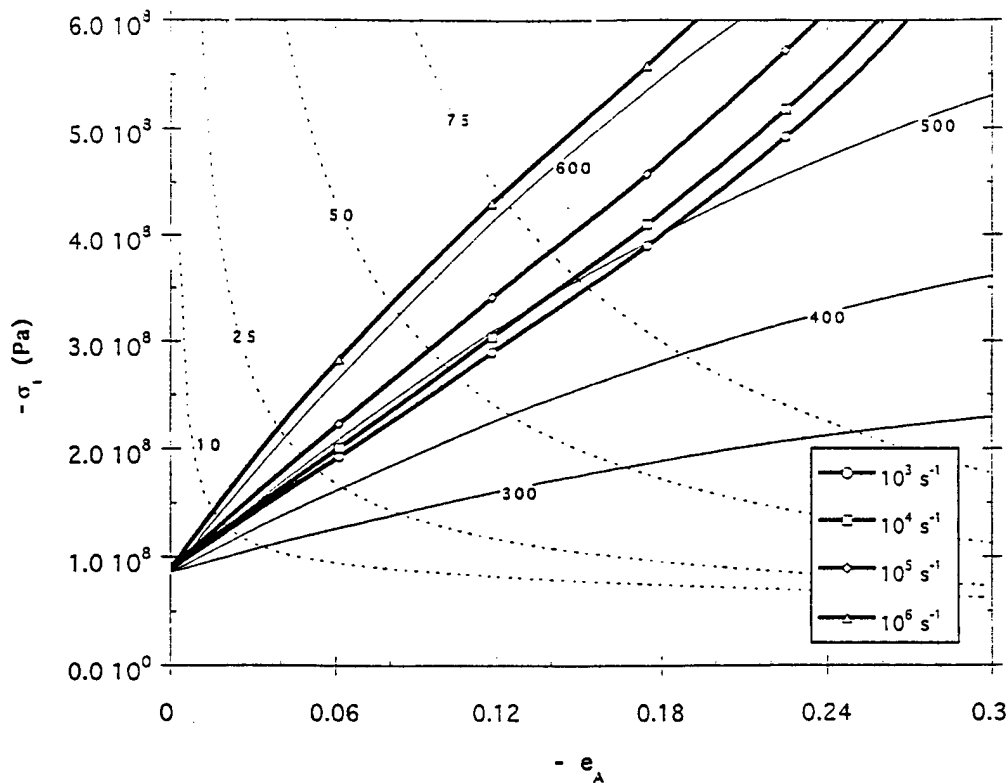
Fig. 4. Stress versus areal strain curves of constant wave speed, constant particle velocity, and analogue Hugoniots for annealed copper. Strain-rate is indicated as a parameter for the Hugoniot curves that incorporate the Mie–Grunisen EOS and MTS flow stress model. Units for the indicated speeds are in m/s.

86 MPa. Note that the annealed material has higher wave speeds when compared to the hardened material of Fig. 3 for similar values of strain and strain-rate. This observation can be understood if one notes Eqn (44) and considers the difference in slope between the stress–strain curves for the two materials.

Figures 5 and 6 present results analogous to Figs 3 and 4, but using instead the Johnson–Cook flow stress model to determine wave speed as indicated by Eqn (43). These figures indicate that the Johnson–Cook family of curves has a reasonable domain of intersection with the curves of constant wave speed and constant particle velocity over the range of strain-rates shown. Both the hardened and annealed results of Figs 5 and 6 indicate a plastic wave speed greater than 500 m/s at the 5% strain level. Taylor Cylinder test data discussed in more detail in Section 4 indicate that plastic wave speeds at the 5% strain level range from 300 to 400 m/s depending on initial material condition. The strong sensitivity of wave speed to strain is especially reflected in the Fig. 6 annealed results where u_w ranges from 700 down to 400 m/s as e_A increases from 0 to 15%; this observation was made indirectly by Wilson et al. in Ref. [5] for annealed copper.

3. A LONG WIRE ANALYSIS

A Lagrangian finite-element continuum mechanics code [22] was used to simulate the uniaxial stress problem (long wire problem) modeling the constitutive behavior with the relationships presented in Section 2.3. The purpose of these calculations was to evaluate the use of the jump relationships combined with the material's constitutive behavior (i.e. Eqns 35 and 24 or 25) by comparing with continuum code results.

Letting the Fig. 1 geometry represent a long wire (i.e. r becomes very small), the wire is set in motion at speed v_0 and impacts a rigid surface at time zero. The impact produces
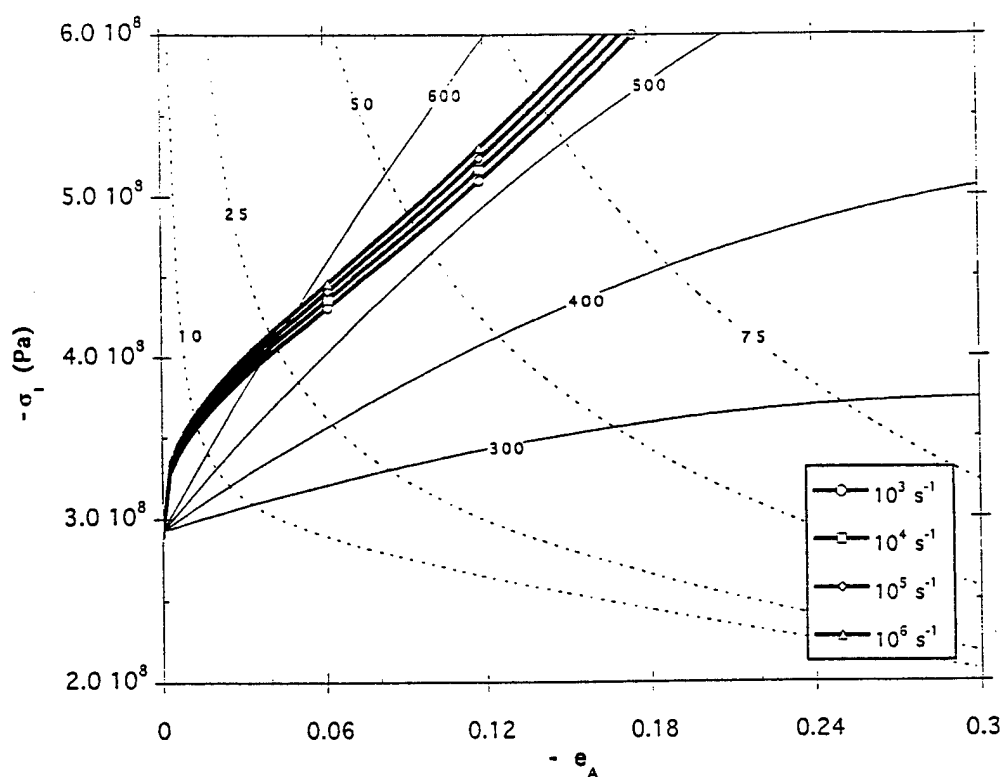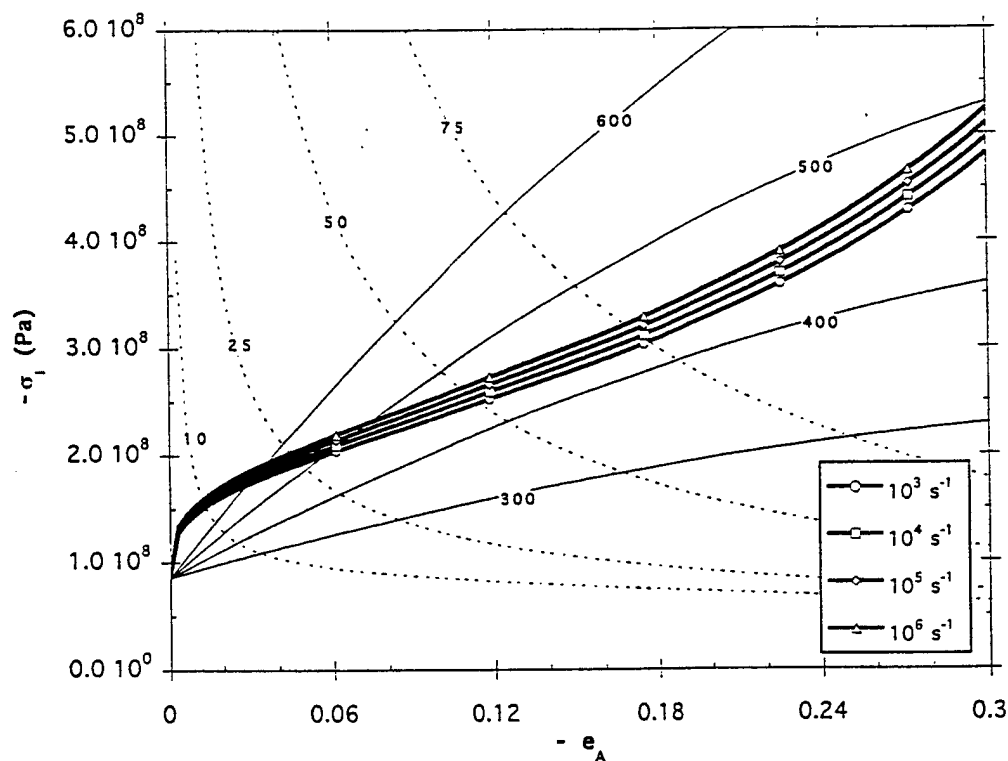
Fig. 5. Stress versus areal strain curves of constant wave speed, constant particle velocity, and analogue Hugoniots for hardened copper. Strain-rate is indicated as a parameter for the Hugoniot curves that incorporate the Mie–Grunisen EOS and Johnson–Cook flow stress model. Units for the indicated speeds are in m/s.

Fig. 6. Stress versus areal strain curves of constant wave speed, constant particle velocity, and analogue Hugoniots for annealed copper. Strain-rate is indicated as a parameter for the Hugoniot curves that incorporate the Mie–Grunisen EOS and Johnson–Cook flow stress model. Units for the indicated speeds are in m/s.

a compressive stress wave that propagates in the positive z direction. This wave separates into elastic and plastic parts [7, 8] with the plastic wave being of most interest to this analysis.

Continuum code calculations provide a means for numerically observing the plastic strain wave motion along the length of the impacting wire. A copper wire 5.08 cm (2 in.) long was modeled assuming a uniaxial stress geometry divided into 200 one-dimensional elements and given an initial speed v_0 of 0.1 km/s. In order to compare the speed of the plastic wave inferred from these calculations with that indicated by the constitutive modeling (Eqns 43 or 44), some criterion must be used to establish the Eulerian position $h(t)$ (defined as the distance from the rigid surface of the anvil face out to the plastic wave, see Fig. 1) of a plastic strain wave [5, 6]. In this study the axial plastic strain ε^p_{zz} discussed in Section 2.4 is applied along the wire to determine $h(t)$. An arbitrary value of -4.94% is used here for ε^p_{zz}, which corresponds to -4.82% for e_A, -4.82% for E_{zz}, and 2.5% for the radial bulge $(R - R_0)/R_0$. The choice of -4.94% here is arbitrary, but does reflect the resolution of the experimental optics at Eglin AFB [5] used for reduction of the time-dependent Taylor Cylinder data discussed in Section 4, and *must* be consistent with the experimentally observed radial bulge.

The discussion in this section first assumes a simple description for the material behavior (Eqn 51 below) in order to derive an analytic solution that can be compared to continuum calculations, and then more realistic material models (i.e. the Johnson–Cook and the MTS models) are investigated. The simple constitutive model is in fact identical to that used by Kolsky [8].

3.1. *Simple constitutive model*

Figure 7 presents the plastic strain wave position $h(t)$ as a function of time for a plastic strain of -4.94% propagating in the annealed copper wire with a constant plastic hardening modulus of 292 MPa., i.e. the flow stress is simply

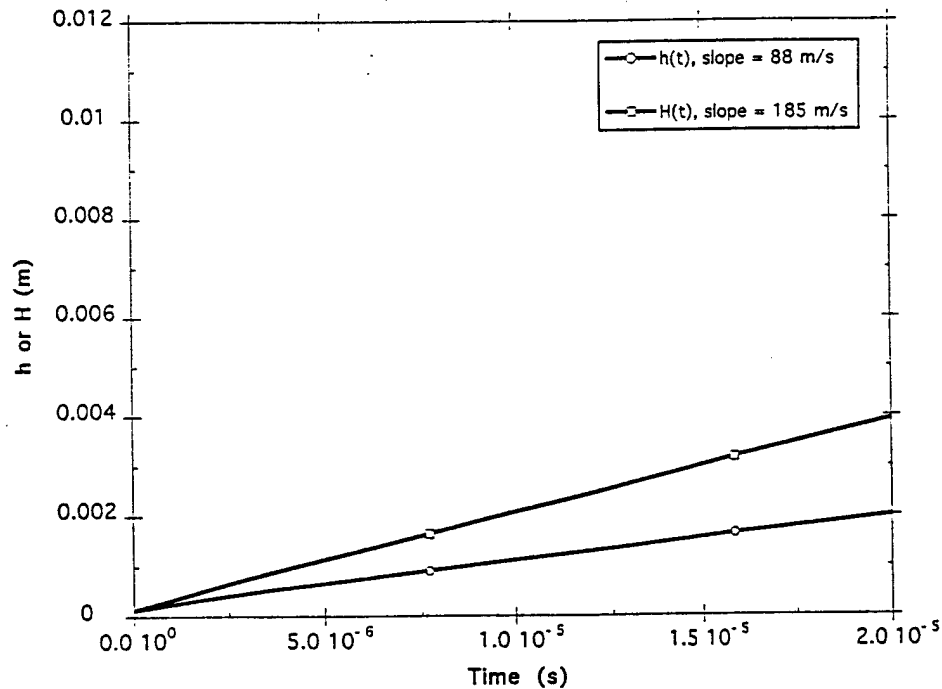$$\sigma = \sigma_0 + B |E_{zz}|. \tag{51}$$

Fig. 7. Wire problem plastic wave position curves using both Eulerian and Lagrangian position coordinates shown as a function of time. This calculation incorporates the Mie–Grunisen EOS and a simple strain-hardening flow stress model for annealed copper. Initial impact velocity is 100 m/s.

This simple flow stress model implies a wave speed obtained via Eqn 32 of

$$u_w = \sqrt{\frac{B}{\rho_0}},$$
(52)

which has a value of 0.181 km/s. The Fig. 7 code results show a wave traveling about 2.0 mm in 20 μs with a near constant slope $\dot{h}$ of 0.88 km/s. Also shown in Fig. 7 is the Lagrangian position $H(t)$ of the same plastic wave, which measures wave travel out to about 4.0 mm in 20 μs with a near constant $\dot{H}$ of 0.185 km/s. Both wave position curves are measured from the laboratory reference frame but using different metrics; the $H(t)$ curve in effect disregards the kinematical history of the material through which the plastic wave has propagated since it measures the wave position in terms of initial configuration coordinates. The slopes of the $h(t)$ and $H(t)$ curves in Fig. 7 differ by roughly v_0, i.e. 0.097 km/s; the elastic precursor wave moving out in front of the plastic wave at 3.66 km/s has decelerated the wire particle velocity by a few percent. If we account for the deceleration effects of the elastic precursor, then we have for the plastic wave

$$\dot{H} = \dot{h} - (v_0 - u_e),$$
(53a)

where the elastic jump velocity u_e can be obtained by solving Eqn (17b) for the particle velocity and setting σ_0 to zero, σ_1 to the initial yield stress, u_w to the elastic longitudinal wave speed (i.e. $\sqrt{E/\rho_0}$), and the strain to the elastic strain at yield:

$$u_e = \frac{\sigma_y}{(1 - \sigma_y/E)} \frac{1}{\sqrt{E\rho_0}}.$$
(53b)

This relationship gives 2.75 m/s for annealed copper having an initial yield of 86 MPa and 8.96 m/s for hardened copper having an initial yield of 293 MPa.

Recalling that u_w is the velocity of a reference frame attached to the plastic strain wave, this frame observes material entering the wave front with a particle velocity of $-u_w$ and material exiting from behind the wave front with a particle of $-(u_w - u_1)$; i.e. the plastic wave frame does not "recognize" the particle velocity of the medium through which it is moving [11]. Therefore the slope of the $H(t)$ curve in Fig. 7 or $\dot{H}$ should be identical to the wave speed u_w of 0.181 km/s for a steady state wave propagation; the explanation for the 2% difference between these speeds is discussed below.

Figure 8 presents plastic strain profiles for the wire problem in terms of small Lagrangian strain E_{zz} versus the characteristic variable Z/t where Z is the Lagrangian axial position. These profiles are given at three locations along the wire: $Z = 1.27, 2.54$, and 7.62 mm. Kolsky [8] provides an analytical solution for the shape of these profiles relating the plastic wave speed to the characteristic variable Z/t.

$$u_w(E_{zz}) = Z/t$$
(54)

and the maximum Lagrangian strain to this same speed:

$$v_0 = -\int_{E_{zz}^{max}}^{0} u_w(E_{zz}) dE_{zz}.$$
(55)

Equation 54 states that every value of plastic strain can propagate at an unique speed; for the flow stress model given by Eqn (51), this speed is given by Eqn (52). Equation (55) relates the wave speed to the velocity of the *undeformed* wire and provides a means for computing the maximum plastic strain realized after the wire has decelerated to zero velocity.

For u_w equal to a constant, as is the case for Eqn (51), the profiles shown in Fig. 8 should be step functions at wave speeds of 0.181 km/s for the Z/t profiles. The observation that the Fig. 8 profiles are distributed about this speed is a consequence of the dissipation in the continuum code calculation, albeit the results do approach the analytical solution as the plastic wave propagates further down the long wire.

Returning to the Fig. 7 observation that $\dot{H}$ appeared large by 2% relative to u_w, this can be understood by noting from Fig. 8 that the numerical propagation speed for a strain close to
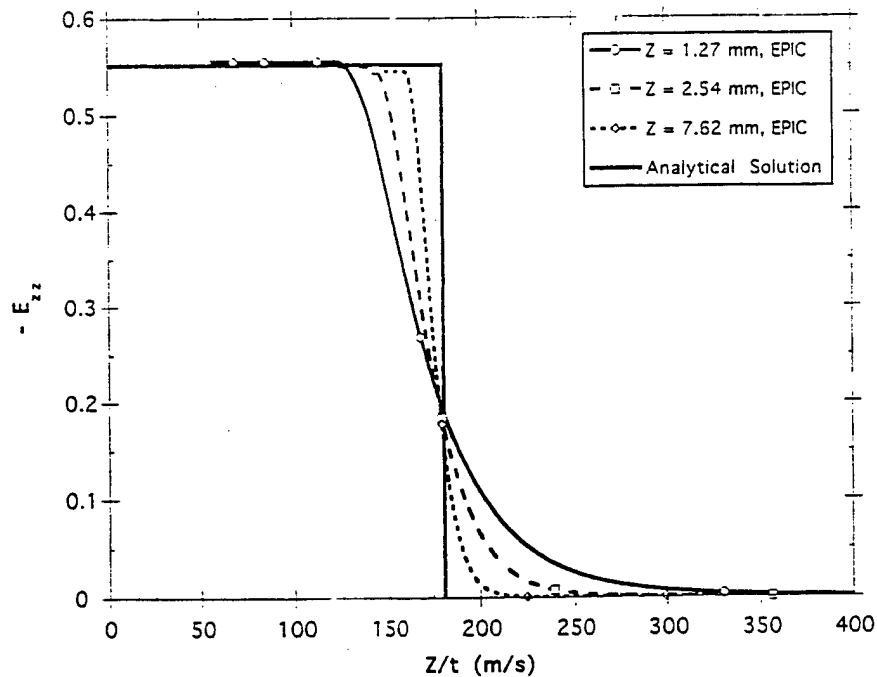
Fig. 8. Wire problem plastic wave profiles at various Lagrangian positions (Z) along the wire measured relative to the impact interface. Wave profiles are in terms of axial Lagrangian strain shown as a function of the characteristic variable Z/t. This calculation incorporates the Mie–Grunisen EOS and a simple strain-hardening flow stress model for an annealed copper. Initial impact velocity is 100 m/s. Also shown is the analytical profile from von Karman [7] and Kolsky [8].

5% is 0.225 km/s at $Z = 1.27$ mm, slowing to 0.190 km/s at 7.62 mm, and approaching 0.181 km/s only in the limit as Z becomes large. Therefore, even though the slopes in Fig. 7 appear to be constant, some transient behavior is still evident in the code calculations from Fig. 8 with the effect of producing slightly faster wave speeds ($\dot{H}$), faster particle velocities (u_1), and also higher stresses (σ_1); recall that the constitutive wave speeds (u_w) given by Eqn (43) and (44) and the jump relationships given by Eqns (17) assume steady state wave propagation.

Equation (55) can be solved for E_{zz}^{max} using u_w from Eqn (52), thus giving the relationship

$$E_{zz}^{max} = \frac{v_0}{u_w} \tag{56}$$

that has a value of -55.2% for the wire problem. This analytical result agrees very well with the Fig. 8 maximum strain of -54.5%.

3.2. Realistic constitutive models

Focusing now on constitutive models that are representative of real materials, Fig. 9 presents continuum code results showing the wave position as a function of time for a plastic strain wave of $\varepsilon_{zz}^p = -4.94\%$ propagating in annealed copper ($\sigma_0 = 86$ MPa) with a constitutive description given by the MTS model. This wave is seen to travel about $z = 8.5$ mm (or $Z = 10.3$ mm) in 20 μs with a constant speed h of 0.406 km/s (or $\dot{H}$ of 0.503 km/s). Figure 9 presents similar wave position results using a constitutive description given by the Johnson–Cook model. Here the wave is seen to travel about $z = 5.1$ mm (or $Z = 6.9$ mm) in 20 μs with a speed h of 0.248 km/s (or $\dot{H}$ of 0.337 km/s). Comparison of the Fig. 9 curves indicates very different plastic wave propagation for the annealed material using the two different flow stress models, the MTS results representing a much faster wave propagation.

Figure 10 is similar to Fig. 9 except that the initial material condition is now hardened ($\sigma_0 = 293$ MPa). Again the MTS result shows faster wave propagation relative to the Johnson–Cook results, albeit a much slower result when compared to the annealed material of Fig. 9.
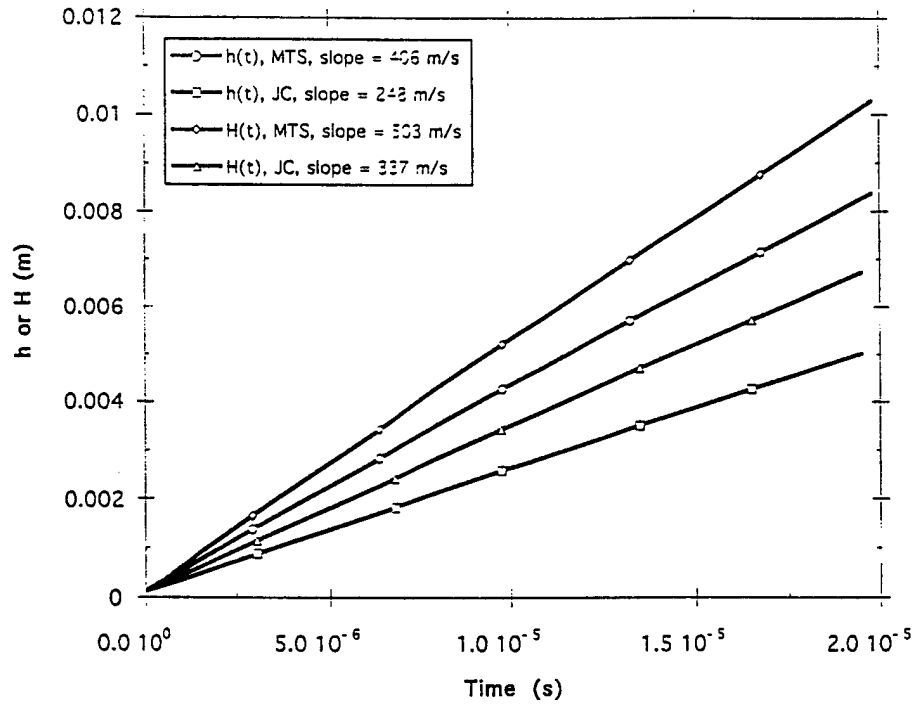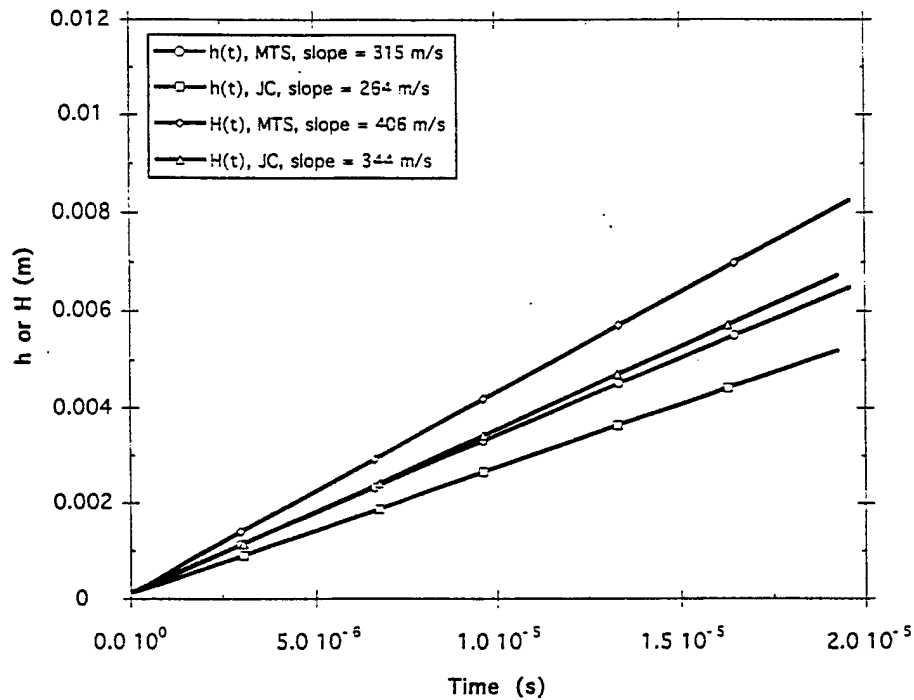
Fig. 9. Wire problem plastic wave position curves using both Eulerian and Lagrangian position coordinates shown as a function of time. These calculations incorporate the Mie–Grunisen EOS and the Johnson–Cook and MTS flow stress models for an annealed copper. Initial impact velocity is 100 m/s.

Fig. 10. Wire problem plastic wave position curves using both Eulerian and Lagrangian position coordinates shown as a function of time. These calculations incorporate the Mie–Grunisen EOS and the Johnson–Cook and MTS flow stress models for a hardened copper. Initial impact velocity is 100 m/s.

Table 4. Plastic strain wave speeds for copper

Material condition. constitutive model	h (km/s)	$v_0 - u_e$ (km/s)	H (km/s)	Wave speed u_w (km/s)
Annealed, constant u_w	0.088	−0.097	0.185	0.181
Hardened, constant u_w	0.094	−0.091	0.185	0.181
Annealed, MTS	0.406	−0.097	0.503	0.507
Hardened, MTS	0.315	−0.091	0.406	0.407
Annealed, JC	0.248	−0.097	0.337	0.321
Hardened, JC	0.264	−0.091	0.344	0.321

Table 4 summarizes Figs 9 and 10 wave speeds comparing different constitutive models and material conditions. Both an annealed and a hardened copper are shown. The simple case where the constitutive model is given by Eqn (51) was discussed above and is given here only for comparison. Both the MTS annealed and hardened copper cases show good agreement when comparing H and u_w. Also, h and H differ almost exactly by $v_0 + u_e$, satisfying Eqn (53a).

The wave speed u_w shown in Table 4 for the Johnson–Cook model is identical for both material conditions because the slope of the Johnson–Cook flow stress is independent of the initial yield stress (no implied saturation behavior). Actually, Johnson–Cook parameters characterized for a hardened copper would have a smaller value for the modulus B than that published for the annealed material in Ref. [17]. The Johnson–Cook annealed and hardened copper cases show somewhat less agreement when comparing H and u_w, differing by about 6%. Also the Johnson–Cook speeds h and H do not seem to differ by $v_0 + u_e$, as indicated by Eqn (53a).

3.3. Comparison to jump relationships

The upper portion of Table 5 summarizes the continuum code results in terms of wave speed, particle velocity, stress, and strain-rate at the plastic strain of $e_A = -4.82\%$ for the various material conditions and constitutive models. These code results can then be compared to jump relationship predictions obtained via Eqns (17) and (38) and listed in the lower portion of Table 5. The jump results are computed assuming a strain e_A of -4.82%

Table 5. Comparison of continuum code results with jump relationships using copper for the wire problem

Continuum code using EPIC	Annealed, constant u_w	Hardened, constant u_w	Annealed, MTS Model	Hardened, MTS Model	Annealed, JC Model	Hardened, JC Model
e_A	−4.82%	−4.82%	−4.82%	−4.82%	−4.82%	−4.82%
ε_v	−0.0252%	−0.0744%	−0.0492%	−0.0870%	−0.0603%	−0.120%
u_w(km/s)	0.181	0.181	0.507	0.407	0.321	0.321
H(km/s)	0.185	0.185	0.503	0.406	0.337	0.344
u_1(m/s)	9.36	9.36	25.7	22.0	26.7	31.6
$\sigma_1(=-\sigma)$(MPa)	−104.	−307	−203.	−359.	−249.	−495.
$\dot{e}^p$(1/s)	4.24×10^4	3.04×10^4	3.00×10^4	2.53×10^4	7.20×10^3	6.53×10^3
Jump relationships plus constitutive model	Annealed, constant u_w	Hardened, constant u_w	Annealed, MTS Model	Hardened, MTS Model	Annealed, JC Model	Hardened, JC Model
e_A	−4.82%	−4.82%	−4.82%	−4.82%	−4.82%	−4.82%
ε_v	−0.0252%	−0.0744%	−0.0492%	−0.0870%	−0.0603%	−0.120%
u_w(km/s)	0.204	0.180	0.521	0.391	0.615	0.684
u_1(m/s)	9.83	8.67	25.1	18.9	29.6	33.0
σ_1(MPa)	−104.	−307.	−203.	−359.	−249.	−495.
$\dot{e}^p$(1/s)	—	—	$\sim 4 \times 10^4$	$> 1 \times 10^4$	NI*	NI*

* NI: no intersection.

and a plastic wave speed obtained by solving Eqn (18) for u_w:

$$u_w = \sqrt{\frac{(\sigma_1/(1 + e_A) - \sigma_0)}{e_A \rho_0}}. \tag{57}$$

Recall that under the uniaxial stress assumption the magnitude of the axial stress σ_1 is always equal to the flow stress σ, without any adjustment for two-dimensional area changes. Therefore the stress $\sigma_1/(1 + e_A)$ appearing in Eqn (57) is replaced by $-\sigma$ for the purpose of computing u_w for the wire problem. Recall also from Section 2.3 that the jump relationships plus a constitutive equation result in a system of three equations for six unknowns. Specifying the two variables e_A and σ_1 ($= -\sigma$) and recalling that ε_v can be evaluated using the uniaxial stress assumption via Eqn (49), then allow the speed u_w, the particle velocity u_1, and the strain rate $\dot{\varepsilon}^p$ to be computed. Comparison of the code and jump results in Table 5 shows good agreement in u_w and u_1 for the constant u_w constitutive model and the MTS model and some disagreement for the Johnson–Cook model.

4. A TAYLOR CYLINDER ANALYSIS

4.1. *Comparison to continuum code results*

The EPIC code [22] was used to simulate the Cylinder Impact Test shown in Fig. 1 for the purpose of numerically observing the plastic wave [7,8] motion along the length of the impacting *cylinder*. This problem is purposely quite similar to the wire problem except that a two-dimensional (r, z) axi-symmetric impact geometry is modeled using quadrilateral elements with an aspect ratio close to one. Ten elements were used across the radius of the cylinder to spatially resolve the plastic wave results presented below. The impact surface was modeled as a rigid boundary. The copper cylinder has a 7.62 mm (0.30 caliber) dia, a Length to Diameter ratio (L/D) of 10, and an initial velocity of 0.100 km/s. The MTS flow stress model is assumed for the mechanical response of the copper, and the Mie–Grunisen EOS is assumed for the nonlinear elastic thermodynamic response.

Plastic wave position curves $H(t)$ and $h(t)$ are presented in Fig. 11 for the annealed copper cylinder impact. The first 10–12 μs of these results show a nonlinear transient (designated as Phase I in Ref. [23]) dominated by the EOS and is the result of the radial relief waves interacting with the lower frequency longitudinal waves [6]; the elastic part of these waves initially propagates at the dilatational speed in an extended medium [8]:

$$c_d = \sqrt{\frac{1}{\rho}\left(k + \frac{4}{3}G\right)}, \tag{58}$$

where k and G are the bulk and shear moduli, respectively, evaluated for the compressed material state. This wave speed is about 4.74 km/s for copper compressed to 3.85 GPa and agrees with the longitudinal sound speed reported by Marsh [24].

After Phase I (i.e. after roughly 12 μs) the kinematics of the plastic wave shown in Fig. 11 transition to a more steady behavior (designated as Phase II in Ref. [23]) similar to wire problem results shown in Fig. 9. The so-called gap closure transient discussed in Ref. [6] determines the time of this Phase I to Phase II transition where the slope of $h(t)$ becomes constant. During this transition the elastic wave speed decelerates from the dilatational speed c_d to that for uniaxial stress realized in the wire problem (i.e. $\sqrt{E/\rho_0}$ or 3.66 km/s), and the plastic wave propagates with a near constant speed corresponding to the constant slope observed in the Fig. 11 results after about 12 μs.

Davies and Hunter [25] and Follansbee [26] review a simple analysis for stress equilibrium concluding that a material region of dimension L requires π wave reverberations with its boundaries before a uniform stress state is achieved; in terms of an equilibration time T_e they advocate

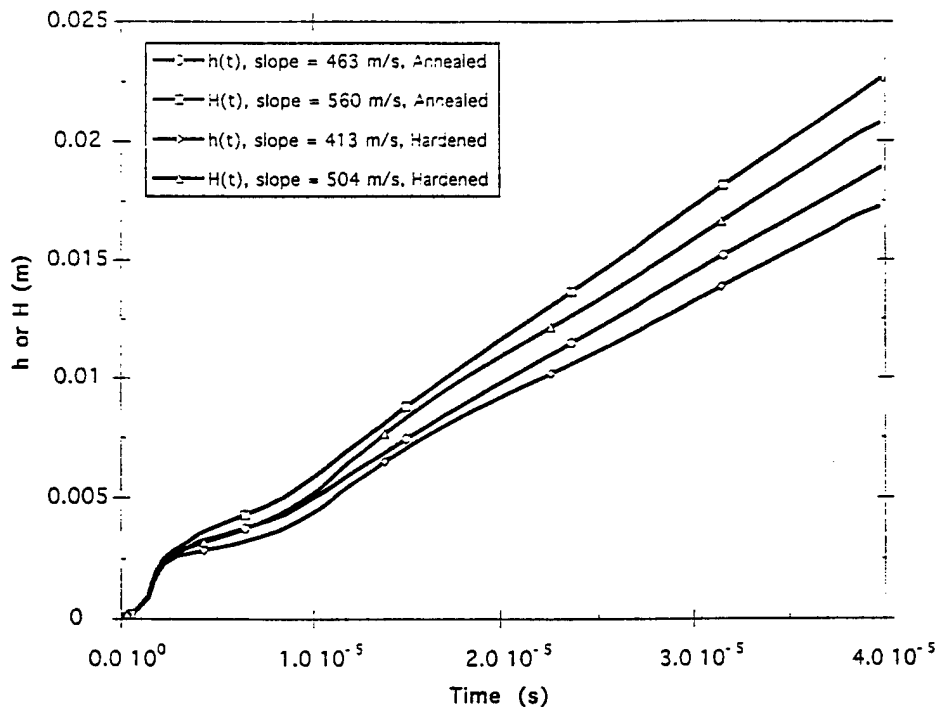$$T_e = \frac{\pi L}{u_w}. \tag{59}$$

Fig. 11. Taylor Cylinder problem plastic wave position curves using both Eulerian and Lagrangian position coordinates shown as a function of time. These calculations incorporate the Mie–Grunisen EOS and the MTS flow stress model for both annealed and hardened coppers. Initial impact velocity is 100 m/s. Note that the position curves show an initial transient behavior [23] out to about 12 μs.

For an elastic problem the wave speed u_w would be constructed from the appropriate elastic moduli, but for a plasticity problem with strain hardening (where the stress magnitude is a function of the plastic strain) the appropriate value for u_w in Eqn (59) would be the plastic wave speed. If we let the dimension L be the radius R of the impacting 7.62 mm cylinder and u_w be equal to a plastic wave speed of 0.507 km/s, then T_e has a value of 23.6 μs. Thus plastic strain disturbances realized during the transition from Phase I to Phase II should require about 24 μs to attain radial stress uniformity, or about 36 μs total (12 μs for Phase I plus 24 μs). Figure 12 supports this rationale showing stress histories for the cylinder impact problem realized at the centerline at the axial location of the plastic wave. The early time (Phase I) stress history has been discussed in some detail in Ref. [6]. It can be observed in this figure that the total axial stress and pressure do not achieve steady state until after at least 36 μs. However in terms of $H(t)$ or $h(t)$ results, i.e. Fig. 11, steady plastic wave propagation is realized quite early in the event, after 12 μs.

Further observation of Fig. 12 indicates that even though the stress state may be approaching a constant after 36 μs, a state of uniaxial stress has not yet been realized since the axial stress exceeds the flow stress by roughly 10% [see Eqn (42a)]. Again Davies and Hunter [25] and Follansbee [26] conclude that stress waves require upwards of 20–40 dia of travel before uniaxial stress is realized for a cylinder impact similar to a Taylor Test; for a 7.62 mm cylinder this means 152–304 mm of stress wave travel, or 41.6–83.2 μs. Figure 12 indicates that 80 μs is not quite sufficient to realize uniaxial stress in the Taylor Test simulation. Therefore, use of the uniaxial stress plastic wave relationship given by Eqn (32) *at early times* should therefore be corrected for inertial effects.

Returning now to the Fig. 11 results. the slope of the $H(t)$ curve after 12 μs might be expected to correspond to the Table 4 u_w of 0.507 km/s for annealed MTS copper. However, measurement of $\dot{H}$ for 12 μs $\leqslant t \leqslant$ 50 μs gives a faster propagation of about 0.560 km/s. In fact $\dot{H}$ does not decay to smaller values even at late times, say 40–50 μs. The difference observed in these results [i.e. u_w for the wire problem given by Eqn (32) versus u_w for the finite cylinder
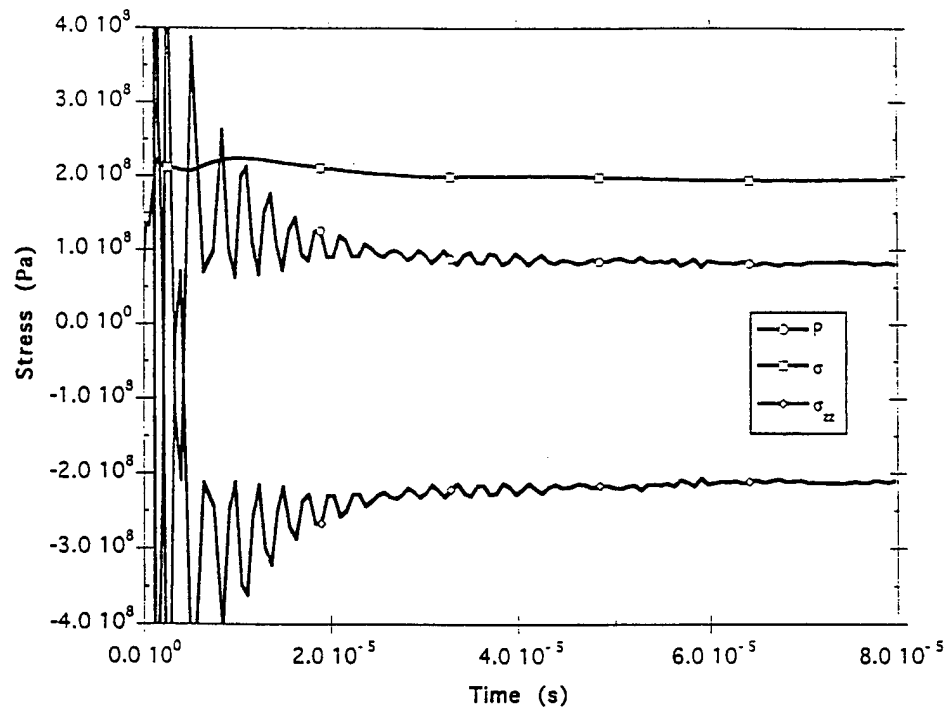
Fig. 12. Taylor problem stress histories from the centerline of an impacting cylinder at the axial location of the plastic wave position. These calculations incorporate the Mie–Grunisen EOS and the MTS flow stress model for annealed copper. Initial impact velocity is 100 m/s. Observed oscillations represent radial wave dispersion demonstrating that stress equilibrium is not achieved until after $40\,\mu s$.

problem given by Eqn (57) is due in part to the two-dimensional aspect of area change that is explicitly accounted for in Eqn (57) by the $(1 + e_A)$ factor modifying the stress σ_1. This statement is supported by reviewing Fig. 12 where σ_{zz} is not equal to $-\sigma$, which is the criterion for uniaxial stress; at early times $(20\,\mu s)$ in Fig. 12 the flow stress is about 199 MPa versus an axial stress value of -240 MPa. Note from Eqn (18) that the axial stress is proportional to the square of plastic wave speed, thus the faster speed observed in Fig. 11 is consistent with the larger stress magnitude observed in Fig. 12.

Table 6 summarizes the comparison of the continuum results for the 0.100 km/s cylinder impact with the jump relationship predictions; both annealed and hardened material results

Table 6. Comparison of continuum code results with jump relationships using copper for the Taylor impact problem (100 m/s)

Continuum code using EPIC	Annealed, MTS Model	Hardened, MTS Model
e_A	-4.82%	-4.82%
ε_v	-0.0509%	-0.0897%
u_w(km/s), Eqn (32)	0.502	0.434
$\dot{H}$ (km/s)	0.560	0.503
u_1(m/s)	26.9	25.9
$\sigma_1(\sigma)$(MPa)	$-240.(210.)$	$-400.(370.)$
$\dot{\varepsilon}^p$(1/s)	1.07×10^4	9.00×10^3
Jump relationships plus constitutive model	Annealed, MTS Model	Hardened, MTS Model
e_A	-4.82%	-4.82%
ε_v	-0.0509%	-0.0897%
u_w(km/s), Eqn (57)	0.573	0.550
u_1(m/s)	27.9	26.5
σ_1(MPa), Eqn (38)	$-225.$	$-403.$
$\dot{\varepsilon}^p$(1/s)	$5. \times 10^5$	$1. \times 10^5$

are presented using the MTS model. Note the code results show 10% higher speeds when compared to u_w calculated via Eqn (32), and that the axial stress σ_1 is also larger than the flow stress σ by 10–20%. One can speculate that areal and radial inertial effects account for most of the difference and conclude that the uniaxial stress assumption is valid to within 20%. The jump predictions presented at the bottom of Table 6 are better suited for comparison to the continuum code results because they do account for the areal change experienced by the cylinder at the position of the 4.82% plastic strain wave. In general, the jump values for u_w, u_1, σ_1 all agree to within 5% with the code results for $\dot{H}$, u_1, σ_1, except for the hardened material wave speeds which exhibit more deviation. The procedure for evaluating the jump relationships first computes σ_1 via Eqn (38) assuming that σ is given, then u_w is computed using Eqn (57) [i.e. Eqn (18) inverted], and finally u_1 is obtained using Eqn (17a). These Table 6 jump predictions are all consistent with a graphical solution using Figs 3 and 4 at the 4.82% plastic strain level; the strain-rates appearing at the bottom of Table 6 were inferred from the graphical solution and are observed to deviate substantially from the continuum code estimates.

As to the question of the influence of numerical parameters such as artificial viscosity Q, a Courant condition [27] determined time step Δt, and initial finite element size Δz on the continuum code results shown in Tables 4–6, Table 7 presents sensitivity coefficients indicating the how these parameters affect the plastic wave speed $\dot{H}$. Table 7 shows small sensitivity to EPIC numerical parameters, the largest being Δz, which decreases $\dot{H}$ by 3.06% if the mesh size were doubled.

Plastic wave profiles similar to the wire problem profiles in Fig. 8 in terms of the axial plastic strain (E_{zz}) versus the Z/t for five elements of material on the cylinder centerline are shown in Fig. 13. As for the Fig. 8 results, all element positions are measured relative to the impact interface in terms of the Lagrangian position variable Z. The plastic strain profiles at low strain for most of these elements are somewhat ragged as a result of radial ringing [6]. Note that the profile shapes during Phase I (profiles $Z = 0$ and $Z = 3.74$ mm) are unique, but after the Phase I to Phase II transition the profile shapes (profiles $Z = 7.47$, 11.21 and 14.91 mm) all collapse onto each other and indicate a common plastic wave speed of about 0.550 km/s at the 5% strain level.

4.2. Comparison to experimental data

Several Taylor Anvil tests conducted by Wilson et al. [5] at Eglin Air Force Base were simulated. These tests feature copper cylinders having a 7.62 mm (7.62 mm) dia, a Length to Diameter ratio (L/D) of 7.5, and various initial velocities. In order to compare the calculations with the Eglin AFB test data in terms of plastic wave propagation speeds, two criteria were used: (1) the radial bulge criterion [i.e. $(R - R_0)/R_0$, R being the peripheral radius] used previously at Eglin [see Ref. 5] and (2) the axial plastic strain criterion used in Section 3 (i.e. ε_{zz}^p) applied at the centerline of the cylinder. The plastic strain criterion should define a wave position out in front of the $(R - R_0)/R_0$ position if radial inertia effects are present. A value for $(R - R_0)/R_0$ of 2.5% (i.e. $R - R_0$ equals 3.75/1000 in. for a 7.62 mm rod) is used here reflecting the resolution of the experimental optics [5]. Figure 14 presents the plastic wave position $H(t)$ shown as a function of time from 0 to 25 μs, comparing calculations with experimental data. The calculations use the MTS flow stress model for a hardened copper ($\sigma_0 = 293$ MPa). Note that at small times the calculated radial bulge curve accelerates

Table 7. Sensitivity of the wave speed to numerical parameters

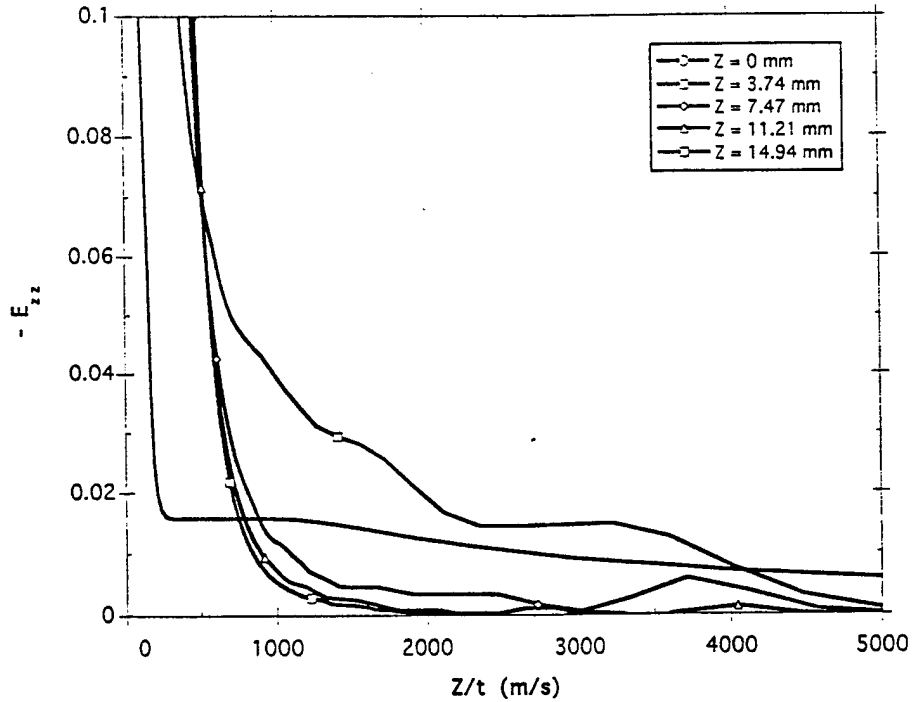| Parameter x	$\dfrac{\Delta \dot{H}/\dot{H}}{\Delta x/x}$
Time step, Δt	-9.33×10^{-3}
Element size, Δz	-3.06×10^{-2}
Artificial viscosity, Q	-9.88×10^{-4}

Fig. 13. Taylor problem plastic wave profiles at various Lagrangian positions (Z) along the cylinder measured relative to the impact interface. Wave profiles are in terms of axial Lagrangian strain shown as a function of the characteristic variable Z/t. This calculation incorporates the Mie–Grunisen EOS and MTS flow stress model for annealed copper. Initial impact velocity is 100 m/s. Note the coalescence of wave profiles after steady wave propagation is achieved (i.e. Phase II wave propagation).
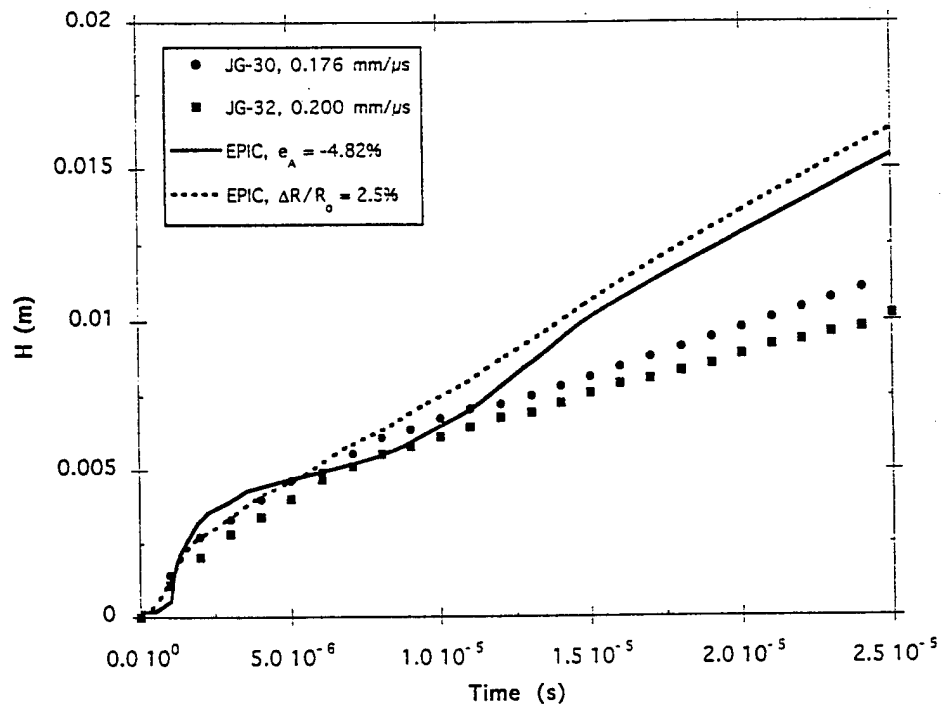

Fig. 14. Taylor problem plastic wave position curves using Lagrangian position coordinates shown as a function of time. These calculations incorporate the Mie–Grunisen EOS and the MTS flow stress model for hardened coppers and are compared to experimental data. Note that the position curves show an initial transient behavior [23] out to about 15 μs.

differently when compared to the calculated plastic strain curve, but the two assume the same asymptotic slope (i.e. same speed, zero acceleration) after about 14 μs: the so-called Phase I to Phase II transition time discussed in Ref. [13].

Also shown in Fig. 14 are the experimental data points from the Eglin AFB tests JG-30 and JG-32 [5, 13]. These two tests are, in principle, identical except for the initial velocity, 0.176 and 0.200 km/s, respectively. Note that the higher velocity JG-32 data points should lie above the JG-30 data; the fact that the reverse is true (higher initial velocity results in higher strain rates, and higher strain rates result in faster wave speeds, see Fig. 2) is probably a measure of the uncertainty in the experimental data sets. The asymptotic slope indicated by the JG-30 data is 43% less than the calculated curves (0.311 km/s for the tests compared to 0.547 km/s for the calculations), and a similar statement can be made for JG-32; the MTS results in Fig. 14 have the appearance of being too stiff.

Table 8 compares mainly wave speeds from the experiments and MTS continuum calculations for the four Eglin AFB tests JG-30, JG-32, JG-34, and JG-38 [5, 13]. As mentioned above, tests JG-30 and JG-32 use the hardened copper and tests JG-34 and JG-38 use annealed copper. The wave speed u_w shown in the fifth column is predicted with the jump relationships using the procedure: (1) given the flow stress at the position of the 4.82% plastic strain wave (as computed by the continuum calculation), calculate the axial stress σ_1 using the energy jump given by Eqn (38) and (2) the wave speed u_w is computed using Eqn (57). This procedure is identical to that described in Section 4.1 for the Table 6 results, and produces speeds that compare well with $\dot{H}$ inferred from the calculations; only 2–4% differences are observed, with the jump u_w being always slightly higher.

Again viewing Table 8, the experimentally measured values of $\dot{H}$ are consistently slower by as much as 50% when compared to either the jump or the continuum code speeds. In fact a quick sensitivity study illustrates that this difference cannot be reconciled with a moderate modification to the constitutive modeling: as indicated by Eqn (34) the MTS wave speed is determined by the three functions s_{th}, Θ_0, and $\hat{\sigma}_s$. We will say that the constant-structure thermal-activation function s_{th} and the saturation threshold stress $\hat{\sigma}_s$ are both physically based and well characterized. As a sensitivity study then, we will treat the dislocation generation rate function Θ_0 as an empirical function that is not well characterized and say it can be modified. Reducing Θ_0 by 50% and repeating the continuum calculations for the same four tests slow the plastic wave speed $\dot{H}$ by about 20% as shown in Table 8, cutting the experimental and calculational difference to about 30%. So, although Θ_0 may be empirical in form and have experimental uncertainty in its parameters, it cannot be in error by the amount needed to bring the calculations into agreement with the tests.

Now the experimental speeds can be further analysed by assuming they are correct and reversing the jump computation procedure outlined above to infer a flow stress at the 4.82% plastic strain wave. Inverting Eqn (57) for σ_1 and Eqn (38) for σ, and using the experimental

Table 8. Laboratory frame plastic strain wave speeds for copper

Cylinder test or Calculation	$\dot{h}$ (km/s)	$r_0 \div u_e$ (km/s)	$\dot{H}$ (km/s)	u_w Eqn (57) (km/s)	σ@ Wave (MPa)
JG-30, 0.176 km/s	0.144	−0.167	0.311	—	289
MTS-hardened	0.379	−0.167	0.547	0.563	375
Modified MTS-h,	0.275	−0.167	0.442	452.0	331
JG-32, 0.200 km/s	0.104	−0.191	0.295	—	285
MTS-hardened	0.361	−0.191	0.552	0.572	379
Modified MTS-h	0.261	−0.191	0.452	0.455	332
JG-38, 0.227 km/s	0.151	−0.224	0.375	—	129
MTS-annealed	0.417	−0.224	0.641	0.653	240
Modified MTS-a	0.293	−0.224	0.516	0.522	180.
JG-34, 0.204 km/s	0.156	−0.201	0.357	—	124
MTS-annealed	0.431	−0.201	0.633	0.645	236
Modified MTS-a	0.308	−0.201	0.508	0.506	174

$\dot{H}$ as the wave speed give the flow stresses listed for the four tests in Table 8. Note that these flow stresses show no work-hardening for the initially hardened copper ($\sigma_0 = 293$ MPa) and only a slight amount of work-hardening for the initially annealed copper ($\sigma_0 = 86$ MPa). Actually the initially hardened copper result shows a slight amount of strain softening.

5. SUMMARIZING REMARKS AND CONCLUSIONS

In summary, the significant parts of this effort are as follows:

(1) The definition of areal strain e_A used by others in the analysis of Taylor Cylinder Impact events [5, 6, 12, 13, 23] was related to the plastic logarithmic strain ε^p_{zz} in Section 2.1. Logarithmic or natural strain is in common use in explicit continuum mechanics codes and is used in this work to track numerically determined plastic strain waves. The areal strain e_A can also be shown to be identical to the definition of small Lagrangian strain E_{zz} in the axial direction.

(2) Conservation jump relationships for mass, momentum, and energy formulated for a steady propagating plastic wave were combined with the thermodynamic and mechanical constitutive behavior of a metal in Section 2.3, yielding a set of four equations (i.e. Eqns (17a), (17b), (38), and a flow stress model) containing the seven unknowns $u_w, u_1, e_A, \varepsilon_v, \sigma_1, \sigma, \dot{\varepsilon}^p$. This manipulation of jump equations in conjunction with constitutive relations is analogous to deriving a $P(\rho)$ Hugoniot for the shock wave problem [11]. Hugoniot curves [i.e. $\sigma_1(e_A, \dot{\varepsilon})$] are presented for the Johnson–Cook and MTS flow stress models (mechanical behavior) and a Mie–Grunisen EOS (thermodynamic behavior) plotted as a function of areal strain and strain-rate.

(3) Rate-dependent mechanical constitutive behavior in the forms of the Johnson–Cook and MTS flow stress models was presented and subsequently differentiated with respect to strain to obtain the classical plastic wave speed [7, 8] for the uniaxial stress problem. Numerical evaluation of these mechanically specific wave speeds indicated a strong sensitivity in the Johnson–Cook model to strain (at small values) and a very weak dependence to strain-rate. Conversely, the MTS model showed a linear dependence on strain and moderate sensitivity to strain-rate. Continuum code results for the uniaxial stress (wire) problem compare well to the analytical solutions derived by von Karman and Duwez and Kolsky for wave speed and the maximum realized plastic strain.

(4) Continuum code simulations of Taylor Cylinder events were performed for 0.100 km/s impacts and the results (in particular u_w, u_1, σ_1) were compared to estimates using the specific jump relationships:

$$\sigma_1 = -\frac{\frac{1}{2}e_A\sigma_0 + i_0\rho_0 + \frac{1}{\Gamma}\left(\frac{2}{3}\sigma - \varepsilon_v k_1\right)}{\frac{1}{\Gamma} + \frac{1}{2}\frac{e_A}{(1 + e_A)}} \tag{60}$$

$$u_w = \sqrt{\frac{\sigma_1(1 + e_A) - \sigma_0}{e_A\rho_0}} \tag{61}$$

$$u_1 = -u_w e_A. \tag{62}$$

Evaluation of these relationships assumes that a flow stress model is given and that the areal strain and strain-rate are specified. This comparison (detailed in Table 6) was found to be in good agreement for all quantities compared except for the strain-rate. The lack of agreement for the strain-rate is possibly due to the action of artificial viscosity in the continuum code results. A further assumption is made in the use of Eqns (60)–(62) that the volumetric strain ε_v can be approximated using the uniaxial stress relationship given by Eqn (49); this was found to be a very good approximation when compared to EPIC calculations.

(5) A sensitivity analysis was performed to verify that the continuum code simulations of the Taylor Test are well resolved in space and time and not heavily influenced by artificial

viscosity. The sensitivities showed that the effect of these numerical quantities on wave speeds is less than 3% per 100% change in the space or time resolution or artificial viscosity.

(6) Continuum code simulations of the hardened and annealed copper Taylor Cylinder Tests conducted at Eglin AFB [5] were performed for impact velocities that ranged from 0.176 to 0.228 km/s, and the results (again u_x, u_1, σ_1) were compared to estimates using the jump relationships Eqns (60)–(62) and with the experimental plastic wave speeds extracted from the Eglin AFB time-resolved data (see Table 8). As in item 4 above, the continuum and jump results compare very well, but both indicate much faster wave propagation relative to the experimental wave speeds. It can be speculated that the experimental wave speeds were extracted from the film at a strain level larger than the estimated resolution threshold of the data, or that the flow stress models used in the code calculations do not accurately capture the plastic wave propagation speed. Assuming that the experimental wave speeds are physically correct, the jump relationships can be inverted and used to estimate the flow stress implied by the Table 8 experimental wave speeds. Inverting the jump relationships for this purpose gives

$$\sigma_1 = (1 + e_A)[\sigma_0 + \rho_0 \dot{H}^2 e_A] \tag{63}$$

$$\sigma = -\frac{3}{4} e_A \sigma_0 \Gamma - \frac{3}{2} i_0 \rho_0 \Gamma + \frac{3}{2} \varepsilon_v k_1 - \sigma_1 \left[\frac{3}{2} + \frac{3}{4} \frac{e_A \Gamma}{(1 + e_A)} \right] \tag{64}$$

$$i_1 = i_0 + \frac{e_A}{\rho_0} \frac{1}{2} \left(\frac{\sigma_1}{(1 + e_A)} - \sigma_0 \right) \tag{65}$$

that when applied to the experimental speeds gives a flow stress magnitude for the hardened copper that is close to the initial yield (showing negligible hardening at the 4.82% strain level) and values for the annealed copper that indicate very modest hardening (see Table 8).

(7) Note that Eqns (63)–(65) are in the appropriate form for converting time resolved experimental wave speeds, i.e. $\dot{H}(e_A)$ or $\dot{H}(e_A, \dot{e}^P)$, into mechanical constitutive behavior, i.e. $\sigma(e_A, i_1)$ or $\sigma(e_A, \dot{e}^P, i_1)$, respectively, under the assumption that elastic strains are small.

REFERENCES

1. Taylor, G. I., The use of flat-ended projectiles for determining dynamic yield stress I. Theoretical considerations. *Proceedings of the Royal Society of London.* A-194, 289 (1948).

2. Lee, E. H. and Tupper, S. J., Analysis of plastic deformation in a steel cylinder striking a rigid target. *Journal of Applied Mechanics.* 21, 63 (1954).

3. Hawkyard, J. B., A theory for the mushrooming of flat-ended projectiles impinging on a flat rigid anvil, using energy considerations. *International Journal of Mechanical Sciences*, 11, 313 (1969).

4. Erlich, D. C., Shockley, D. A. and Seaman, L., Symmetric rod impact technique for dynamic yield determination. *AIP Conf. Proc., No. 78, Second Topical Conf. on Shock Waves in Condensed Matter*, Menlo Park, CA, p. 402 (1981).

5. Wilson, L. L., House, J. W. and Nixon, M. E., Time resolved deformation from the cylinder impact test. AFATL-TR-89-76 (November 1989).

6. Jones, S. E., Maudlin, P. J., Gillis, P. P. and Foster, Jr., J. C., An analytical interpretation of high strain rate material behavior during early time plastic deformation in the Taylor impact test. *Computers in Engineering 1992*, ed. G. A. Gabriele 2, 173 *ASME, New York* (1992).

7. von Karman, T. and Duwez, P., The propagation of plastic deformation in solids. *Journal of Applied Physics*, 21, 987 (1950).

8. Kolsky, H., *Stress Waves in Solids*. Dover Publications, New York (1963).

9. Malvern, L. E., The propagation of longitudinal waves of plastic deformation in a bar of material exhibiting a strain-rate effect. *Journal Applied Mechanics*. 18, 203 (1951).

10. Kolsky, H. and Douch, L. S., Experimental studies in plastic wave propagation. *Journal of the Mechanics and Physics of Solids.* 10, 195 (1962).

11. Courant, R. and Friedrichs, K. O., Supersonic flow and shock waves. *Applied Mathematical Sciences*, 21, Springer, New York (1948).

12. Foster, Jr., J. C., Maudlin, P. J. and Jones, S. E., On the Taylor test: a continuum analysis of plastic wave propagation. *Proc. of the 1995 APS Topical Conf. on Shock Compression of Condensed Matter*, Seattle, Washington, p. 291 (1995).

13. Jones, S. E., Maudlin, P. J., Foster, Jr., J. C. and Kazmier, M., On the Taylor test, Part II: an engineering analysis of plastic wave propagation. Los Alamos National Laboratory report LA-12845-MS (1994).

14. Harlow, F. H. and Amsden, A. A., *Fluid Dynamics*. LA-4700, Los Alamos Scientific Laboratory (1971).

15. von Mises, R., Mechanik der plastischen Formanderung von Kristallen. *Z. angew. Math. Mech.*, 8, 161–85 (1928).

16. Johnson, G. R. and Cook, W. H., A constitutive model and data for metals subjected to large strains, high strain rates, and high temperatures. *Proceeding of the 7th International Symposium on Ballistics*, The Hague, The Netherlands (April 1983).

17. Johnson, G. R. and Holmquist, T. J., Test data and computational strength and fracture model constants for 23 materials subjected to large strains, high strain rates, and high temperatures, LA-11463-MS, Los Alamos National Laboratory (1989).

18. Follansbee, P. S., High-strain-rate deformation of FCC metals and alloys. In *Metallurgical Applications of Shock-Wave and High-Strain-Rate Phenomena*, eds. L. E. Murr, K. P. Staudhammer and M. A. Meyers, Chap. 24, p. 451, Marcell Dekker, New York (1986).

19. Follansbee, P. S. and Kocks, U. F., A constitutive description of the deformation of copper based on the use of mechanical threshold stress as an internal state variable. *Acta Metallica*, 36, 81–93 (1988).

20. Malvern, L. E., *Introduction to the Mechanics of a Continuous Medium*. Prentice-Hall, New Jersey (1969).

21. Maudlin, P. J., Davidson, R. F. and Henninger, R. J., Implementation and assessment of the mechanical-threshold-stress model using the EPIC2 and PINON computer codes. Los Alamos National Laboratory, LA-11895-MS (September 1990).

22. Johnson, G. R. and Stryk, R. A., User instructions for the EPIC-2 Code. Air Force Armament Laboratory, Eglin Air Force Base report AFATL-TR-86-51 (August 1986).

23. Jones, S. E., Gillis, P. P., Foster, Jr, J. C. and Wilson, L. L., A one-dimensional, two-phase flow model for Taylor impact specimens. *Journal Engr. Mats. Technol.* 113, 228 (1991).

24. Marsh, S. P., ed., *LASL Shock Hugoniot Data*. Univ. of California Press, Berkeley, CA (1980).

25. Davies, E. D. H. and Hunter, S. C., The dynamic compression testing of solids by the method of the split Hopkinson pressure bar. *Journal of the Mechanics and Physics of Solids*. 11, 155 (1963).

26. Follansbee, P. S., High strain rate compression testing. *Metals Handbook*. 9th Edition. Vol. 8. ASM, Metalpark, OH (1985).

27. Strikwerda, J. C., *Finite Difference Scheme and Partial Differential Equations*. Wadsworth & Brooks/Cole, California (1989).

APPENDIX F

CONSTITUTIVE MODELING USING THE TAYLOR IMPACT TEST

S.E. Jones
Department of Mechanical Engineering
University of Alabama
Tuscaloosa, Alabama

Paul J. Maudlin
Theoretical Division
Los Alamos National Laboratory
Los Alamos, New Mexico

J.C. Foster, Jr.
Wright Laboratory
Armament Directorate
Eglin Air Force Base, Florida

ABSTRACT

The Taylor test can be conveniently divided into three fairly distinct stages. The first stage is initial transient behavior after impact characterized by nonlinear plastic wave propagation. The second stage is quasi-steady propagation of the plastic wave front. The duration of this stage is a function of the specimen caliber and material. The final stage is terminal transient behavior, during which most of the deceleration of the undeformed section takes place.

After the initial transient is complete, which varies with the strain at which the plastic wave front propagates, the motion is very well behaved, in the sense that a one-dimensional analysis can be effectively applied. This paper contains such an analysis. The results are supported by an example from which the state of stress for an OFHC copper specimen is deduced.

INTRODUCTION

The motion of Taylor impact specimens has been discussed in some detail by the authors [1-3]. In this series of papers, estimates for plastic wave speed, stress, and other key material properties were given. These estimates were developed using two different viewpoints [1,2] and were verified with a continuum calculation [3]. The purpose of this paper is to introduce a new estimate for the maximum strain-rate after the initial transient. This estimate, along with the equation for stress at constant strain [1-3] for the plastic material, allows us to deduce the state of stress at strain-rates exceeding 10^4/sec. A stress/strain-rate diagram at 10% compressive strain for OFHC copper is included as an example at the end of the paper.

The success of the analysis presented in this paper is based on the observation that the particle velocity u of the material at the plastic wave front is proportional to the current speed of the undeformed section v after the initial transient is over. This means that

$$u = \beta v \qquad (1)$$

where β is the constant of proportionality. This hypothesis was first introduced by the authors in [4] without any supporting evidence. Strong supporting evidence for this assumption comes from continuum mechanics code calculations. Figure 1 shows such a calculation for an OFHC copper cylinder, impacting a hardened 4340 steel anvil. The impact velocity is 176 m/s and after the initial transient the relationship between u and v is perfectly linear throughout the period of quasi-steady deformation and the terminal transient. Notice that the slope of the line in Figure 1 corresponds to a value of β approximately 0.85. In [2], this value of corresponds to a strain at the plastic wave front of about 7% in compression.

The notation used in this paper is the same as that used in all of our previous papers, e.g. [4]. For convenience, Figure 2 shows deformed and undeformed specimens. The position of the plastic wave front relative to the fixed anvil face is h. The current undeformed section length is ℓ. The displacement of the back end of the specimen is s, with $\dot{s} = v$. The engineering strain across the plastic wave front is $e = A_0/A - 1$, where A_0 is the original cross-sectional area of the specimen and A is the deformed cross-sectional area.

Conservation of mass (assuming constant density ρ across the plastic wave front) is given by

$$e\dot{\imath} = v - u = (1-\beta)v \ . \qquad (2)$$

The equations of motion for the undeformed section ℓ introduced in [1-2] are:

$$\rho\ell\dot{v} = \sigma_0 \qquad (3)$$
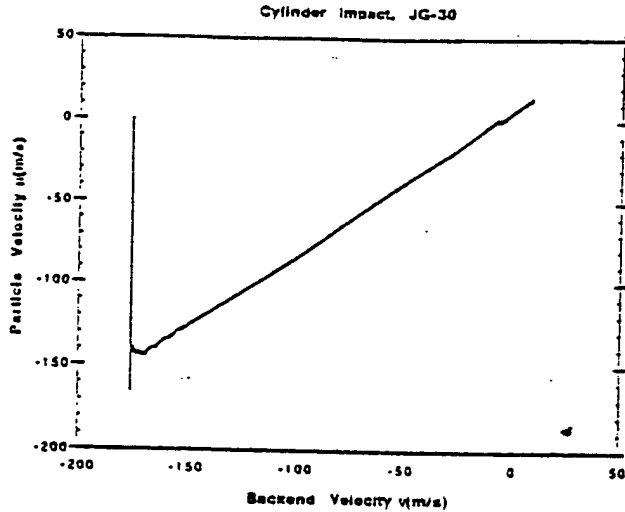
Cylinder Impact, JG-30

FIGURE 1. The relationship between particle velocity at the plastic wave front, u, and undeformed secton velocity, v. Notice that the relationship is completely linear, after a period of initial transient behavior.
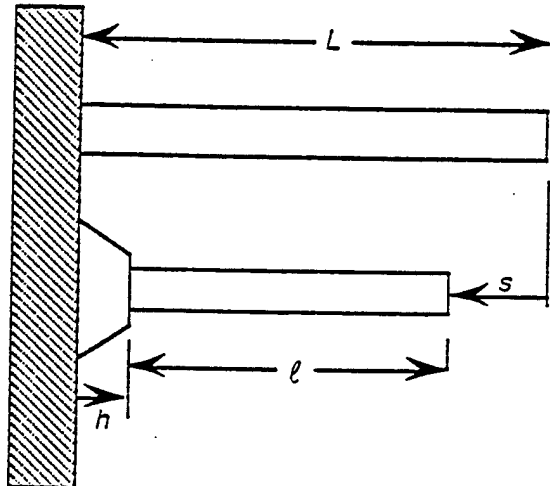

FIGURE 2. A taylor impact specimen of original length L undergoing plastic deformation.

and

$$\rho \dot{\ell}(v-u) = \frac{\sigma}{1+e} - \sigma_0 . \qquad (4)$$

In these equations σ_0 is the quasi-static yield stress in compression for the specimen material and σ is the dynamic compressive yield stress. By using equations (1) and (2), we can write equation (4) in the form

$$\sigma = (1+e)\left(\sigma_0 + \frac{(1-\beta)^2}{e}\rho v^2 \right) . \qquad (5)$$

which expresses the dynamic yield stress in terms of the quasi-static yield stress and the current velocity, a fact which will be useful later.

EVALUATION OF KEY PARAMETERS

The philosophy behind following a plastic wave of constant strain e has been fairly well documented by the authors [1-3]. In [2], it was shown that post-test measurements of recovered Taylor cylinders could be used to determine the key parameters in the test. Two fundamental relationships were devised from kinematic considerations and a detailed examination of the particle velocity during the initial transient [5]. Without further discussion, these relations are:

$$h_f - \bar{h} = -\left(1 + \frac{1-\beta}{e}\right)(s_f - \bar{s}) \qquad (6)$$

and

$$\frac{\bar{h}}{v_0 \bar{t}} = \frac{2\beta - 1}{3e} - \frac{1+2e}{2e} \qquad (7)$$

where $\bar{h}$ is the position of the plastic wave front at the end of the initial transient (see Figure 2). The distance $\bar{s} = v_0 \bar{t}$ is the displacement of the undeformed section at the end of the initial transient. The time $\bar{t}$ will vary for differing strains, as will the distance $\bar{h}$. Figure 3, included here with the permission of the authors [6], shows reduced EPIC code calculations from a Taylor cylinder test on OFHC copper. For low strains, $\bar{h}$ is large while $\bar{t}$ is small. For large strains, $\bar{h}$ is small while $\bar{t}$ is large. The distances h_f and s_f can be measured from a recovered specimen for the strain prescribed. The impact velocity v_0 is known from test instrumentation.

For a prescribed, compressive strain e, equations (6) and (7) are a pair of linear algebraic equations for the determination of β and $\bar{h}$. We assume that the transition time $\bar{t}$ is known. Notice that when $\bar{h}$ has been found, $\bar{t}$ can be determined from

$$\bar{h} + \bar{\ell} + \bar{s} = L \qquad (8)$$
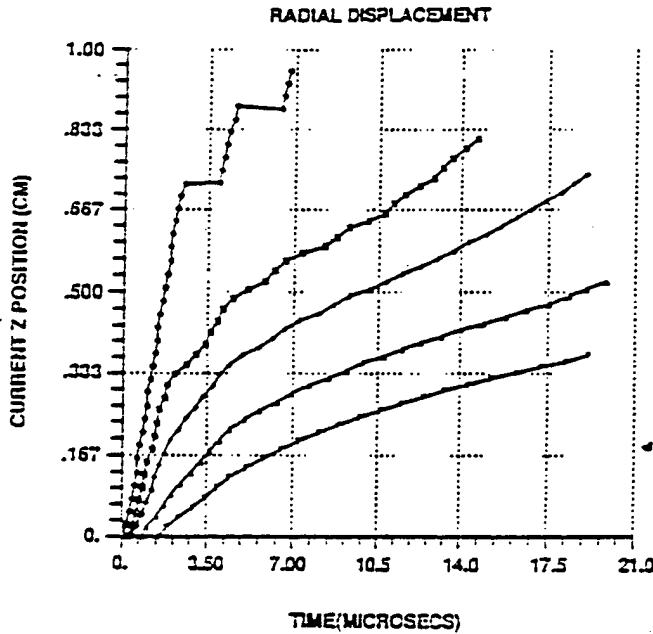
F-2

RADIAL DISPLACEMENT

FIGURE 3. EPIC code calculation showing normalized radial displacement $(R-R_0)/R_0$ versus time (included with the permission of the authors [6]). The normalized displacements correspond to 0.002, 0.010, 0.020, 0.050, and 0.100. The highest curve corresponds to the normalized displacement of 0.002 (0.4% compressive strain) and the largest curve corresponds to the normalized displacement of 0.100 (17.4% compressive strain).

which stems from Figure 2. Also, when β has been found, the plastic wave speed can be determined by

$$\dot{h} = -\left(1 + \frac{1-\beta}{e}\right)v \tag{9}$$

which is the result of combining

$$\dot{h} + \dot{\ell} + v = 0 \tag{10}$$

with equation (2). Reference [2] contains a thorough discussion of these equations and the motivation behind them. A discussion of the post-test measurement technique is also included in this reference.

BEHAVIOR AFTER THE INITIAL TRANSIENT

Equation (3) describes the motion of the undeformed section ℓ during the period of quasi-steady deformation following the initial transient and the terminal transient during which most of the deceleration takes place. Equation (3) can be integrated directly when equation (2) is used to change the variables.

$$\frac{\rho(1-\beta)}{e\sigma_0}vdv = \frac{d\ell}{\ell} \tag{11}$$

Integration of this equation leads to

$$\frac{\rho(1-\beta)}{2e\sigma_0}v^2 = \ell n(\ell) + C_1 \tag{12}$$

The constant of integration C_1 can be evaluated with the conditions at the end of the event. In this case,

$$C_1 = \frac{\rho(1-\beta)}{2e\sigma_0}v_c^2 - \ell n(\ell_f) \tag{13}$$

where ℓ_f is the undeformed section length corresponding to the strain e with which the plastic wave is associated and v_c is the critical velocity of the undeformed section below which deformation at that strain can no longer be sustained. When equations (12) and (13) are combined, we get

$$\ell = \ell_f \, exp\left\{\frac{\rho(1-\beta)}{2e\sigma_0}\left(v^2 - v_c^2\right)\right\} \,. \tag{14}$$

which is the velocity dependent undeformed section length. Notice that the critical velocity v_c can be found from

$$\bar{\ell} = \ell_f \, exp\left\{\frac{\rho(1-\beta)}{2e\sigma_0}\left(v_0^2 - v_c^2\right)\right\} \tag{15}$$

because $\bar{\ell}$ can be determined from equation (8).

Equations (3) and (14) are also the source for information about the displacement of the undeformed section, s. Changing the variables and separating them leads to

$$ds = \frac{\rho\ell_f}{\sigma_0} \, exp\left\{\frac{\rho(1-\beta)}{2e\sigma_0}\left(v^2 - v_c^2\right)\right\}vdv \tag{16}$$

Integration of this equation gives

$$s + C_2 = \frac{e\ell_f}{1-\beta} \, exp\left\{\frac{\rho(1-\beta)}{2e\sigma_0}\left(v^2 - v_c^2\right)\right\} \tag{17}$$

The constant of integration can be evaluated from the conditions that exist at the beginning of quasi-steady, plastic wave propagation [4,5],

$$C_2 = \frac{e\ell_f}{1-\beta} \, exp\left\{\frac{\rho(1-\beta)}{2e\sigma_0}\left(v_0^2 - v_c^2\right)\right\} - \bar{s} \tag{18}$$

and now equation (17) becomes

$$s - \bar{s} = \frac{e\ell_f}{1-\beta}\left[exp\left\{\frac{\rho(1-\beta)}{2e\sigma_0}\left(v^2 - v_c^2\right)\right\} - exp\left\{\frac{\rho(1-\beta)}{2e\sigma_0}\left(v_0^2 - v_c^2\right)\right\}\right] \tag{19}$$

Notice that at the end of the event when $v = v_c$.

$$s_f - \bar{s} = \frac{e \ell_f}{1-\beta}\left[1 - exp\left\{\frac{\rho(1-\beta)}{2e\sigma_0}\left(v_0^2 - v_c^2\right)\right\}\right] . \quad (20)$$

which relates the total displacement during the quasi-steady and terminal transient stages to the change in velocity.

One useful estimate remains to be found. The terminal time can be obtained from equations (3) and (14) by separating the time and velocity.

$$dt = \frac{\rho \ell}{\sigma_0} exp\left\{\frac{\rho(1-\beta)}{2e\sigma_0}\left(v^2 - v_c^2\right)\right\}dv \quad (21)$$

Integrating this equation between the transition time $\bar{t}$ and the current time t allows us to find

$$t = \bar{t} - \frac{\rho \ell_f}{\sigma_0}\int_v^{v_c} exp\left\{\frac{\rho(1-\beta)}{2e\sigma_0}\left(v^2 - v_c^2\right)\right\}dv \quad (22)$$

This equation estimates the current time in terms of the current velocity, v.

ESTIMATION OF STRAIN-RATES

The strain-rate is the most difficult physical quantity to estimate in the test. However, for a complete description of the material it is essential. Taylor [7] and Whiffin [8] discussed the difficulties associated with "rate of strain estimation" in their seminal papers. Their estimates are for average strain-rates with which the average yield stress can be associated. There is no strain connected with these quantities.

Taylor's [7] strain-rate estimate is based on uniform deceleration of the undeformed section. If one assumes that $dv/dt = const.$, then it follows that

$$\frac{1}{2}v^2 = \frac{dv}{dt}s + \frac{1}{2}v_0^2 . \quad (23)$$

At the end of the event, this equation can be used to solve for dv/dt.

$$\frac{dv}{dt} = \frac{-\frac{1}{2}v_0^2}{L - L_f} \quad (24)$$

Separating the variables in this equation and integrating provides us with an estimate for the terminal time, t_f.

$$t_f = \frac{L - L_f}{v_0/2} . \quad (25)$$

at which $v = 0$.

The post-test geometry of a recovered Taylor cylinder is shown in Figure 4. The average engineering strain in the deformed region of the cylinder is given by

$$\frac{\left(L_f - \ell_f\right) - \left(L - \ell_f\right)}{L - \ell_f} = -\frac{L - L_f}{L - \ell_f} . \quad (26)$$

Using the terminal time estimate given in equation (25), an estimate for the average strain-rate can be found.

$$\dot{e}_{Av} = \frac{\left(L_f - \ell_f\right)}{L - \ell_f}\frac{\frac{1}{2}v_0}{L - L_f} = -\frac{\frac{1}{2}v_0}{L - \ell_f} \quad (27)$$

This is Taylor's estimate for the average strain-rate in a Taylor test. Generally, it underestimates the highest rate achieved in the test.

An estimate similar to that of Taylor can be constructed for the present theory. Beginning with equation (23), we modify the result to account for initial transient behavior and find the equivalent of equation (24).

$$\frac{dv}{dt} = -\frac{\frac{1}{2}\left(v_0^2 - v_c^2\right)}{s_f - \bar{s}} \quad (28)$$

Separating the variables in this equation and integrating leads to the time estimate

$$t_f - \bar{t} = \frac{2\left(s_f - \bar{s}\right)}{v_0 + v_c} \quad (29)$$

under these conditions, equation (26) becomes

$$\frac{\left(L_f - \ell_f\right) - \left(\bar{\ell} - \ell_f\right)}{\bar{\ell} - \ell_f} = -\frac{\bar{\ell} - L_f}{\bar{\ell} - \ell_f} \quad (30)$$

Combining equations (29) and (30), we can estimate the average strain-rate for the particular strain in the event.

$$\dot{e}_{Av} = -\frac{\bar{\ell} - L_f}{\bar{\ell} - \ell_f}\frac{v_0 - v_c}{2\left(s_f - \bar{s}\right)} \quad (31)$$

The quantities necessary to make this calculation are all contained in the previous sections. However, the results, like equation (27) are based on uniform deceleration and are typically low.

To improve the strain-rate estimate, we can follow Taylor's reasoning for the current configuration of the specimen. Assuming that the strain behind the plastic wave front is approximately uniform, we can express the average strain-rate as a function of the current position of the rod in the following form.
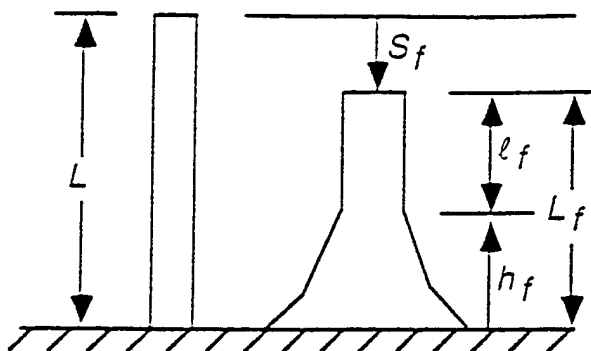
$$\dot{e} = \frac{-s}{L - \ell}\frac{1}{t} \quad (32)$$

FIGURE 4. Deformed and undeformed taylor cylinders. The nomenclature used to describe the deformed cylinder is shown.

TABLE 1

Axial Position (inches)	Rod Diameter (inches)	Axial Position (inches)	Rod Diameter (inches)	Axial Position (inches)	Rod Diameter (inches)
0.000	0.300	0.800	0.308	1.275	0.380
0.050	0.300	0.825	0.310	1.300	0.384
0.100	0.300	0.850	0.313	1.325	0.388
0.150	0.300	0.875	0.318	1.350	0.392
0.200	0.300	0.900	0.321	1.375	0.399
0.250	0.300	0.925	0.324	1.400	0.404
0.300	0.300	0.950	0.327	1.425	0.405
0.350	0.300	0.975	0.333	1.450	0.409
0.400	0.300	1.000	0.337	1.475	0.412
0.450	0.300	1.025	0.342	1.500	0.410
0.500	0.300	1.050	0.346	1.525	0.409
0.550	0.300	1.075	0.350	1.550	0.409
0.600	0.301	1.100	0.353	1.575	0.417
0.650	0.302	1.125	0.358	1.600	0.440
0.675	0.303	1.150	0.361	1.625	0.476
0.700	0.304	1.175	0.365	1.650	0.511
0.725	0.304	1.200	0.369	1.675	0.525
0.750	0.306	1.225	0.372	1.687	0.541
0.775	0.308	1.250	0.376		

An estimate for the maximum rate achieved in the test after the initial transient can now be easily found.

$$\dot{e}_{max} = \frac{-\bar{s}}{L-\bar{\ell}} \; \frac{1}{\bar{t}} = \frac{-v_0}{L-\bar{\ell}} \tag{33}$$

It is tempting to use equations (14), (19), and (22) to estimate the strain-rate as a function of velocity and then draw stress/strain-rate diagrams [8]. However, because equation (32) utilizes uniform strain behind the plastic wave front, it does not predict the rates very well for large times after the initial transient. The assumption is reasonable when the transition from initial transient behavior to quasi-steady deformation occurs (equation (33)), because the deformation zone is thin.

Conclusion

We conclude this paper with an example intended to clarify the very abbreviated presentation in the previous sections. To accomplish this, data from a Taylor test on OFHC copper [6] is presented in Table 1. A 30 caliber rod impacts a hardened 4340 steel anvil at 176 m/s. The axial position is measured from the undeformed (back) end of the specimen and the associated diameter is given at intervals of 0.050". From these measurements, we can approximate the undeformed section lengths for given strains. For example, if e = −0.10, which corresponds to a diameter of 0.316", then we can use linear interpolation to find ℓ_f = 0.867" = 22.0 mm. For this specimen $L = 57.15$ mm and $L_f = 42.91$ mm (See Figure 4). This means that $h_f = 20.89$ mm and $s_f = 14.24$ mm. For this impact, $\bar{t} = 14$ μs is a reasonable choice, and from this estimate $\bar{s} = v_0\bar{t} = 2.46$ mm.

Using the information in the previous paragraph, we can solve equations (6) and (7) for β and $\bar{h}$. The results are: $\beta = 0.768$ and $\bar{h} = 5.40$ mm. It now follows that $\bar{\ell} = L - \bar{h} - \bar{s} = 49.29$ mm.

We are now in a position to estimate the state of stress at 10% compressive strain. Using equation (5) with

$\sigma_0 = -300$ MPa, we find $\sigma = -404$ MPa. From equation (33) we find that this stress corresponds to a strain-rate of -2.24×10^4 s^{-1}. These estimates are all very reasonable and consistent with our earlier efforts [2, 3].

The one-dimensional analysis contained in this paper has been successfully applied to many Taylor specimens. Although only one example has been included, it is clear that data at other strains can be obtained using the same analysis. By varying the impact speed, other strain-rates can be achieved and the stress/strain-rate diagram can be constructed at constant strain. Some of these diagrams will be reported later.

It is possible to develop the constitutive behavior for the specimen material parametrically in terms of the velocity v [9]. Future efforts will concentrate on improving the estimate for velocity dependent strain-rate.

REFERENCES

1. Foster, J.C., Jr., P.J. Maudlin, and S.E. Jones. 1995. "A Continuum Analysis of Plastic Wave Propagation in the Taylor Test." Proceedings of the 1995 APS Topical Conference on Shock Compression of Condensed Matter, Seattle, WA.

2. Jones, S.E., P.J. Maudlin, J.C. Foster, Jr., and M. Kazmeir. 1994. "On the Taylor Test, Part II: An Engineering Analysis of Plastic Wave Propagation." Los Alamos National Laboratory report LA-12845-MS.

3. Maudlin, P.J., J.C. Foster, Jr., and S.E. Jones. 1994. "On the Taylor Test, Part III: A Continuum Mechanics Code Analysis of Steady Plastic Wave Propagation." Los Alamos National Laboratory report LA-12836-MS.

4. Jones, S.E., P.P. Gillis, J.C. Foster, Jr., and L.L. Wilson. 1991. "A One-Dimensional Two-Phase Flow Model for Taylor Impact Specimens." J. Engr. Mat'ls. Tech. Trans. ASME, Vol. 113, p. 228.

5. Jones, S.E., P.J. Maudlin, P.P. Gillis, and J.C. Foster, Jr. 1992. "An Analytical Interpretation of High Strain

Rate Material Behavior During Early Time Plastic Deformation in the Taylor Impact Test." Proceedings of the ASME Computers in Engineering Conference, San Francisco, CA.

6. Wilson, L.L., J.W. House, and M.E. Nixon, 1989, "Time Resolvable Deformation from the Cylinder Impact Test." AFATL-89-76. Air Force Armament Laboratory, Eglin AFB.

7. Taylor, G.I., 1948, "The Use of Flat-Ended Projectiled for Determining Dynamic Yield Stress I Theoretical Considerations." *Proc. Roy. Soc. London.* Series A, Vol. 194, p. 289.

8. Whiffin, A.C., 1948, "The Use of Flat-Ended Projectiles for Determining Dynamic Yield Stress II. Tests on Various Metallic Materials." Vol. 194, p. 300.

9. Jones, S.E., David Allen, Scott Sharp, and Joseph C. Foster, Jr., 1994, "A Parametric Representation for the Constitutive Properties of Metals at High Strain-Rates." Proceedings of the 14th World Congress on Computational and Applied Mathematics, Atlanta, GA. p. 749.

APPENDIX G

A PARAMETRIC REPRESENTATION FOR THE CONSTITUTIVE PROPERTIES OF METALS AT HIGH STRAIN-RATES

by

S. E. Jones, David Allen, Scott Sharp
Department of Engineering Science and Mechanics
The University of Alabama
Tuscaloosa, AL 35487-0278

and

Joseph C. Foster, Jr.
Wright Laboratories
Armament Directorate
Eglin AFB, FL

Introduction

The Taylor impact test is a useful method for determining the flow stress of ductile material at high strain-rates [1,2]. Because the strain-rates achieved in the test can be roughly 10^4 or higher, interest in the Taylor test is growing. Early analyses of the test produced a single estimate for dynamic yield stress at an unknown strain and strain-rate. These estimates indicated the substantial increase in yield stress that can occur at elevated strain-rates, but were not very useful for developing the constitutive properties of the materials. Thus, the emphasis was directed toward using the test to evaluate the material parameters in constitutive equations with hydrocodes and to assess the performance of the codes [3]. However, these results are usually correlated to the particular form of constitutive equation employed. Hence, they are limited by the mathematical structure of this equation and any assumptions used in its development.

One-dimensional models still retain some attractive features. In spite of the fact that they cannot compete with code calculations in terms of accuracy and the number of physical parameters that can be included in a mathematical model, they very often offer a simplicity that lends itself to interpretation that exceeds that provided by the code. It is for this reason that an effort to develop and extend the one-dimensional analysis of the Taylor test continues. In this paper, using the equations governing the terminal transient for the test, implicit stress/strain-rate relations are given at constant strain. The key free parameters in the mathematical model are determined by the theory given in [4]. The results are applied to OFHC copper rods.

The theory presented in [4] focuses on the determination of the key parameters which characterize the deformation of the specimen during quasi-steady motion. However, the specimen undergoes three distinct stages of deformation: (1) an initial transient stage that is dominated by the shock at impact, (2) a period of quasi-steady deformation in which all of the parameters in the problem remain virtually constant, and (3) a terminal transient stage in which deceleration of the undeformed section occurs. The initial transient has been fairly well characterized in [5]. The period of quasi-steady deformation has been extensively discussed in [6,7]. However, the terminal transient behavior of the specimen has not been utilized. In this paper, we demonstrate that this stage can be very successfully applied to the development of constitutive properties for the specimen material.

Theory

The details of the derivation of the equations of motion for the undeformed section are contained in [4]. Without further discussion, these equations are:

$$\rho \ell \dot{v} = \sigma_0 \qquad (1)$$

$$e\dot{\ell} = v - u \qquad (2)$$

$$\dot{h} \div \dot{\ell} + v = 0 \qquad (3)$$

and

$$\sigma = (1 + e)\left(\sigma_0 + \frac{(1 - \beta)^2}{e}\rho v^2\right) \qquad (4)$$

In these equations ρ is the density of the specimen, v is the current velocity of the undeformed section, u is the particle velocity of the plastic material at the plastic wave front, e is the engineering strain at the plastic wave front, β is a parameter relating the particle velocity to the undeformed section velocity, σ_0 is the compressive yield stress of the specimen material, and σ is the compressive dynamic yield stress of the specimen material. Dots over variables denote differentiation with respect to time t.

For terminal transient behavior, we assume that the dynamic yield stress given in equation (4) is valid. We further assume that a reasonable approximation to the plastic wave motion during this stage is provided by $\dot{h} \approx 0$. This doesn't mean that the plastic material has come to rest, but only that the wave front position is stationary in a frame fixed to the rigid boundary surface. With this assumption equation (3) becomes

$$\dot{\ell} = -v \qquad (5)$$

and equation (1) can now be rewritten in the form

$$\rho \ell v \frac{dv}{d\ell} = \sigma_0 \qquad (6)$$

This equation has separable variables and is easily integrated to give

$$\ell = \ell_f \exp\left\{-\frac{\rho}{2\sigma_0}v^2\right\} \qquad (7)$$

which is a relation from which the undeformed section length during the terminal transient can be estimated. ℓ_f is the final undeformed section length which can be determined by the theory presented in [4]. The stress σ_0 is compressive and, therefore, negative.

With equation (7), an estimate for the strain-rate can be found.

$$\dot{e} = \frac{\dot{\ell}}{\ell} = -\frac{1}{\ell_f}v\exp\left\{\frac{\rho}{2\sigma_0}v^2\right\} \qquad (8)$$

Now, the constant strain can be estimated with the engineering analysis given in [4]. The parametric representation of the constitutive equation at constant strain for the specimen material is given by equations (4) and (8).

Conclusions

Equations (4) and (8) can be used to plot the total stress as a function of strain-rate at constant strain. A large base of Taylor test data can be accessed in [8] provided that an estimate for the plastic wave front position at the end of the initial transient can be found. To accomplish this, we observe that the relationship between the kinetic energy of the specimen at impact and the volume of the material in the mushroom is approximately linear. The details of this discussion are contained in [9]. The results of a typical test on OFHC Copper are shown in Figure 2. The strain-rate is somewhat underpredicted because the estimate in equation (8) is crude, especially for longer rods. The effect of reducing the rod length, which decreases ℓ, is shown in Figure 3. For very short rods, the agreement with other observations is substantial. The situation is very similar to that experienced with strain gages in the neighborhood of non-uniform straining. The smaller the gage length, the more accurate the estimate of local strain. The undeformed section length in equation (8) effectively plays the role of a gage length for the specimen. Future efforts will be concentrated on improving the estimate for strain-rate at the plastic wave front.

References

1. G. I. Taylor, "The Use of Flat-Ended Projectiles for Determining Dynamic Yield Stress," *Proc. Roy. Soc. London, Series A.*, Vol. 194, pp. 289-299, September 1948.

2. S. E. Jones, P. P. Gillis, and J. C. Foster, Jr., "On the Equation of Motion of the Undeformed Section of a Taylor Impact Specimen," *J. Appl. Phys.*, Vol. 61, pp. 499-502, January 1987.

3. G. R. Johnson and T. J. Holmquist, "Evaluation of Cyliner-Impact Test Data for Constitutive Model Constants," *J. Appl. Phys.*, Vol. 64, pp. 3901-3910, October 1988.

4. S. E. Jones, J. J. Maudlin, J. C. Foster, Jr., and M. Kazmier, "On the Taylor Test, Part II: An Engineering Analysis of Plastic Wave Propagation," submitted for publication.

5. S. E. Jones, P. J. Maudlin, P. P. Gillis, and J. C. Foster, Jr., "An Analytical Interpretation of High Strain Rate Material Behavior During Early Time Plastic Deformation in the Taylor Impact Test," *Proceedings of the ASME Computers in Engineering Conference*, Vol. 2, pp. 173- 179, August 1992.

6. J. C. Foster, Jr., P. J. Maudlin, and S. E. Jones, "On the Taylor Test, Part I: A Continuum Analysis of Plastic Wave Propagation," submitted for publication.

7. P. J. Maudlin, J. C. Foster, Jr., and S. E. Jones "On the Taylor Test, Part III: A Continuum Mechanics Code Analysis of Plastic Wave Propagation," submitted for publication.

8. J. W. House, "Taylor Impact Testing," AFATL, TR-89- 41.

9. D. J. Allen, "Taylor Impact Testing of Visco-Elastic Materials," Master's Thesis, University of Alabama, May 1995.
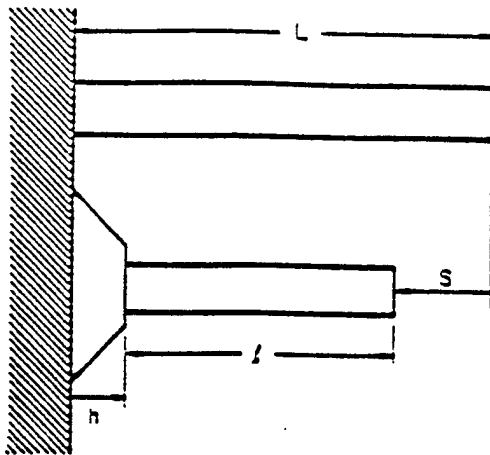
Figure 1. The Taylor impact test. A cylindrical rod of undeformed length L impacts a rigid boundary with velocity v_0. h denotes the current position of the plastic wave front, ℓ denotes the current undeformed section length, and s denotes the displacement of ℓ.
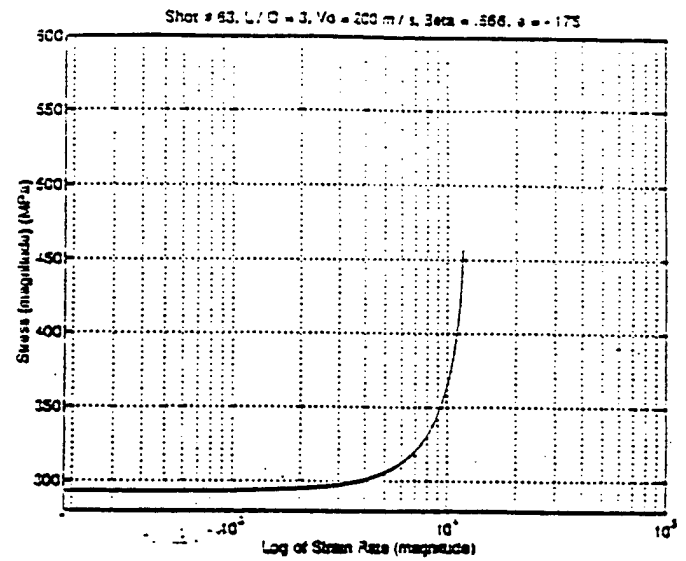

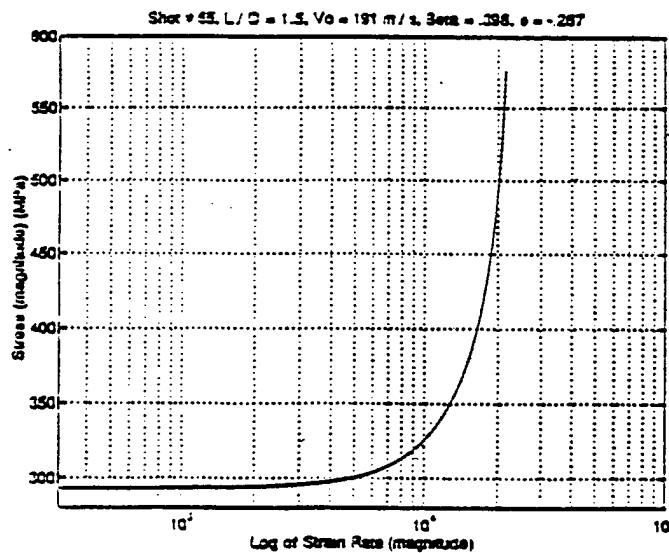Figure 2. A stress/strain-rate diagram at constant strain drawn for OFHC copper with equations (4) and (8).

Figure 3. A stress/strain-rate diagram at constant strain drawn for OFHC copper with equations (4) and (8).
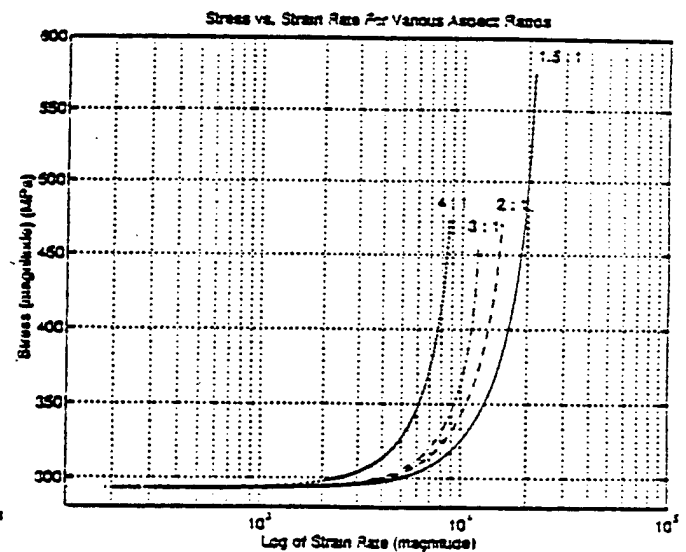
Figure 4. Stress/strain-rate diagrams for OFHC copper. Reducing the undeformed section length during the terminal transient shifts the curve to the right.

APPENDIX H

VOID FORMATION IN OFE COPPER

JESSICA L. MAYES, STEVEN L. HATFIELD and PETER P. GILLIS

Department of Materials Science & Engineering, University of Kentucky
Lexington, Kentucky 40506

JOEL W. HOUSE

Wright Laboratory Armament Directorate - MNMW
Eglin AFB, Florida 32542

ABSTRACT

This paper reports results from the study of dynamic plastic deformation produced in OFE copper specimens by symmetric rod impact (rod-on-rod) tests. The study was performed by post-test sectioning of the specimens and examination of their microstructure using relatively low magnification optical microscopy. Particular emphasis was placed on porosity as a microstructural feature that relates directly to damage theories of constitutive behavior.

INTRODUCTION

Following World War II, Taylor (1947) and Whiffin (1947) published the technique of impacting a cylindrical specimen against a massive anvil and the concomitant elementary analysis that estimates the specimen flow stress from its post-test deformation. Since then, this test has remained a means of primary importance in determining dynamic mechanical properties of ductile materials. As high-speed, large capacity computers came into general use, highly sophisticated numerical analyses were applied to this test. Uncertainties concerning friction, compliance, and impedance, at the specimen-anvil interface eventually led Erlich *et al.,* (1981) to modify this test by impacting a pair of identical rods, one against the other. This form of the test is generally referred to as a symmetric rod impact test or a rod-on-rod (ROR) test, whereas the original rod against anvil experiment is often called a Taylor test. This paper reports results from the study of deformation damage produced in ROR impact testing.

The study was performed by post-test sectioning of the specimens and examination of their microstructures using relatively low magnification optical microscopy. Particular emphasis was placed on porosity, or the lack thereof.

Metallographic analysis of impact specimens subject to high strain rates provides insight into continuum processes, such as plasticity and damage. The objective of this paper is to describe and compare the observed microstructure of Oxygen Free Electronic (OFE) Copper ROR specimens tested at different impact velocities.

EXPERIMENTAL

The material used in these ROR impact tests was OFE copper. However, two different initial grain sizes were used, 75 and 40 μm. Specimens were cut to length from cylindrical rod stock of an initial diameter of 7.94 mm and then turned to a final diameter of 7.62 mm to match the bore of the mann barrel. Material to be tested was annealed at 600°C for one hour in a vacuum and the final average grain size of the specimens tested was 75 and 40 μm, as shown in Fig. 1. The large grain material was impacted at 392 m/s and
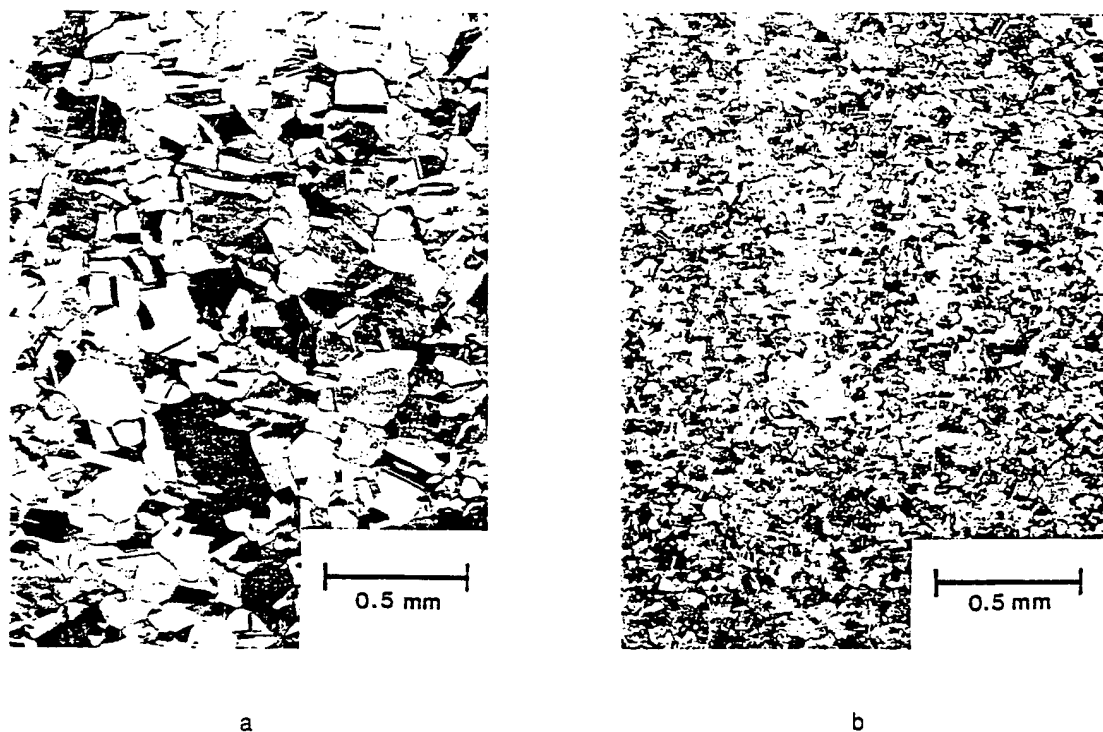
Fig. 1.   Initial microstructure of OFE copper material, a) 75 micron
average grain size, b) 40 micron average grain size.

300 m/s. The fine grain material was impacted at 233 m/s. Complete details of the experimental apparatus, data acquisition techniques, and interpretation are presented elsewhere (House *et al.*, 1992).

Recovered ROR specimens were sectioned along the axis of the rod. Sectioning of the rods was accomplished using a diamond abrasive cutting wheel. After mounting in cold mount epoxy, the specimens were ground and polished using standard methods for preparing copper materials. Final polishing was completed using 0.05 µm alumina abrasive. Dichromate etch was applied to reveal grain structure. The specimens were then viewed under an optical microscope at 50X magnification for microstructural analysis.

RESULTS AND DISCUSSION

Figure 2 is a montage created from photomicrographs originally taken at 50X magnification. The test specimens had been impacted together at 392 m/s. The montage details a midplane of the impactor and receptor rods, from the impact interface back to near the undeformed regions of each. By enlarging this area of interest under the microscope, microstructural features in the plastically deformed region are clearly observed.

As expected, grains near the impact interface and near the specimen axis had collapsed under the large compressive load. The post-impact structure has flat, pancake-shaped grains parallel to the impact face as shown in location a of Fig. 2. Similar deformation is observed to different degrees throughout the mushroomed region. However, it is most severe nearest the impact face and nearest the axis.

Of particular interest, however, are voids observed along the axis near the impact face in both the impactor and receptor, location b. Typically, these cavities are non-symmetric. In order to assess whether the observed porosity resulted from metallographic polishing, the mating surfaces to those shown in Fig. 2 were polished using a different technique. The voids observed in these mating surfaces matched those in the figure. Thus, we believe the observed damage was produced during the impact event.

The void porosity, or damage, results from strong tensile release waves that propagate from the lateral free surface of the rods after the initial compressive wave. These tensile release waves focus on the rod axis

RCR - 2
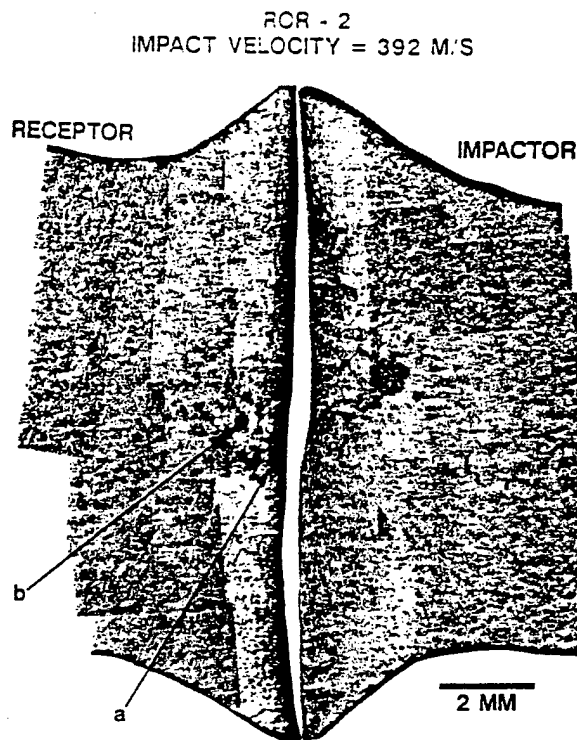IMPACT VELOCITY = 392 M/S

Fig. 2.   Deformed microstructure of 75 μm copper impacted at 392 m/s.

to create a very high, radial tensile stress. This stress causes microvoids to nucleate and grow. Close inspection reveals that the nucleation sites are along grain boundaries with void growth, or link-up, occurring along grain boundaries as well.

Christy *et al.*, (1986) reported on microstructural features of similar OFE copper shock loaded in flyer plate experiments. They reported that in large grain copper, 250 μm and 90 μm material, void nucleation and growth occurred at grain boundaries. The average grain size of the material in Fig. 1a is 75 ±12 μm as determined by the linear intercept method.

Figure 3 shows results from a test conducted at 300 m/s with the 75 μm copper. Comparison between Figs. 2 and 3 shows similar grain deformation has occurred at the impact interface nearest the rod axis. Void nucleation has occurred and appears to be associated with the grain boundaries of the material. In general, Fig. 3 reveals a smaller void size which is consistent with a lower impact velocity. The amplitude of the initial compressive and tensile release waves are impact velocity dependent.

Figure 4 shows results from a test conducted at 233 m/s with the 40 μm copper. Comparison with the 75 μm material shows similar types of grain deformation. However, the void porosity on the rod axis nearest the interface has now increased, and the geometric shape of the voids is spherical. The increased void porosity, for a lower impact velocity experiment, indicates a relationship between the stress state in the material and the grain size.

Christy *et al.*, also experimented with finer grain, 20 μm, copper and with cold worked copper. These materials revealed a change in phenomenology associated with void nucleation and growth. In these materials, Christy *et al.*, observed that the nucleation sites for voids were occurring as often in the matrix

ROR -10
IMPACT VELOCITY = 300 M/S

RECEPTOR   IMPACTOR

2 MM
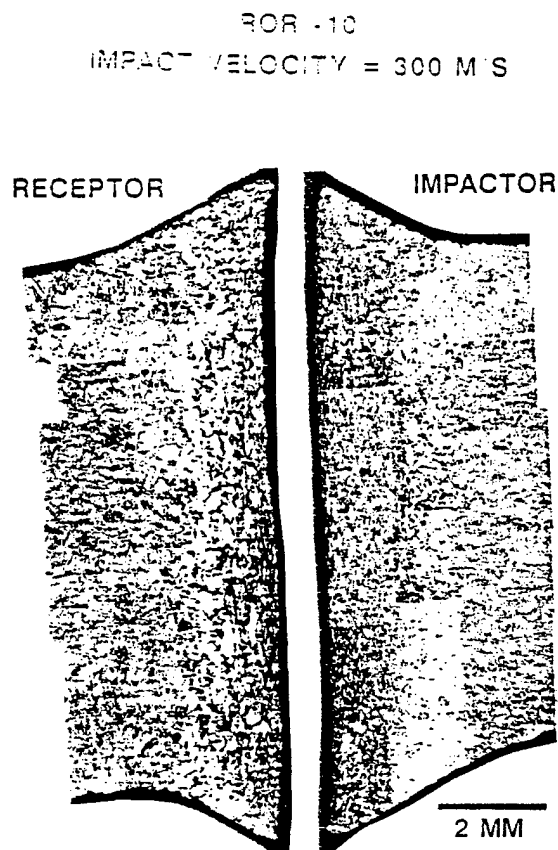
Fig. 3.   Deformed microstructure of 75 μm copper impacted at 300 m/s.

as they did at the grain boundary. Propagation of the voids in fine grain and cold worked copper was occurring by transgranular growth. These observations are consistent with the results seen in Fig. 4.

Grain size studies show that a small grain material will harden faster at low levels of strain than does a larger grain material. This phenomena is related to the grain boundary surface area per unit volume and to the strain compatibility requirements between neighboring grains. Under an applied load, grain boundaries act to create dislocation pile-ups and can be sinks for dislocation annihilation. Because of a high volume fraction of grain boundary, a fine grain material tends to harden rapidly at low strain levels and to have a relatively homogeneous distribution of dislocations.

Copper with a large grain size has a lower volume fraction of grain boundary, it tends to harden more slowly and to have, initially, a more heterogeneous distribution of dislocations. In larger grain material, regions adjacent to grain boundaries have a high dislocation density, whereas in the inner matrix material the dislocation density remains relatively low. Consequently, under the stress state created by tensile release waves, the large grain material hardens along the grain boundaries where eventually the stress state will cause void nucleation to occur. Once nucleated, voids in the material will propagate along the grain boundaries where the energy requirement for crack growth will be lowest.

Under the same stress state, fine grain materials will uniformly harden both at the grain boundary and in the matrix. This condition makes the probability of void nucleation at the grain boundary versus the matrix

One significant difference arises in the quantitative interpretation of porosity between high-speed ROR tests and pseudo-static tension tests. In the latter, the hydrostatic stress is somewhat uniform over any cross-section of the specimen, even after severe necking. Consequently, the area fraction of porosity on any cross-section can be easily calculated and from it the volume fraction (that appears in most theories) can be readily found. By contrast, the stress state in an ROR specimen is much more variable. There are axial and time variations as in the tension specimen, but, unlike the tension specimen, there are large radial variations in stress. In fact, except near transverse free surfaces, the only region of the specimen in which the hydrostatic stress can become tensile is the longitudinal axis. Radial waves from the lateral surface propagate tensile (release) stresses towards the specimen axis. As they converge on the axis, they amplify and produce extremely high hydrostatic tensions in this region even though the axial stress component remains compressive. This description is consistent with the observations of porosity near the specimen axis and complete absence thereof near the lateral surface (Worswick *et al.*, 1991). This leads to the conclusion that there is a radial variation in fractional porosity from center to surface, which raises the question of what total area should be used to calculate an area fraction.

CONCLUSIONS

Microstructural features such as grain deformation and porosity have been examined in specimens recovered from ROR impact tests. These experiments revealed that grain size played a major role in determining the hardening and void growth characteristics of OFE copper. Experiments with 75 μm material at 392 m/s and 300 m/s showed a smaller void size at the lower velocity. An experiment conducted with 40 μm material at 233 m/s showed a striking increase in void porosity and a general change in void geometry. This demonstrates the influence of the grain boundary causing more rapid hardening of the fine grain material than in the larger grain material. The ROR impact test has proven to be a useful experiment for studying high strain-rate deformation when combined with an analysis of internal material damage.

REFERENCES

Christy, S., H. Pak, and M.A. Meyers (1986). In: *Metallurgical Applications of Shock-Wave and High-Strain-Rate Phenomena* (L.E. Murr, K.P. Stauchammmer, M.A. Meyers, eds.), pp. 835-863. Marcel Dekker, Inc., New York.

Erlich, D., D.A. Shockey and L. Seaman (1981). In: *AIP Conference Proceedings, No. 78, Second Topical Conference on Shock Waves in Condensed Matter,* pp. 402-406. Menlo Park, California.

House, J.W., L.L. Wilson, T. Wallace, P. Mauclin (1992). Experimental Results of Symmetric Taylor Tests Using OFE Copper, In preparation.

Taylor, G.I. (1947). The Use of Flat-Ended Projectiles for Determining Dynamic Yield Stress, I. Theoretical Considerations, *Proc. Roy. Soc. London, Series A,* **194,** 289-299.

Whiffin, A.C. (1947). The Use of Flat-Ended Projectiles for Determining Dynamic Yield Stress, II. Tests on Various Metallic Materials, *Proc. Roy. Scc. London, Series A,* **194,** 300-322.

Worswick, M.J., B. Wang and R.J. Pick (1991). Void Growth During High-Velocity Impact: Experiment and Model. *Journal de Physique,* **4,** 605-612.

APPENDIX I

AN ELEMENTARY THEORY OF ONE-DIMENSIONAL ROD PENETRATION USING A NEW ESTIMATE FOR PRESSURE

P. WANG and S. E. JONES

Department of Engineering Science and Mechanics. The University of Alabama, Tuscaloosa, AL 35487, U.S.A.

Summary—In this paper, a new pressure law is proposed to replace the modified Bernoulli equation of Tate in 1967 and 1969. It is achieved by decomposing the equation of motion, which was proposed by Jones *et al.* in 1987, into two parts and incorporating the kinematic equation by Wilson *et al.* in 1989. The new pressure law takes the effect of mushroom strain into account. From two different considerations, the pressure law is applied to the one-dimensional penetration modeling. First, by assuming that the rod/target interface pressure is approximately constant during the quasi-steady state, the governing equations can be analytically integrated to give a closed form solution for the penetration depth. The prediction is reasonably good in the low velocity regime. Secondly, a velocity-dependent interface pressure is added. A so-called shape factor, which was first introduced without physical interpretation by Alekseevskii in 1966. is substantiated. With this factor, the governing equations can be numerically integrated to give very accurate predictions for the impact velocity range from 1 km/s to 4 km/s.

INTRODUCTION

In the model developed by Alekseevskii [1] and Tate [2], the behavior of the rod is assumed to have two consecutive deformation zones. The first zone is a wafer thin plastic region, which is instantaneously eroded at the tip (or rod/target interface) of the rod. The second zone is the current uneroded (rigid) portion of the rod. In the first zone, the rod material is assumed to behave hydrodynamically, and in the second zone the rod is rigid over its uneroded length. The transition between these two zones is assumed to occur somewhere around the maximum stress (ultimate dynamic yield strength) that the rod can sustain as a rigid body. Beyond this dynamic yield strength, the material then behaves more like an incompressible and inviscid fluid in steady state. In order to simulate this transition phenomenon, for the first zone, they introduced the modified Bernoulli equation, which includes both dynamic strengths of the rod and target. This was used to estimate the rod/target interface pressure and to relate the current penetration velocity to the current velocity of the uneroded rod. As to the second zone, they applied Newton's second law to estimate a decelerated motion for the undeformed section. However, a factor that is controversial, but vital to the modified Bernoulli equation, is how to determine the strengths for the rod and target materials. These strength values are frequently obtained by matching the theoretical prediction of penetration depth with experimental data. A variety of attempts to estimate the target strength analytically thus became the focus of many efforts in verifying or revising the theory of Tate and Alekseevskii. Tate [3, 4] developed a flow field model, from which the modified Bernoulli equation was derived and the strength factors were correlated to material constants. Assuming elastic–plastic behavior of the rod and target material, the size of plastic region in the rod was estimated. It was suggested by Tate that a treatment of the unsteady motion could be accommodated by the addition of a Archimedean buoyance terms, which are present in any accelerated frame of reference. From the viewpoint of force balance, Rosenberg *et al.* [5] introduced the effective cross-sectional areas of the rigid rod and its mushroom front end to the modified Bernoulli equation. Based on this modification, and estimating the target resistance from the expansion of a cylindrical cavity in an infinite medium, they claimed good agreement between the model and experimental data. On the other hand, Wright [6,7] and Wright and Frank [8] questioned the validity of the

I-1

assumption of the steady state and the estimate of the interface pressure by the modified Bernoulli equation. Lately. Anderson and Walker [9] have made a further examination of Tate's model with the aid of numerical simulation. They indicated that because a finite region of the projectile deceleration is not accounted for, Tate's model predicts the rear of the projectile decelerates too late and too rapidly at the end of penetration. On the basis of discrepancies in the prediction between Tate's model and numerical simulation, Walker and Anderson [10] proposed a nonsteady state penetration model. Anderson *et al.* [11, 12] also reported that target resistance varies considerably during penetration and that the resistance value used in Tate's model should be considered as an average value to give the correct penetration depth. Recently, Grace [13] proposed a new one-dimensional theory of non-steady penetration of long rods into semi-infinite targets. In his model, the target is modeled as a finite mass that resides within the semi-infinite target and undergoes erosion and deceleration during the penetration process. Based on Newton's law, deriving the equations of motion for the target and the penetrator leads to a new u–v relationship that has replaced the modified Bernoulli equation.

Evidently, there are some deficiencies in the theory of Tate and Alekseevskii in spite of the fact that it has been broadly thought of as a standard reference for one-dimensional long-rod penetration over the past decades. Indicating the fact that this model does not consider mass transfer into the plastic zone and a non-zero mushroom strain at the penetrator tip, Jones *et al.* [14] used the impulse–momentum equation to modify Tate's equation of motion for the undeformed section:

$$l\dot{v} + \dot{l}(v - u) = -\frac{P_B}{\rho(1 + e)} \tag{1}$$

where l is current length of the undeformed penetrator, of which the current velocity is v, and u is the penetration velocity of the penetrator tip. The parameter ρ represents the rod density and e is the mushroom strain, which is assumed constant throughout the quasi-steady state. The term P_B is the penetrator/target interface pressure, estimated by the modified Bernoulli equation. In this equation, the relative velocity term at the left hand side provides the contribution to momentum due to mass transfer into the plastic zone and the strain factor e reflects mushrooming effect at the tip of the penetrator. Compared with Eqn (1), Tate's model has assumed the plastic region is instantaneously consumed, which renders no change in momentum and a 0% compressive strain. Although Eqn (1) can characterize the penetration process in more detail, the pressure term based on the modified Bernoulli equation is ad-hoc. It is apparent that the pressure used by Tate, which in effect causes a 0% compressive strain to the penetrator tip, must be too high for a penetrator with a non-zero mushroom strain. Therefore, Cinnamon *et al.* [15] tried to reduce the net force by introducing a factor to account for the variation of the pressure across the mushroom face. This factor is further correlated to the target strength. With this factor n added, Eqn (1) becomes

$$l\dot{v} + \dot{l}(v - u) = -\frac{P_B}{\rho(1 + n)(1 + e)}. \tag{2}$$

Accompanied with an initial transient analysis and a linear relationship between crater volume and kinetic energy, reasonable predictions can be obtained for impact velocities from 1 km/s to 3 km/s. However, an attempt to integrate the equations analytically and piece together the initial transient and quasi-steady state motions does not succeed due to the presence of a singularity. Consequently, Cinnamon [16] made a further analysis in which the average pressure at quasi-steady state is assumed constant over the range of impact velocities for particular shot combinations. The average pressure is again correlated to the target strength. A similar attempt to integrate these equations analytically by replacing the modified Bernoulli pressure P_B in Eqn (1) with the average pressure also cannot be accomplished due to the presence of a singularity. The reason for this may be the answer for the unsuccessful implementation of modified pressure laws in the model. This suggests that

a reconstruction of the u–v relationship may be necessary in this model, and that a more accurate pressure law may depend on more than densities and strengths.

In this paper, the model proposed by Jones et al. [14] is re-examined. Based on the work of Wang and Jones [17], the original equation of motion will be decomposed into two parts to account for the motions of the mushroom region and the undeformed portion of the penetrator separately. As a result of incorporating these two equations with the kinematic equation derived by Wilson et al. [18], a new pressure law is proposed to replace the modified Bernoulli equation. This new estimate for pressure, taking the effect of mushroom strain in the penetrator tip into account, leads to a new interpretation of the interaction between the pressure and the penetrator during penetration.

Two different cases are considered to implement the pressure law in the model and reasonable agreement with experimental data is achieved with each. In the first case, the pressure is assumed velocity independent (constant) and a new u–v relationship is constructed. Direct integration of this system leads to a closed form solution for the penetration depth. The constant pressures are obtained by matching the penetration depths and then further correlated to the target strengths. In the second case, a velocity-dependent pressure with a shape factor is considered. Numerical integration is required to obtain the penetration depths. The shape factor, which was first proposed by Alekseevskii without physical interpretation, is also correlated to mushroom strain. With these considerations, the previous singularity problem is removed and reasonably accurate predictions can be achieved.

DEVELOPMENT: A NEW PRESSURE LAW

Although Eqn (1) contains the motions of the mushroomed tip and the undeformed (rigid) part of the penetrator, its validity is undermined when the force (pressure) that controls deceleration is incorrectly assumed. The equations of motion are separately derived for the mushroom and the undeformed portions of the penetrator, as illustrated in Fig. 1. From the free body diagram of the mushroom, the equation of motion over the time t to $t + \Delta t$ is obtained from Newton's 2nd law:

$$\rho(-\Delta l A_0)\left[\frac{u - v}{\Delta t}\right] = \sigma A - \sigma_0 A_0. \tag{3}$$

The ratio in the bracket represents the acceleration of the mushroom over Δt. The area of the
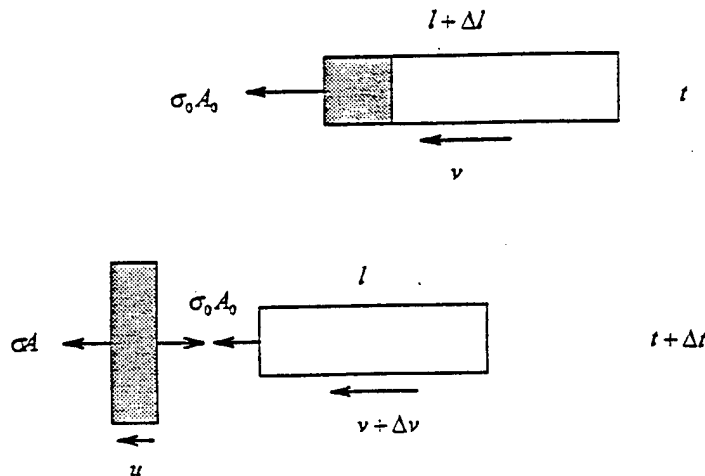
Fig. 1. Free body diagrams of the undeformed and mushroom head (shaded area) of a rod during the time interval Δt.

I-3

fully developed mushroom, A, and the area of the original penetrator, A_0, can be correlate to the engineering strain e:

$$e = \frac{A_0}{A} - 1. \tag{4}$$

Accordingly. let Δt approach zero and use Eqn (4), and Eqn (3) becomes

$$\rho \dot{l}(v - u) = \frac{\sigma}{1 + e} - \sigma_0. \tag{5}$$

Simil..iy, from the free body diagram of the undeformed section, the equation of motion has the form:

$$\rho A_0 l \frac{\Delta v}{\Delta t} = \sigma_0 A_0 \tag{6}$$

and let Δt approach zero, the Eqn (6) becomes

$$\rho l \dot{v} = \sigma_0. \tag{7}$$

Note that σ is the penetrator/target interface stress and σ_0 is the internal stress exerted between the plastic region and undeformed portion of the penetrator. Both of these two stresses are time-dependent in nature. Note that if we combine Eqn (5) and (7) by eliminating the term σ_0, the resulting equation is exactly the same as Eqn (1). Moreover, Eqn (7) is actually the equation of motion used by Tate [2], if we assume that σ_0 is the dynamic yield stress for the penetrator.

Now, we introduce the kinematic relationship derived by Wilson et al. [18], which has the form:

$$e\dot{l} = v - u. \tag{8}$$

By eliminating $\dot{l}$ term between Eqn (5) ... d (8) and solving for σ, we arrive at an expression for the target/penetrator interface stress (pressure):

$$P = -(1 + e)\left[\frac{\rho(v - u)^2}{e} + \sigma_0\right] \tag{9}$$

where σ has been replaced by P and the negative sign denotes ... pre ...n. Before we make further use of Eqn (9) to s. ...i penetration problem, more insight into this equation should first be made. If we comp...e Eqn (9) with the modified Bernoulli c used by Tate [2], the dimensionless coefficient of the term $(v - u)^2$, $-(1 + e)/e$, i... is more general than i/2. The socalled shape fac...r proposed by Alekseevskii [1] ca ...ected by this coefficient as well. It shou...' be clear that the mushroom strain influenc ...interface pressure.

A PENETRATION MODEL BASED ON CONSTANT PRESSURE

Based on Eqns (7–9), a new penetration model can be established once an estimate for P has been found. To begin, we assume that the target/penetrator interface pressure is approximately constant throughout the steady state. Actually, this assumption dates back to the early eighteenth century work of Robins and Euler [19]. However, it is only applicable to the penetration of nondeforming projectiles at low velocities [19, 20]. Considering the penetration of deforming penetrators, Christman and Gehring [21] used this assumption to typify steady state penetration. The validity of this assumption has also been discussed by Anderson et al. [9, 12] using a numerical simulation. Based on the constant pressure, the u–v relationship is thus obtained directly from Eqn (9) in terms of P:

$$u = v - \left[\frac{1}{\rho}\left(\frac{-e_1}{1 + e_1}P - e_1\sigma_0\right)\right]^{1/2} \tag{10}$$

where e has been replaced by e_1, which denotes the constant strain during quasi-steady state

penetration. Accordingly, the difference between the penetration velocity u and the current velocity v is also constant. Now, we incorporate Eqns (7) and (8) to obtain

$$\int_v^0 (v - u)dv = \frac{\sigma_0 e_1}{\rho} \int_{L_0}^{l_r} \frac{dl}{l} \tag{11}$$

where V is the initial impact velocity and l_f is the residual length of the undeformed section at the end of the steady-state phase. Because the difference between u and v is a constant, a direct integration of Eqn (11) gives

$$l_r = L_0 \exp\left(-\frac{K\rho V}{e_1 \sigma_0}\right) \tag{12}$$

where $K = v - u = $ constant, which comes from Eqn (10). By assuming that a final transient phase adds little to total penetration, the total steady-state penetration depth z at $u = 0$ can now be obtained by evaluating the integral:

$$z = \int u dt = \int \frac{u}{v} dv = \frac{\rho}{\sigma_0} \int_V^K (v - K)l dv. \tag{13}$$

After integration, a closed form solution for z can be found:

$$z = -\frac{\rho L_0}{a^2 \sigma_0}\left[\exp(a(K - V)) + (aV - aK - 1)\right] \tag{14}$$

where $a = \rho K/\sigma_0 e_1$ is a constant. It should be noted that σ_0 represents the dynamic yield strength of the penetrator, which is treated as an empirical constant. At this point, the remaining problem is how to find P.

Determining the constant pressure

One straightforward way to determine the constant pressure is to find the pressure that can best match the experimental data for penetration depth. The mushroom strain is obtained from the experimental data of crater diameters. It is noted that the current model does not explicitly account for the influence of the target strength factor (R) but that of the penetrator's dynamic yield strength σ_0. According to Anderson et al. [11], the penetration performance is more susceptible to the target strength than the penetrator strength. Consequently, it is anticipated that these P values may be correlated to target strengths. After investigating the experimental data, only the P values that best fit the penetration depths at low velocities (1 km/s–2 km/s) were obtained. Moreover, it is found that the value of P in each case is approximately twice the dynamic yield strength of the target. However, at higher velocities, this P–R relationship underestimates penetration performance. Conceptually, this can be understood from the impulse–momentum equation that develops the model. This approach relates the time-dependent (or velocity-dependent) penetration force to the product of a constant pressure and impact velocity-dependent mushroom strain (or area). At low impact velocities, the increasing force can be approximately reflected by the product because of increasing mushroom area, when impact velocity increases. However, as the impact velocity gets higher, the mushroom area is approaching some asymptotic limit [15], so the product cannot keep up with the increasing trend of the force. This accounts for the limitation of the application of constant pressure at lower velocities. On the other hand, for low-aspect-ratio penetrators, because a quasi-steady state penetration process may be very short, or may not even be reached, the assumptions of quasi-steady state and constant pressure are not appropriate. Besides, the dynamic yield strengths of some soft targets (like 1100-O AL and lead) are usually very strain-rate sensitive at higher strain rates [22, 23], so a constant value for R is not appropriate. Based on these considerations, the constant pressure model has been mainly used to investigate the cases involving aspect ratios greater than 10 and steel targets.

Prediction based on the constant pressure

A huge database of penetration mechanics compiled by Anderson et al. [24] has been used to examine the validity of the proposed models in this paper. The predictions based on
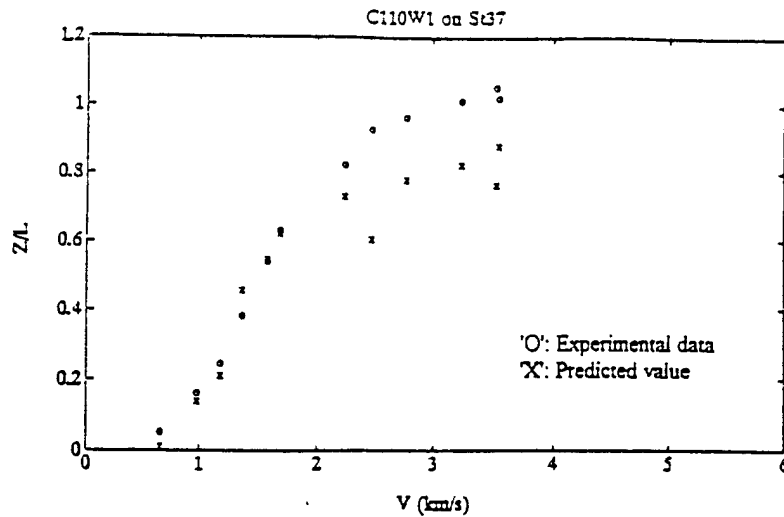
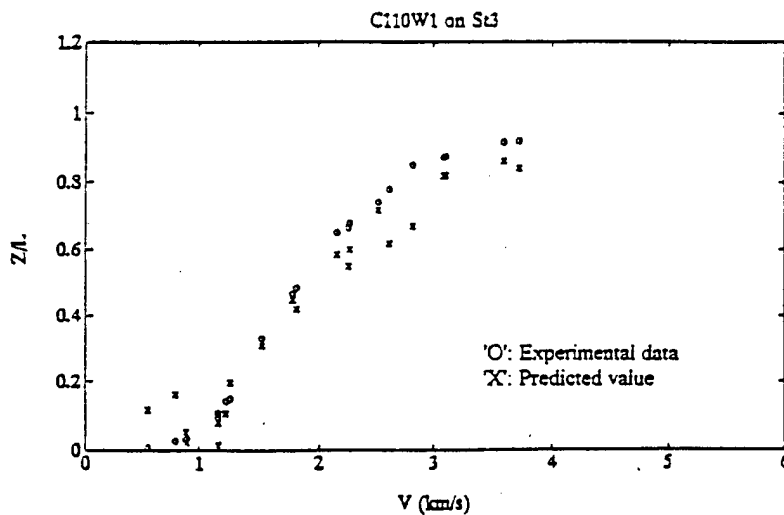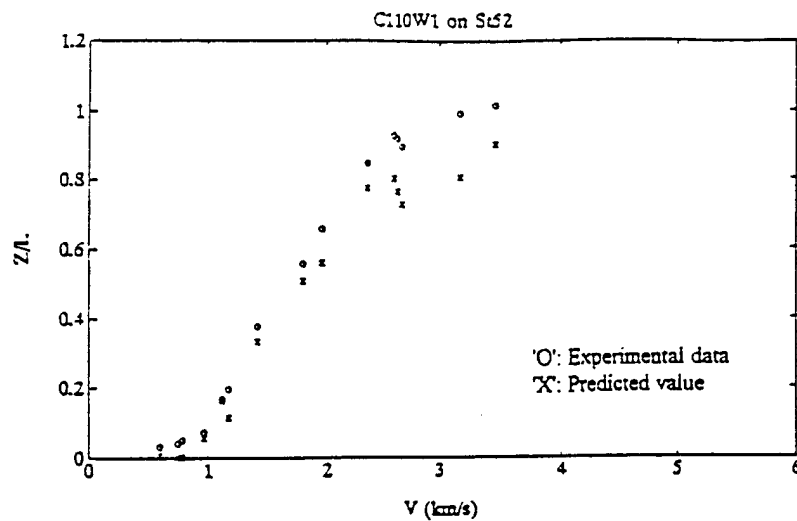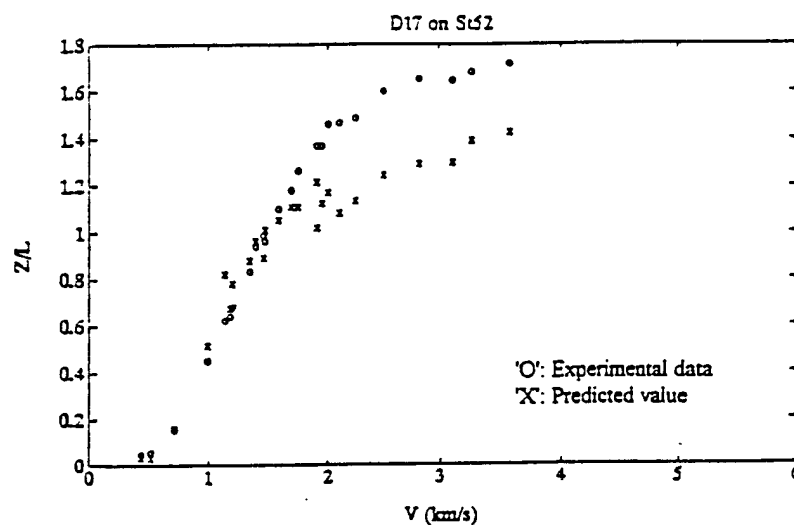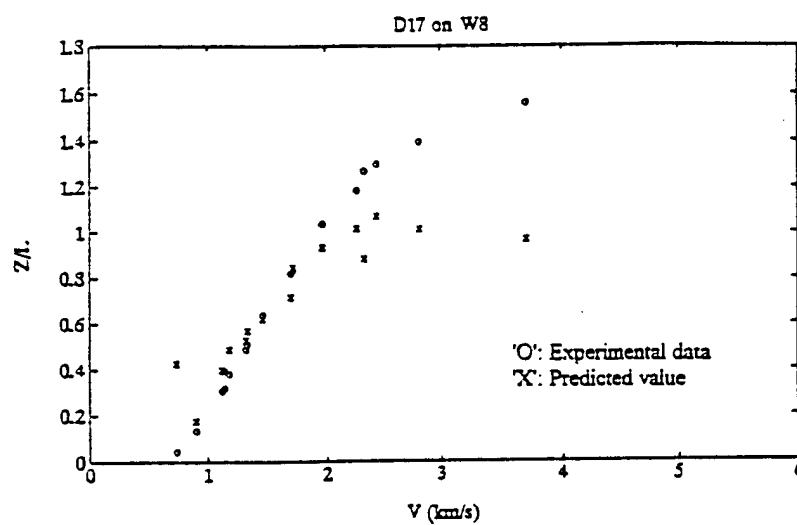Fig. 2. Normalized penetration depth (Z/L) vs impact velocity (V).

Fig. 3. Normalized penetration depth (Z/L) vs impact velocity (V).

constant pressure show common S-shaped penetration curves. For the cases involving steels against steels (e.g. Figs 2–4) and tungsten alloys against steels (e.g. Figs 5 and 6), the theoretical predictions (crosses) can reasonably match the experimental observations (circles) at velocities between 1 km/s and 2 km/s, but suffer considerable error when the velocities exceed 2 km/s. In addition to the previously stated limitation at low velocities, it is possibly due to inertia effects which become more significant relative to strength effects at higher velocities. Numerical simulation also shows that the magnitude of the nonsteady state of penetration increases with impact velocity, and that it contributes significantly to the total penetration at the higher impact velocities [12]. Thus, a velocity-dependent pressure will be invoked to cure the deficiency in the current model. The uncertainties in the experimental data of crater sizes apparently can cause some scattered predictions. For the cases investigated, realistic estimates for material strengths (σ_0 or R) have been used: C110W1–1200 MPA, St37–860 MPA, St52–960 MPA, St3–1300 MPA, D17–1600 MPA, and W8–1800 MPA.

C110W1 on St52

Fig. 4. Normalized penetration depth (Z/L) vs impact velocity (V).

D17 on St52

Fig. 5. Normalized penetration depth (Z/L) vs impact velocity (V).

D17 on W8

Fig. 6. Normalized penetration depth (Z/L) vs impact velocity (V).

I-7

A PENETRATION MODEL BASED ON VELOCITY-DEPENDENT PRESSURE

As the constant-pressure model has indicated, the accuracy of the prediction is reasonably good at low impact velocities (< 2 km/s) for long rods. The predicted S-shaped trend does not match well in the high velocity range ($\geqslant 2$ km/s). In addition to inertia effects at higher velocities, the interface pressure may change with the deformation at the penetrator tip (mushroom strain) and penetration velocities. The assumption of constant pressure throughout the quasi-steady state cannot account for these factors. Motivated by these observations, a velocity-dependent pressure is considered to modify the previous elementary pressure estimate.

Shape factor

Although Eqn (9) has represented the interface pressure P in terms of the current penetration velocity u and current undeformed section velocity v, one more equation is needed to construct the relationship between u and v if P is velocity-dependent. Let's recall the theory proposed by Alekseevskii [1], who considers the pressure balance across the target/penetrator interface and postulates the following equation:

$$Y + k_p \rho_p (v - u)^2 = R + k_t \rho_t u^2 \tag{15}$$

where k_p and k_t are shape factors that characterize the deformed regions in the penetrator and target materials, respectively. Y and R represent the dynamic strength of the penetrator and target, respectively. Simply indicating that these two shape factors depend on the flow geometry and assuming that they are approximately 1/2 based on the hydrodynamic model, Alekseevskii does not give any further physical insight into these factors. Swanson and Donaldson [25] proposed a so-called integral theory of impact to model the long rod penetration process. In their model, they assume the target/penetrator interface pressure is governed by fluid drag, C_d, and the adiabatic hardness. The adiabatic hardness is used to explain the strength factor for the target and is defined as the product of the target density, ρ_t, and the energy per unit mass dissipated in the form of plastic work as the target flows around the penetrator, E_t^*. Thus, the interface pressure assumes the following form:

$$P = \rho_t \left(\frac{C_d}{2} u^2 + E_t^* \right) \tag{16}$$

where u is penetration velocity. It is not difficult to find that the dimensionless drag factor C_d in Eqn (16) plays a very similar role to the shape factor k_t in Eqn (15). Lately, Rosenberg et al. [5] considered the equilibrium of force at rod/target interface by introducing effective cross-sectional areas of the rigid rod and its mushroomed front end to the modified Bernoulli equation. The resultant area ratio, which was specifically taken as two in their model, is somewhat like the shape factor mentioned by Alekseevskii [1]. On the other hand, the coefficient $-(1 + e_1)/e_1$ in Eqn (9) has also revealed the possible physical meaning of the shape factor k_p in Eqn (15). Based on the above overview of the shape factor, it is reasonable to assume that the pressure has the form:

$$P = k_t \rho_t u^2 + R = -(1 + e_1) \left[\frac{\rho (v - u)^2}{e_1} + \sigma_0 \right] \tag{17}$$

where k_t is a constant and will be determined later. R represents the dynamic yield strength of the target, which for example, can be determined by a Taylor impact test. Equation (17) thus establishes a new u–v relationship. Particularly, if k_t and $-(1 + e_1)/e_1$ are both set equal to 1/2, then Eqn (17) returns the modified Bernoulli equation. Or, in other words, the modified Bernoulli equation is a special case of Eqn (17) when $e_1 = -2/3$ and the penetrator's strength (Y) is one third of its dynamic yield strength. It is interesting to note that $e_1 = -2/3$ is the critical value of the tip strain in the earlier penetration theory of Jones et al. [14], which was further elaborated by Gillis et al. [26].

Derivation of the model

A new penetration model based on velocity-dependent interface pressure can be developed by incorporating Eqn (7), (8), and (17). For the sake of convenience, we rewrite Eqn (17) as

$$P = k_1 u^2 + R = k_2(v - u)^2 + Y \tag{18}$$

where

$$k_1 = k_t \rho,$$

$$k_2 = -\left(\frac{1 + e_1}{e_1}\right)\rho_p,$$

and

$$Y = -(1 + e_1)\sigma_0.$$

Note that σ_0 is negative because it is a compressive stress. From Eqn (18), we can rearrange and get a quadratic equation in u:

$$(k_1 + k_2)u^2 + 2k_2 vu + (k_3 - k_2 v^2) = 0 \tag{19}$$

where $k_3 = R - Y$. A further solution for u depends on the sign of the coefficient $(k_1 - k_2)$. By letting $\zeta^2 = k_1/k_2$, u can be written in the following form:

$$u = \frac{v - \zeta[v^2 - A]^{1/2}}{1 - \zeta^2} \tag{20}$$

for $k_1 \neq k_2$, and $A = \dfrac{k_3}{k_1}(1 - \zeta^2)$, or

$$u = \frac{k_2 v^2 - k_3}{2k_2 v} \tag{21}$$

for $k_1 = k_2$. Based on Eqns (20) and (21), the residual length of the penetrator can be obtained by evaluating the integral in Eqn (11). Consequently, the residual penetrator length has the form:

$$\frac{l}{L_0} = \left[\frac{v + \sqrt{v^2 + A}}{V + \sqrt{V^2 + A}}\right]^{[\rho A \zeta/2e_1\sigma_0(1 - \zeta^2)]}$$

$$\times \exp\left[\frac{\rho\zeta}{2e_1\sigma_0(1 - \zeta^2)}\left[(v\sqrt{v^2 + A} - \zeta v^2) - (V\sqrt{V^2 + A} - \zeta V^2)\right]\right] \tag{22}$$

for $k_1 \neq k_2$, or

$$\frac{l}{L_0} = \exp\left[\frac{\rho}{4e_1\sigma_0}(v^2 - V^2)\right]\left[\frac{v}{V}\right]^{(\rho k_3/2k_2 e_1\sigma_0)} \tag{23}$$

for $k_1 = k_2$. Now, the penetration depth z can be obtained by solving

$$z = \int u \, dt = \int \frac{u}{\dot{v}} \, dv = \frac{\rho}{\sigma_0}\int u l \, dv \tag{24}$$

which is similar to Eqn (13). A numerical integration is required to evaluate the integral in Eqn (24).

According to Tate's theory [27], there exists a critical velocity during the deceleration of the penetrator, below which rigid body penetration will continue if $Y > R$ and a further erosion of the penetrator without gaining penetration depth will continue if $Y < R$. A similar consideration can be made for the current model.

I-9

I. *Rigid body penetration.* This implies $v = u$ and l is constant, so we can solve for the critical velocity v_c from Eqn (18):

$$v_c = \left[\frac{Y - R}{k_1} \right]^{1/2}. \tag{25}$$

Because the penetrator remains rigid in this stage, the interface pressure should be the stress responsible for decelerating the residual penetrator (with mushroom tip and constant length). Hence, we transform Eqn (7) to

$$\rho_p l_c \dot{v} = -(k_1 v^2 + R) \tag{26}$$

where l_c represents the residual length that corresponds to $v = v_c$, and can be found from either Eqn (22) or Eqn (23). Integrating Eqn (24) by using Eqn (26), the penetration depth during this stage is obtained:

$$z_c = \frac{\rho_p l_c}{2k_1} \ln \left[\frac{k_1 v_c^2 + R}{R} \right]. \tag{27}$$

Thus, when $T > R$, the total penetration depth is equal to the sum of Eqns (24) and (27).

II. *Erosion without penetration.* This implies $u = 0$, so we can solve for the critical velocity v_c from Eqn (18):

$$v_c = \left[\frac{R - Y}{k_2} \right]^{1/2}. \tag{28}$$

In this stage, the interface pressure is not high enough to make the target material deform, but high enough to continue the material flow across the rigid–fluid interface of the penetrator. Therefore, the undeformed section of the penetrator is decelerated by its dynamic yield strength. That is, Eqn (7) is still valid. Accompanied with Eqn (8) $(u = 0)$, Eqn (7) can be integrated to give the final length:

$$l_f = l_c \exp \left[-\frac{\rho v_c^2}{2 e_1 \sigma_0} \right]. \tag{29}$$

From the previous discussion, it is likely that most of the penetration problems fall in the second type, erosion without penetration. This is because the strength factor of penetrator (Y) is reduced by the factor $-(1 + e_1)$. This implies that at the end of penetration, once $v < v_c$, the second type of penetration is the most likely case. Up to this point, we have established a new penetration model based on a new pressure law, but the shape factor k_t is still unknown.

Determining the shape factor

In order to investigate the behavior of the shape factor, we find its value for each shot by matching the experimental depth data. Motivated by the previous observation that the shape factor k_p is a function of e_1, we make the same assumption for k_t. After examining all the cases, a common trend can be found:

$$
\begin{aligned}
k_t(e_1) &\to \infty \quad \text{when } e_1 \to e_0 \\
k_t(e_1) &\to 0 \quad \text{when } e_1 \to -1
\end{aligned}
\tag{30}
$$

where e_0 and k_0 are both constants. This relation implies that the shape factor becomes large when the mushroom strain approaches some constant (at low velocities) and approaches a small constant value when the mushroom strain approaches -1 (at high velocities). From another viewpoint, this relation is also conceptually similar to the definition of the drag coefficient. Based on Eqn (30), the hyperbolic-type property of $k_t(e_1)$ can be approximated by taking the first three terms of a power series of the form: $\sum_{n=0}^{n=\infty} c_n (e_1 - e_0)^{-n}$. That is,

$$k_t \cong c_0 + \frac{c_1}{(e_1 - e_0)} + \frac{c_2}{(e_1 - e_0)^2} \tag{31}$$

I-10

where c_0, c_1, and c_2 are constants to be determined after a value of e_0 has been assumed. For most of the cases, e_0 is chosen to comply with $k_t = 0$ when $e_1 = -1$. That is, k_0 in Eqn (30) is normally zero. In only one case, "AL alloy on lead", has k_t been non-zero as e_1 approaches -1. In such cases, a maximum trend for the penetration curve can be obtained. On the other hand, it is also found that for most high-aspect-ratio $(L/D \geqslant 10)$ cases, c_0 can be simply set equal to zero. The exceptions to this are the low-aspect-ratio cases $(L/D = 3)$, "1100-O AL on 1100-O AL" and "C1015 steel on C1015 steel". In these cases, c_0 has a significant contribution in determining k_t. However, a further attempt to find regularities among these three constants, or to correlate these constants to other physical parameters, is difficult due to many untractable uncertainties in material properties.

Prediction based on velocity-dependent pressure

By using the strains predicted by the initial transient analysis from Wang and Jones [28], the current model is again tested with a large volume of experimental data. Some selected results predicted by the model, compared with the experimental data, have been presented graphically in the form of normalized penetration depth (Z/L) vs impact velocity (V). The predicted results agree well with the experimental data over an impact velocity range of 0–4 km/s. The S-shaped curve is also reasonably well reflected by the model.

As Fig. 7 shows for the case of aluminum alloy penetrators against lead targets $(L/D = 10$, $\sigma_0 = 275$ MPa, and $R = 60$ MPa), the current model can successfully show the maximum trend of penetration performance, which cannot be achieved in some of our previous work. Figure 8 shows reasonable agreement throughout the whole impact velocity range for the case of D17 WA against St52 steel targets $(L/D = 10, \sigma_0 = 1600$ MPa, and $R = 960$ MPa). As to the cases of C1015 steel on C1015 steel $(L/D = 3, \sigma_0 = R = 650$ MPa) and 1100-O AL on 1100-O AL $(L/D = 3, \sigma_0 = R = 160$ MPa) shown in Figs 9 and 10 respectively, the increasing trends to Z/L at higher velocities $(V > 2$ km/s), which cannot be captured by our previous models [4, 16], can now be accurately predicted by the current model.

CONCLUSION

In this paper, an attempt has been made to modify the modified Bernoulli equation used by Tate. By decomposing the equation of motion proposed by Jones *et al.* [14] into two parts, a new analytical form for the interface pressure has been developed. This pressure form is more general than the modified Bernoulli equation because the mushroom strain effect is included. As a first approximation, a constant interface pressure (P) was assumed dominant through the quasi-steady state, which gives a new relation between the current tail and the
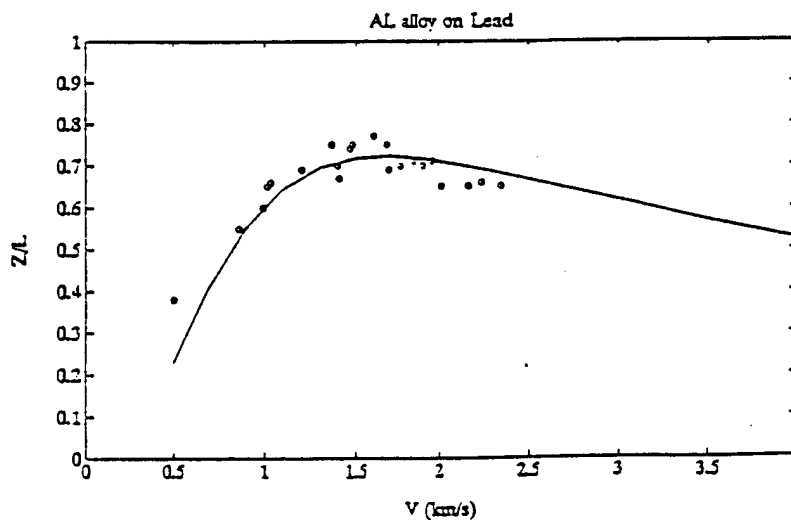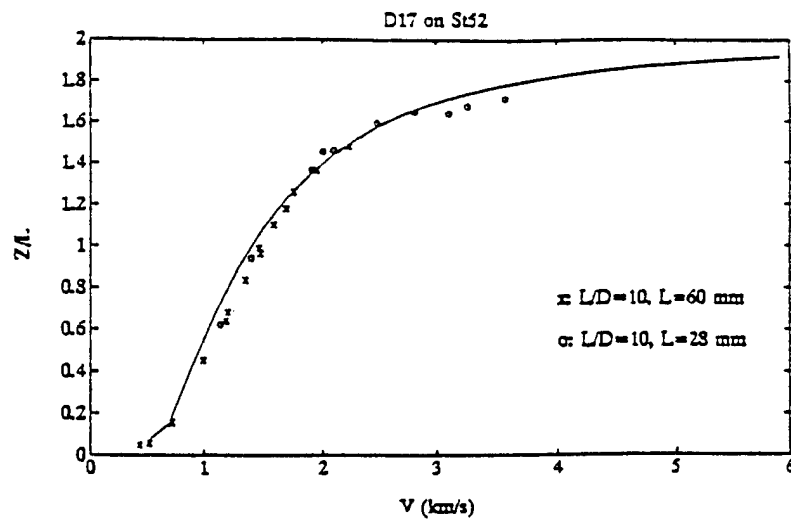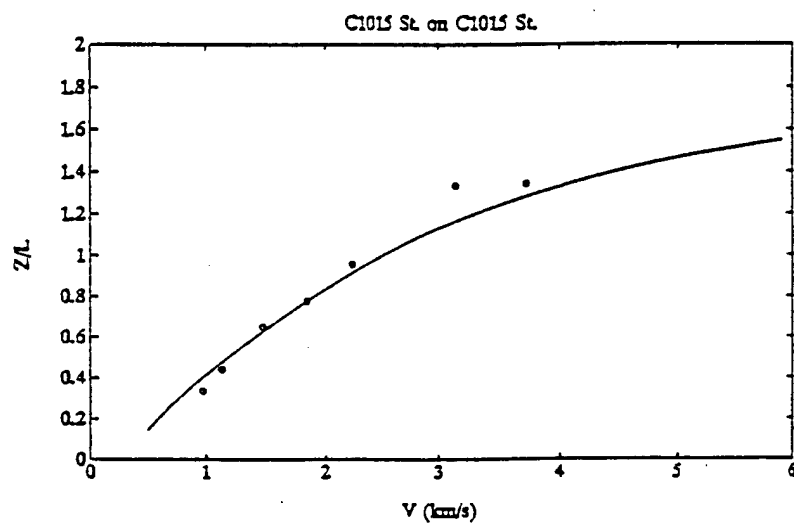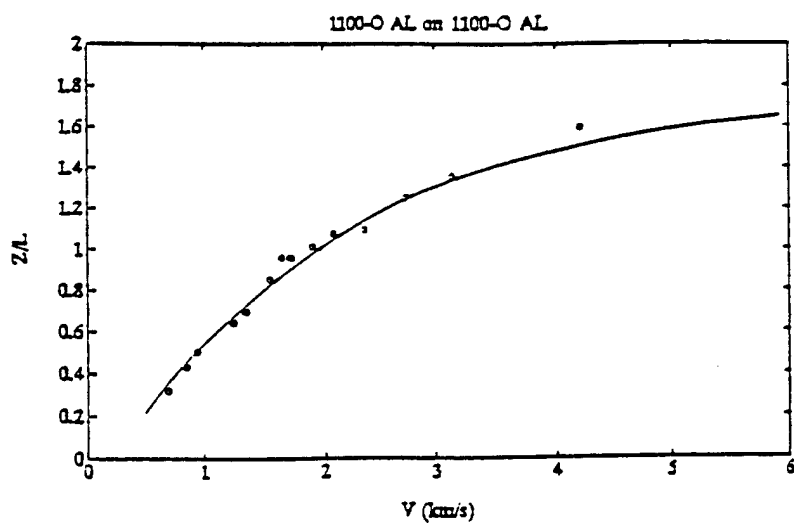

Fig. 7. Normalized penetration depth (Z/L) vs impact velocity (V).

Fig. 8. Normalized penetration depth (Z/L) vs impact velocity (V).

Fig. 9. Normalized penetration depth (Z/L) vs impact velocity (V).

Fig. 10. Normalized penetration depth (Z/L) vs impact velocity (V).

penetration velocity [Eqn (10)]. By employing the experimental strains, P for each case is found and is approximately twice of R. Based on this constant pressure, the model can be integrated analytically and a closed-form solution for penetration is obtained. This removes the singularity problem that has often prevented the integration of the equations of motion introduced by Jones et al. [14]. However, the predicted penetration depths show reasonable agreement only in cases with low impact velocities and large aspect ratio. Moreover, most of these cases involve WA or steel penetrators against steel targets. For the penetrations at higher velocities, a constant P-R relationship may lose effectiveness because the effect of inertia and the contribution of nonsteady state penetration become more significant. Accordingly, the pressure distribution may be more velocity-dependent. Despite these disadvantages, the constant-pressure model reveals a promising direction for the construction of a new pressure law.

Motivated by the constant-pressure model, a velocity-dependent pressure law was formulated. The new pressure law is suggested by equating the previously developed pressure from the viewpoint of the penetrator to an assumed pressure with a similar structure from the viewpoint of the target. By recalling the original theory proposed by Alekseevskii [1], the obscure "shape factor" was reconsidered and identified in terms of the new pressure law. From the viewpoint of the penetrator, the shape factor is a function of the mushroom strain, but from the viewpoint of the target, the shape factor (k_t) cannot be obtained a priori and has to be determined by examining the experimental data. All the distributions of k_t vs the strain were commonly hyperbolic, which can be approximated by an inverse power series expansion with respect to the strain. Nevertheless, further effort failed to correlate the coefficients of the series to known physical parameters. However, with the shape factor added to the model, the system can be integrated numerically without any singularity problem.

This model gives a more accurate prediction than the constant-pressure model, as long as the shape factor is properly chosen and a correct strain trend is determined. It is noteworthy that the velocity-dependent pressure enables the model to capture the maximum trend of the penetration curves for soft targets, which has invalidated some of the previous models. For penetrations by low-aspect-ratio penetrators, better agreement can be achieved because the shape factor probably has offset the deficiency of the assumption of quasi-steady state by taking the flow geometry at the penetrator/target interface into account.

Finally, as a comparison with the numerical simulation made by Anderson et al. [12], by choosing an average mushroom strain of -0.8, the pressure predicted by the velocity-independent model is plotted as a function of impact velocity for the shot combination of D17 on W8 [24] in Fig. 11. The increasing trend of pressure with impact velocity is generally consistent with the observation from numerical simulation when e is constant. On the other
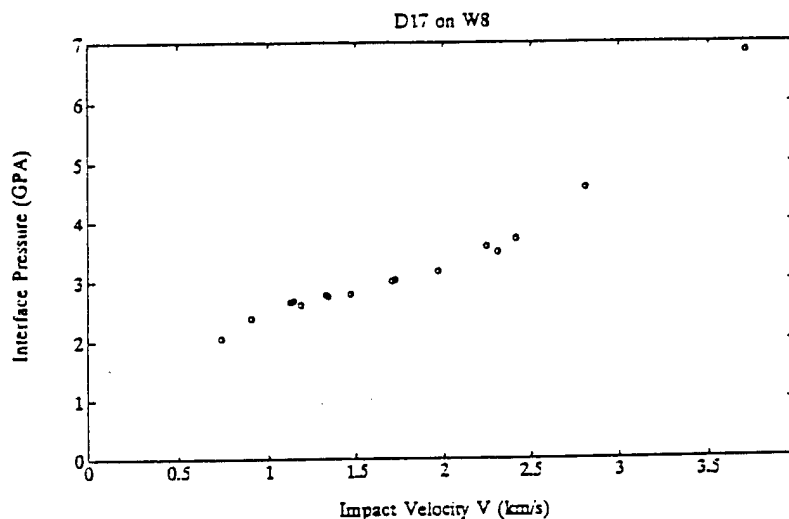

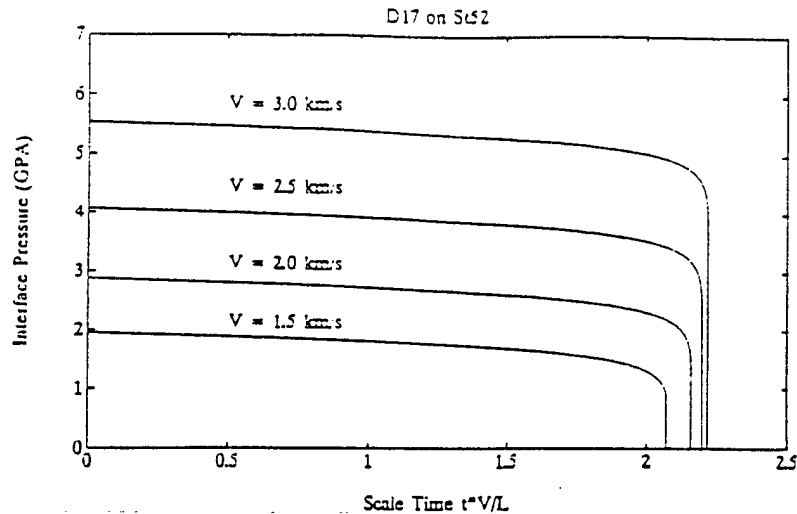Fig. 11. Interface pressure (P) predicted by velocity-independent model vs impact velocity (V).

Fig. 12. Interface pressure (P) predicted by velocity-dependent model vs scale time (tV/L).

hand, the pressure predicted by the velocity-dependent model is plotted as a function of scaled time for the shot combination of D17 on St52 [24] in Fig. 12. By choosing an average mushroom strain of -0.8 and four typical impact velocities, similar to those used by Anderson *et al.* [12], similar increasing trends of pressure with impact velocity are obtained. However, the predicted pressure is apparently much lower than that obtained from the numerical simulation. This is due to the increase in area at the penetrator tip. A compressive strain -0.8 is the equivalent to increasing the diameter by a factor of 2.24.

REFERENCES

1. V. P. Alekseevskii. Penetration of a rod into a target at high velocity. *Combustion, Explosion, and Shock Waves* **2**, 63–66 (1966).
2. A. Tate, A theory for the deceleration of long rods after impact. *J. Mech. Phys. Solids* **15**, 387–399 (1967).
3. A. Tate. Long rod penetration models—Part I. A flow field model for high speed long rod penetration. *Int. J. Mech. Sci.* **28**, 353–548 (1986).
4. A. Tate. Long rod penetration models—Part II. Extensions to the hydrodynamic theory of penetration. *Int. J. Mech. Sci.* **28**, 599–612 (1986).
5. Z. Rosenberg, E. Marmor and M. Mayseless. On the hydrodynamic theory of long-rod penetration. *Int. J. Impact Engng* **10**, 483-486 (1990).
6. T. W. Wright. Penetration with long rods: a theoretical framework and comparison with instrumented impacts. ARBRL-TR-02323, U.S. Army Ballistic Research Laboratory, Aberdeen Proving Ground, MD (1981).
7. T. W. Wright. A survey of penetration mechanics for long rods. In *Computational Aspects of Penetration Mechanics* (Edited by J. Chandra and J. E. Flaherty), *Lecture Notes in Engineering*, pp. 85–196. Springer-Verlag, Berlin-Heidelberg (1983).
8. T. W. Wright and K. Frank. Approaches to penetration problems. In *Impact: Effects of Fast, Transient Loadings* (Edited by W. J. Amman, W. K. Liu, J. A. Studer and T. Zimmermann). A. A. Balkema, Rotterdam (1988).
9. C. E. Anderson and J. D. Walker, An examination of long-rod penetration. *Int. J. Impact Engng* **4**, 481–501 (1991).
10. J. D. Walker and C. E. Anderson, A nonsteady-state model for penetration. *Proc. 13th Int. Symp. on Ballistics*, Stockholm, Sweden (1992).
11. C. E. Anderson, J. D. Walker and G. E. Hauver. Target resistance for long-rod penetration into semi-infinite targets. *Nucl. Engng Design* **138**, 93–104 (1992).
12. C. E. Anderson, D. L. Littlefield and J. D. Walker, Long-rod penetration, target resistance, and hypervelocity impact. *Int. J. Impact Engng* **14**, 1–12 (1993).
13. F. I. Grace, Nonsteady penetration of long rods into semi-infinite targets. *Int. J. Impact Engng* **14**, 303–314 (1993).
14. S. E. Jones, P. P. Gillis and J. C. Foster, Jr., On the penetration of semi-infinite targets by long rods. *J. Mech. Phys. Solids* **35**, 121–131 (1987).
15. J. D. Cinnamon, S. E. Jones, J. W. House and L. L. Wilson, A one-dimensional analysis of rod penetration. *Int. J. Impact Engng* **12**, 145-166 (1992).
16. J. D. Cinnamon. Further one-dimensional analysis of long-rod penetration of semi-infinite targets. Master's Thesis, The University of Texas at Austin (1992).
17. P. Wang and S. E. Jones, An elementary theory of one-dimensional rod penetration using a new estimate for pressure. (Abstract). *Proc. Annual Meeting of the Society of Engineering Science*, College Station, Texas, October (1994).

18. L. L. Wilson, J. C. Foster, S. E. Jones and P. P. Gillis, Experimental rod impact results. *Int. J. Impact Engng* **8**, 15–25 (1989).
19. W. Johnson, *Impact Strength of Materials*. pp. 306. Edward Arnold, London (1972).
20. J. S. Rinehart and J. Pearson, *Behavior of Metals under Impulsive Loads*. pp. 199–200. The American Society for Metals, Cleveland Ohio (1954).
21. D. R. Christman and J. W. Gehring, Analysis of high-velocity projectile penetration mechanics. *J. Appl. Phys.* **37**, 1579–1587 (1966).
22. U. S. Lindholm, Some experiments with the split Hopkinson pressure bar. *J. Mech. Phys. Solids* **12**, 317–335 (1964).
23. U. S. Lindholm and L. M. Yeakley, High strain-rate testing: tension and compression. *Exp. Mech.* **8**, 1–9 (1968).
24. C. E. Anderson, B. L. Morris and D. L. Littlefield, A penetration mechanics database. SWRI Report 3593/001, Southwest Research Institute, San Antonio, TX (1992).
25. C. V. Swanson and C. duP. Donaldson, Application of the integral impact theory to modeling long-rod penetrators. Aeronautical Research Associates of Princeton, ARAP Report 333 (1978).
26. P. P. Gillis, S. E. Jones, L. L. Wilson and J. C. Foster, An analytical and experimental approach to the penetration of semi-infinite targets by long rods. In *Recent Advances in Impact Dynamics of Engineering Structures*. ASME-AMD-Vol. 105 (Edited by D. Hui and N. Jones) (1989).
27. A. Tate, Further results in the theory of long rod penetration. *J. Mech. Phys. Solids* **17**, 141–150 (1969).
28. P. Wang and S. E. Jones, An analysis of one-dimensional penetration using a revised estimate for impulse. *SECTAM XVII Conf.*, Hot Springs National Park, Arkansas, April 10–12 (1994).

APPENDIX J

AN ANALYSIS OF ONE-DIMENSIONAL PENETRATION USING A REVISED ESTIMATE FOR IMPULSE

Ping Wang[1] and S. E. Jones[2]

ABSTRACT

In this paper, a more detailed estimate for the impulse of the external forces acting on a deforming, rigid-plastic penetrator has been made. This result is used in the initial transient analysis introduced by Cinnamon, et al. (1992a) to produce a new estimate for penetration depth. A new parameter, called the impulse factor, correlates with the dynamic strengths of the penetrator and target materials. The predicted results are in good agreement with most of the experimental data.

Introduction

Alekseevskii (1966) and Tate (1967, 1969) independently proposed a simple one-dimensional analytical model to simulate the normal penetration of a semi-infinite target by an instantaneously eroding cylindrical rod. Based on the assumption of quasi-steady state penetration, a modified hydrodynamic equation (or modified Bernoulli equation) was introduced to relate the interface pressure between the penetrator and target to their dynamic yield strengths and to the penetrator and penetration velocities. Due to its simplicity and its ability to make qualitative predictions, Tate's theory has become a standard reference in one-dimensional engineering models to explore the terminal ballistic behavior of long rods against semi-infinite targets. A series of experimental investigations on different tungsten alloys and steel alloys impacting different armor steel targets at velocities between 0.5 km/s and 4 km/s were conducted by Hohler and Stilp (1977, 1980, 1984, 1987) to investigate the validity of Tate's model. One factor that is widely considered controversial but vital to Tate's model is how to decide the

[1]Graduate student, Department of Engineering Science and Mechanics, The University of Alabama, Tuscaloosa, AL 35487
[2]University Research Professor, Department of Engineering Science and Mechanics, The University of Alabama, Tuscaloosa, AL 35487

dynamic yield strength or target resistance. A variety of attempts to estimate target strength analytically thus became the focus of many efforts in verifying or revising Tate's theory. On the other hand, Wright (1981, 1983) indicated the flaws of Tate's assumptions of steady state and rigid-plastic behavior of materials and questioned the validity of using the modified Bernoulli equation to describe the stress applied at the target/penetrator interface. Lately, Anderson and Walker (1991) made a further examination of Tate's model with the aid of numerical simulation. On the basis of discrepancies in the prediction between Tate's model and the numerical simulation, Walker and Anderson (1992) proposed a nonsteady-state penetration model. Anderson, et al. (1992a) also reported that target resistance varies considerably during penetration and that the resistance value used in Tate's model should be considered as an average value to give the correct penetration depth. Using information provided by numerical simulation, these authors proposed many possible directions to modify Tate's model, but not much progress was made in developing analytical techniques.

In 1987, Jones, Gillis, and Foster (1987) used the impulse-momentum equation to modify the equation of motion derived by Tate. A further modification was made by Wilson, et al. (1989) on the kinematic equations by considering the conservation of mass across the plastic interface between the mushroom and the uneroded portion of the rod. In the revised model, the engineering strain of the mushroom tip of the penetrator was assumed constant and obtained by measuring the diameters of craters in targets. Nevertheless, the modified Bernoulli equation was still used. The dynamic yield strengths of targets and penetrators were also assumed constants and treated as empirical quantities. In order to remove dependence of mushroom strain on post-test measurement, a linear crater volume-kinetic energy relationship was applied by Kerber, et al. (1992). Due to the assumption of steady-state behavior for the whole penetration process, the predicted results were satisfactory for longer rods and higher impact velocities, but not well correlated for shorter and lower velocities where the initial transient state should not be ignored. Cinnamon, et al. (1992a) thus adapted the governing equation to the transient state by presuming negligible deceleration and constant penetration velocity during the initial transient. This transient analysis, accompanied with the crater volume-kinetic energy relationship, made it possible to calculate crater diameters and penetration depths in a completely algebraic way. On the other hand, a specific factor, which was correlated to target strengths, was introduced to describe the variation of the interface pressure across the mushroom tip. Due to this factor, the interface pressure estimated by the modified Bernoulli equation was reduced and reasonable predictions for penetration depths were obtained for impact velocities between 1 km/s and 3 km/s. However, for impact velocities above 3 km/s, this model tended to over-predict the penetration depths. Believing that the pressure was too high, Cinnamon (1992) made a further pressure analysis and found that if the average pressure at steady state was presumed to be constant over the range of impact velocities for particular shot combinations, then reasonable penetration results could be predicted. Again, this average pressure was successfully correlated to target strength. A huge database of penetration tests compiled by Anderson et al. (1992b), which embraces a wide range of impact velocities and various kinds of target and penetrator materials, was used to examine the validity of the model based on the combination of the new pressure analysis, transient analysis and crater volume-kinetic energy relationship. The results showed the trend of penetration depths converges as the high velocity regime is reached, which is in agreement with most experimental observations.

In this paper, a re-examination is made of the impulse-momentum relationship derived by Jones, et al. in 1987. Considering the impulse due to the nonlinear time-dependent force exerted on a rod which transitions from an undeformed state to a fully deformed state (mushroom), an important factor called the impulse factor is introduced to evaluate the time integral of force (impulse). Based on the initial transient analysis, the impulse factor is found dependent on two dimensionless parameters, which play a significant role in characterizing the trend of the mushroom strain at the transition point between transient and steady state penetration. By matching the available experimental data of crater diameters and penetration depths, one of the parameters is found to have a constant value and the other one can be correlated to the dynamic yield strength factors of penetrators and targets. Because the impulse factor more practically accounts for the effect of impulse during penetration, the current study has suggested an alternative way to modify previous models from an aspect that is different from pressure reduction. Computational results show that the current model has good predictive capability over a fairly wide range of penetrator and target combinations.

Theory

1. **Impulse factor.** In 1987, Jones, et al. modified Tate's model by separating the rod material into rigid (undeformed) and plastic (deformed) regions during the penetration process (Fig. 1). They examined the balance of impulse and momentum across the deformed and undeformed sections (Fig. 2). By assuming a linear force-time relation (Fig. 3-a), the impulse integral was thus simply estimated by the rectangular area under the force-time curve. The force was further correlated to the modified Bernoulli pressure P_B. Accordingly, the equation of motion was obtained by dividing by Δt and taking the limit as Δt approaches to zero:

$$l\dot{v} + \dot{l}(v - u) = -\frac{P_B}{\rho(1+e)} \tag{1}$$

In this equation, v is the velocity of the undeformed section, u is the penetration velocity, l is the undeformed section length, ρ is the constant penetrator mass density, P_B is the interface pressure (the modified Bernoulli pressure) between the penetrator tip and the target and e is the engineering strain in the deformed section of the penetrator adjacent to the rigid-plastic interface. According to the modified Bernoulli equation, P_B is represented by

$$P_B = \frac{1}{2}\rho_t u^2 + R_t = \frac{1}{2}\rho(v - u)^2 + Y_p \tag{2}$$

where ρ_t is the density of target, and R_t and Y_p are the dynamic yield strengths of the target and penetrator, respectively. Due to Eq. (2), a relationship between u and v is also uniquely defined.

Despite the simple way of estimating the impulse during penetration, this model ignored possible nonlinear force-time relation (Fig. 3-a) that may be attributed to different impact velocities and material properties. In a related problem, Ipson and Recht (1975) investigated the structure of this integral. However, the impulse integral cannot be obtained precisely because a knowledge of the actual force-time relation is usually not available. In order to overcome this

problem, we invoke the mean value theorem of integral in calculus to estimate the impulse, which is schematically shown in Fig. (3-b). According to the theorem, if the integrand is continuous, the integral can be replaced by:

$$\text{Impulse} = \int_{t}^{t+\Delta t} F(\xi)d\xi = F(\tau)\Delta t \qquad (3)$$

where $t \leq \tau \leq t - \Delta t$. We assume that $F(\tau)$ can be denoted by a positive real factor n, called the impulse factor, multiplied by F_1. If we now repeat the procedure for deriving Eq. (1), then we have:

$$l\dot{v} + \dot{l}(v - u) = -\frac{nP_3}{\rho(1+e)} \qquad (4)$$

Note that Eq. (4) only differs from Eq. (1) by the factor n but reduces to Eq. (1) when n is set equal to one. The impulse factor will be used in the transient analysis.

2. Initial Transient Analysis. Following the assumptions made by Cinnamon, et al. (1992a) to characterize the initial transient phase, we arrive at the transition between transient and steady state, and Eq. (4) becomes:

$$\dot{l}(v_0 - u_0) = -\frac{nP_3}{\rho(1+e_1)} \qquad (5)$$

where v_0 is impact velocity, u_0 is penetration velocity at impact and e_1 is the mushroom strain when steady state is reached. Another equation which accounts for the conservation of mass across the mushroom is:

$$e_1\dot{l} = v_0 - u_0 \qquad (6)$$

Eqs. (5) and (6) govern the mushrooming process during the transient phase until steady state is reached. By eliminating $\dot{l}$ between Eq. (5) and Eq. (6) and rearranging, we obtain:

$$\frac{\rho(v_0 - u_0)^2}{P_3} = -\frac{ne_1}{(1+e_1)} \qquad (7)$$

In order to estimate the behavior of the impulse factor n, we rewrite Eq. (7) as:

$$Y = nX \qquad (8)$$

where $X = -e_1/(1+e_1)$ and $Y = \rho(v_0 - u_0)^2/P_3$ and then evaluate the X-Y relation with the penetration database compiled by Anderson et al. (1992b). An important X-Y relation can be obtained for each combination of shot by a least-squares fit:

J-4

$$Y = \alpha + \frac{\beta}{X} \qquad (9)$$

where α and β are two least-square coefficients. Using Eqs. (8) and (9), the impulse factor n can be found:

$$n = \frac{1}{X}(\alpha + \frac{\beta}{X}) \qquad (10)$$

Thus we can solve for the strain e_1 by substituting n back into Eq. (7):

$$e_1 = \frac{\beta(\frac{P_B}{\rho})}{-(v_0 - u_0)^2 + (\alpha - \beta)(\frac{P_B}{\rho})} \qquad (11)$$

3. Determining α and β. As shown in Eq. (10) the impulse factor is dependent on two dimensionless constants α and β. One way to find these two constants is to match the theoretical strains predicted by Eq. (11) to the experimental strains. However, a limited number of shots for each material combination, which are often subject to uncertainties, and different choices of impact velocity, make it difficult to precisely find the impulse factor by only matching the strain trend. This drawback is especially apparent in the higher velocity regimes, where small errors in predicting strains usually results in considerable errors in predicting penetration depth when the linear kinetic energy-crater volume relation is applied. On the other hand, the impulse factor should be able to reflect a well-known experimental observation--the saturation region at high velocities. Based on the above observations, α and β will be selected to match the following equation for penetration depth z derived by Cinnamon, et al. (1992a)

$$z = \frac{1}{A}(1 + e_1)(aE_0 + b) \qquad (12)$$

where E_0 is kinetic energy of the penetrator at impact, A is initial cross-section area of penetrator and a, b are the slope and intercept of the kinetic energy-crater volume line respectively.

After matching the predicted results obtained from Eq. (11) and Eq. (12) with the experimental data case by case, it is found that agreement with Eq.(12) only occurs when α is equal to two, and the values of β vary as the dynamic yield strengths of penetrators and targets. Further investigation shows β can be approximated by the dynamic yield strength ratios of penetrators to targets (Fig. 4). Using a least-square scheme to correlate β to strength ratio, we find:

$$\beta = -0.3947 - 1.5687(\frac{Y_p}{R_t}) \qquad (13)$$

It should be noted that the dynamic yield strengths used in this paper refer to the compressive strengths measured by a Taylor anvil test or by a split Hopkinson bar test at high strain rates. Some of the information for dynamic strengths can be found in some previously reported papers or experimental reports. For the cases where no dynamic strength data are available, the strengths are estimated from the formula suggested by Tate (1986). However, dynamic yield strengths of some materials are usually very sensitive to strain-rate, the type of experiment, and heat treatment of materials. This makes it difficult to obtain definite and reproducible experimental measurements. The strength factors in this paper are based on the highest available strain rate.

Computational results

A collection of penetration data for normal impacts against semi-infinite targets published by different researchers from 1961 to 1991 was compiled in a penetration mechanics database by Anderson, et al. (1992b). Using these data, the current model that incorporates Eqs. (2), (10), (11) and (12) has been verified to make accurate predictions for crater diameters and penetration depths for most cases. Some selected results within the impact velocity range between 1 km/s and 4 km/s are shown in Figs. (5)-(8). Figure (5) compares the predicted results of low-strength 1100-O aluminum penetrator against different low-strength steel and aluminum targets. Good agreement has been achieved with the experimental data. The underestimated points can be attributed to the fact that the strength of 1100-O aluminum is more strain-rate sensitive at high impact velocities. Two cases are compared in Fig. (6) for the results of low-strength aluminum (2024-T3) rods and high-strength aluminum (7075-T6) rods impacting on a soft target (1100-O AL). The latter case suffers more deviation at lower velocities, which can be attributed to the errors in transient analysis and the cylindrical crater approximation. For shallow craters, the cylindrical approximation is especially poor. Figures (7) and (8) show good agreement with the experimental data for high-strength rods (4340 hard steel) against high-strength targets (4340 hard steel) as well as high-density rods (D17) against high density targets (D17) and against high-strength steel targets (W8), respectively.

Conclusion

In this paper, a more detailed estimate for the impulse of the external forces acting on a deforming, rigid-plastic penetrator has been made. This result is used in the initial transient analysis introduced by Cinnamon, et al. (1992a, 1992b) and Cinnamon (1992) to produce a new estimate for penetration depth that extends over a wider range of impact velocities than previously reported. A new parameter, called the impulse factor, correlates with the dynamic strengths of the penetrator and target materials. For the most part, the results show reasonable agreement with experimental observations. Figure (9) is an example of an aberrant fit to the experimental data. For very soft targets, like lead, the theory cannot capture the trend for maximum penetration observed by Tate (1969) and others. This is probably due to neglecting the strain-rate dependence on velocity-dependent strength in the target. Future efforts will concentrate on improving the estimate for impulse and utilizing the velocity-dependence of the target strength in the analysis, as observed by Anderson, et al. (1992a).

References

Alekseevskii, V. P., 1966, "Penetration of A Rod into A Target at High Velocity," *Combustion, Explosion, and Shock Waves*, Vol. 2, pp. 63-66.

Anderson, C. E., and Walker, J. D., 1991, "An Examination of Long-Rod Penetration," *International Journal of Impact Engineering*, Vol. 4, pp. 481-501.

Anderson, C. E., Walker, J. D., and Hauver G. E., 1992a, "Target Resistance for Long-Rod Penetration into Semi-Infinite Targets," *Nuclear Engineering and Design*, Vol. 138, pp. 93-104.

Anderson, C. E., Morris, B. L., and Littlefield, D. L., 1992b, *A Penetration Mechanics Database*, SWRI Report 3593/001, Southwest Research Institute, San Antonio, TX.

Cinnamon, J. D., Jones, S. E., House, J. W., and Wilson, L. L., 1992a, "A One-Dimensional Analysis of Rod Penetration," *International Journal of Impact Engineering*, Vol. 12, pp. 145-166.

Cinnamon, J. D., Jones, S. E., Wilson, L. L., and House, J. W., 1992b, "Further Results in The One-Dimensional Analysis of Rod Penetration," *Proceedings of the SECTAM XVI Conference*, Nashville, TN., Vol. II, No. 11, pp. 37-43.

Cinnamon, J. D., 1992, "Further One-Dimensional Analysis of Long-Rod Penetration of Semi-Infinite Targets," master's thesis, The University of Texas at Austin.

Hohler, V., and Stilp, A. J., 1977, "Penetration of Steel and High Density Rods in Semi-Infinite Steel Targets," *Proceeding of The 3rd International Symposium on Ballistics*, Karlsruhe, West Germany.

Hohler, V., and Stilp, A. J., 1980, "Study of The Penetration Behavior of Rods for A Wide Range of Target Densities," *Proceeding of The 5th International Symposium on Ballistics*, Toulouse, France.

Hohler, V., and Stilp, A. J., 1984, "Influence of The Length-to-Diameter Ratio in The Range from 1 to 32 on The Penetration Performance of Rod Projectiles," *Proceeding of The 8th International Symposium on Ballistics*, Orlando, Florida.

Hohler, V., and Stilp, A. J., 1987, "Hypervelocity Impact of Rod Projectiles with L/D from 1 to 32," *International Journal of Impact Engineering*, Vol. 5, pp. 323-331.

Ipson, T. W. and Recht, R. F., 1975, "Ballistic-Penetration Resistance and Its Measurement," *Experimental Mechanics*, Vol. 15, No. 7, pp. 249-257.

Jones, S. E., Gillis, P. P., and Foster, J. C., Jr., 1987, "On the Penetration of Semi-Infinite Targets by Long Rods," *Journal of The Mechanics and Physics of Solids*, Vol. 35, pp. 121-131.

Kerber, M. W., Jones, S. E., Fisher, C. A., and Wilson, L. L., 1992, "Penetration and Cratering of Semi-Infinite Targets by Long Rods," *Proceeding of The 12th International Symposium on Ballistics*, San Antonio, TX.

Tate, A., 1967, "A Theory for The Deceleration of Long Rods after Impact," *Journal of The Mechanics and Physics of Solids*, Vol. 15, pp. 387-399.

Tate, A., 1969, "Further Results in The Theory of Long Rod Penetration," *Journal of The Mechanics and Physics of Solids*, Vol. 17, pp. 141-150.

Tate, A., 1986, "Long Rod Penetration Models--Part II. Extensions to the Hydrodynamic Theory of Penetration," *International Journal of Mechanical Science*, Vol. 28, No. 9, pp. 599-612.

Walker, J. D., and Anderson, C. E., 1992, "A Nonsteady-State Model for Penetration," *Proceeding of The 13th International Symposium on Ballistics*, Stockholm, Sweden.

Wilson, L. L., Foster, J. C., Jones, S. E., and Gillis, P. P., 1989, "Experimental Rod Impact Results," *International Journal of Impact Engineering*, Vol. 8, pp. 15-25.

Wright, T. W., 1981, "Penetration with Long Rods: a Theoretical Framework and Comparison with Instrumented Impacts," ARBRL-TR-02323, US Army Ballistic Research Laboratory, Aberdeen Proving Ground, MD.

Wright, T. W., 1983, "A Survey of Penetration Mechanics for Long Rods," *Computational Aspects of Penetration Mechanics* (edited by Chandra, J. and Flaherty, J. E.), Lecture Notes in Engineering, Springer-Verlag, Berlin-Heidelberg, 3, pp. 85-106
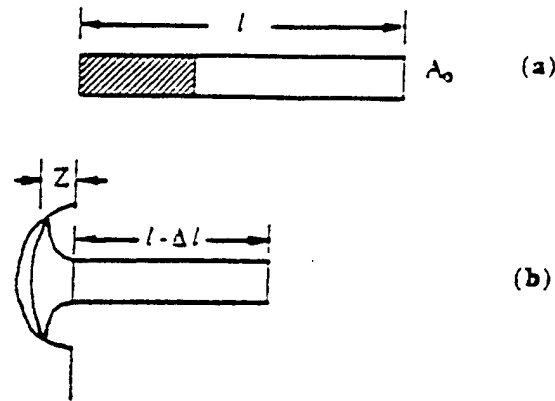
Figure 1. Schematic of rod. (a) Shows plastic portion (shaded area) Δl and undeformed portion $l-\Delta l$. (b) Shows penetration into target to a depth z.
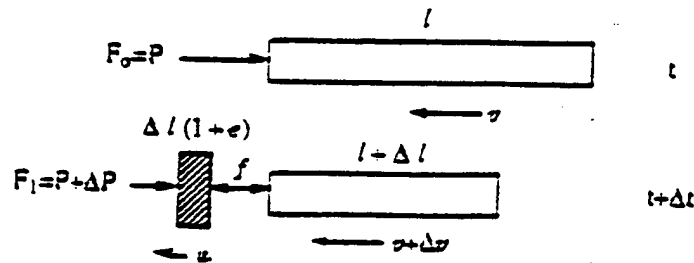
Figure 2. Schematic of the transfer of mass element $\rho A \Delta l$ from the undeformed to the plastic portion of rod during the time interval Δt. The external impulsive force also varies from F_0 to F_1.
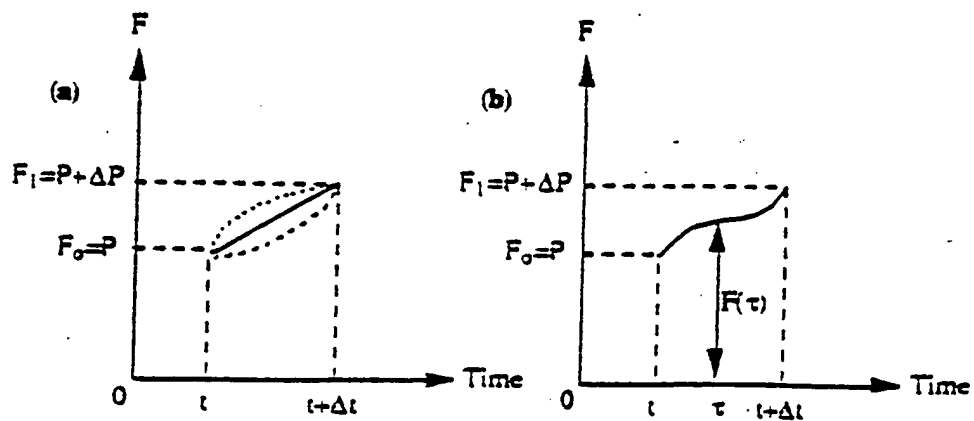
Figure 3. (a) Schematic of a linear and imaginary nonlinear force-time relationship. (b) Schematic of using mean value theorem of integral for an imaginary nonlinear force-time curve.
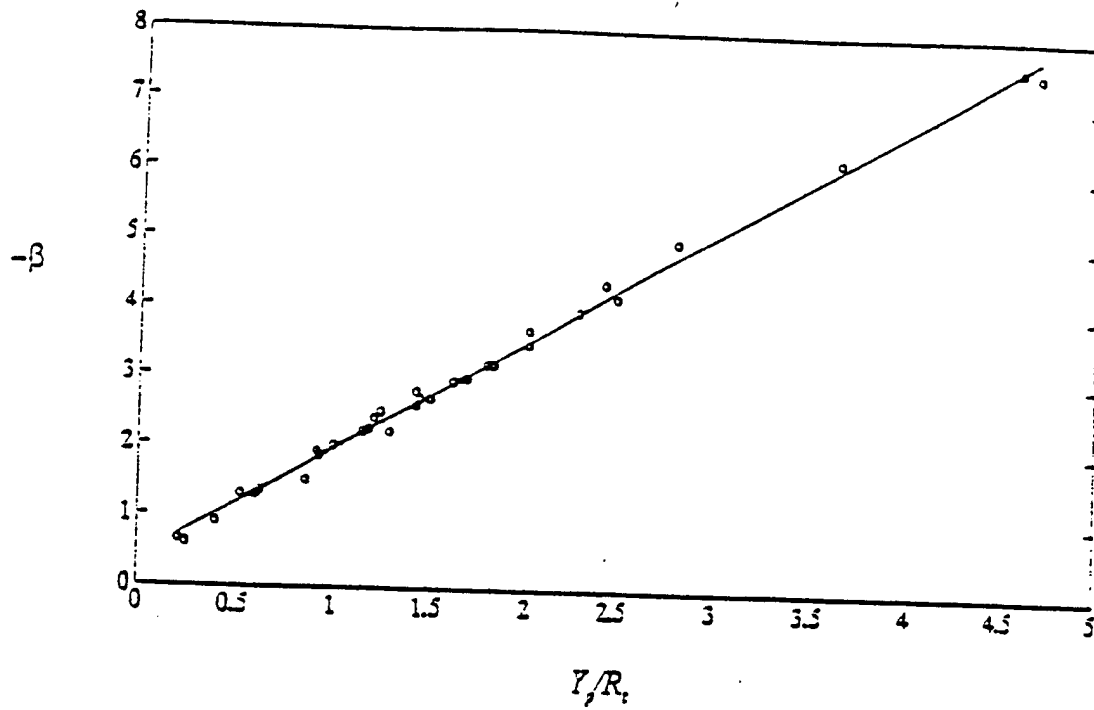
Figure 4. An approximately linear relationship between the β values and the ratios of the penetrator strengths to the target strengths.
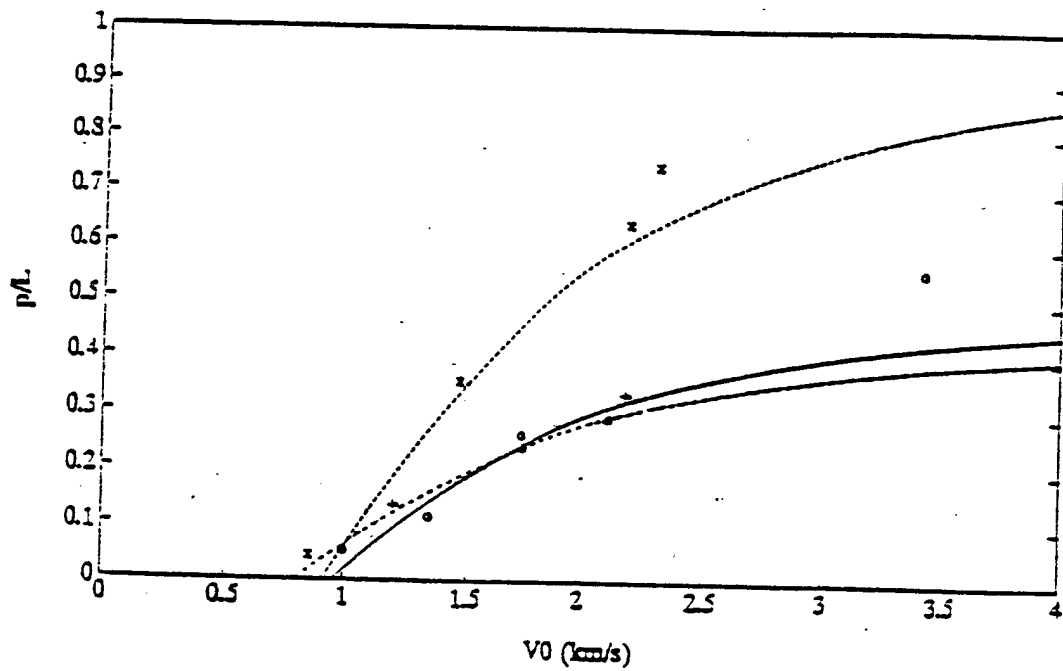
Figure 5. Normalized penetration depth vs. impact velocity
O: experimental data of 1100-O AL on C1015 St; -: current model.
X: experimental data of 1100-O AL on 2024-T3 AL; --: current model
$\div$: experimental data of 1100-O AL on 304 stainless steel; --: current model.
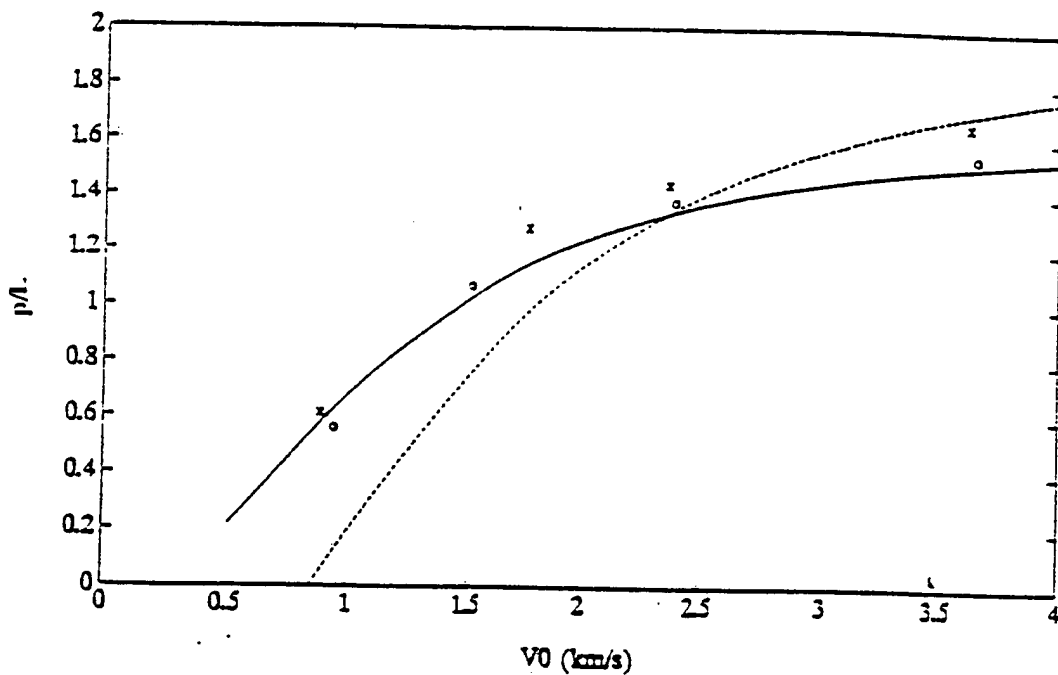
Figure 6. Normalized penetration depth vs. impact velocity
O: experimental data of 2024-T3 AL on 1100-O AL; -: current model.
X: experimental data of 7075-T6 AL on 1100-O AL; --: current model.
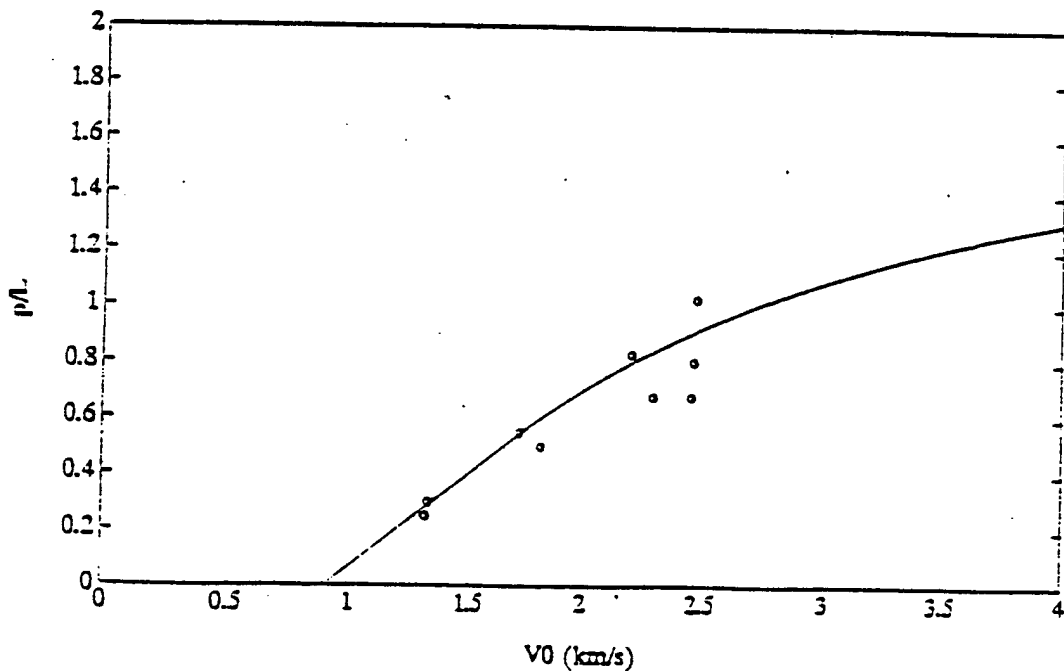
Figure 7. Normalized penetration depth vs. impact velocity
O: experimental data of 4340 hard steel on 4340 hard steel; -: current model.

J-11
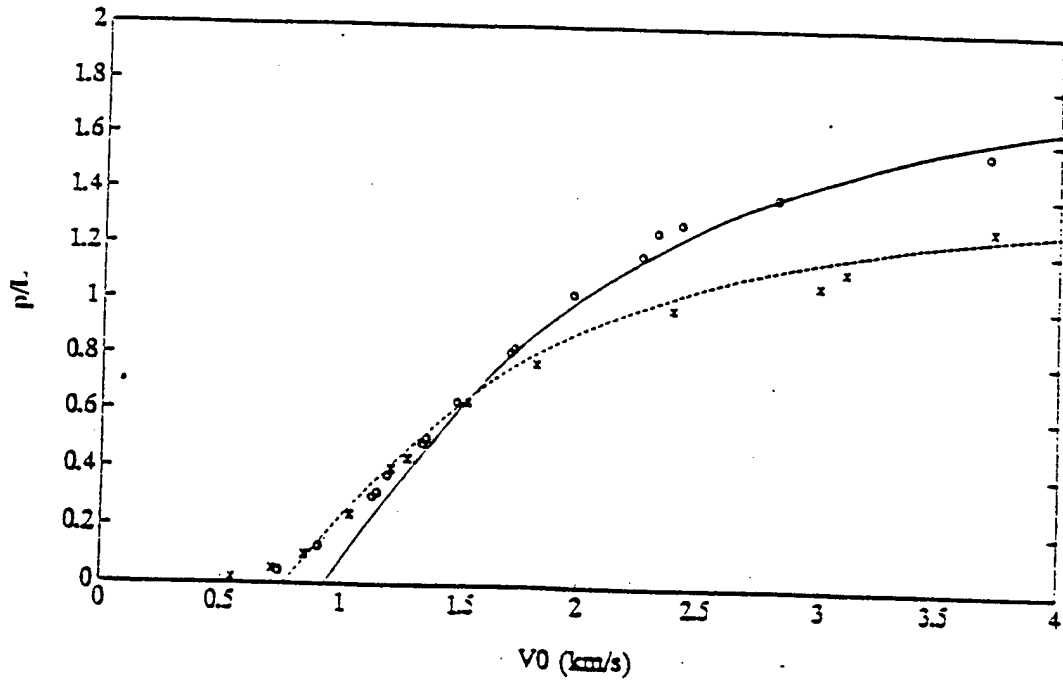
Figure 8. Normalized penetration depth vs. impact velocity
O: experimental data of D17 on W8; -: current model.
X: experimental data of D17 on D17; --: current model.
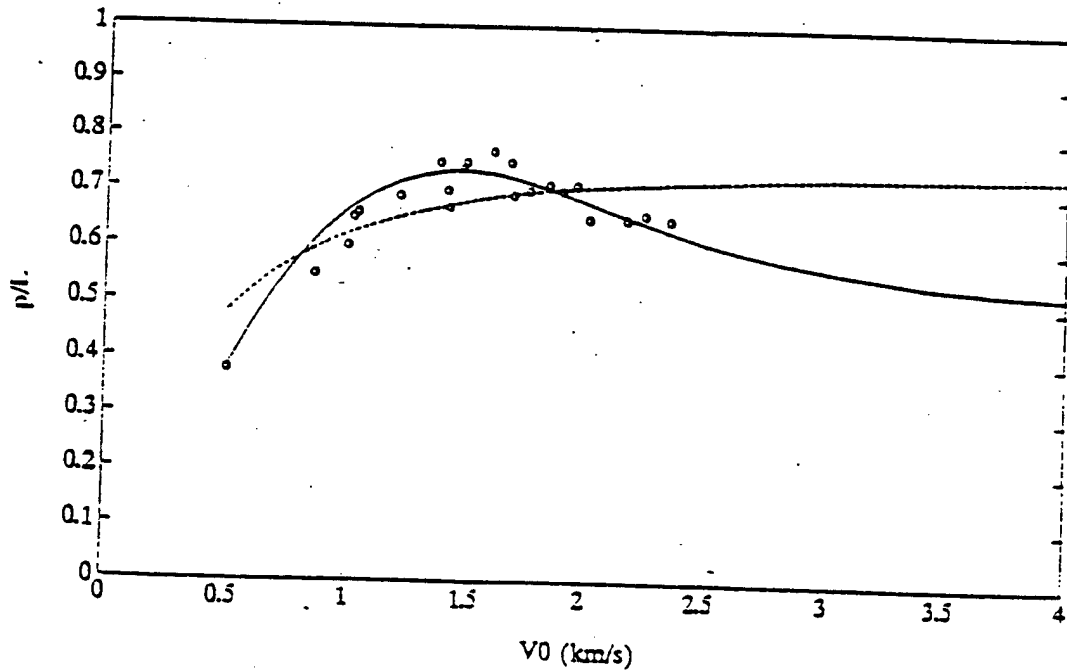
Figure 9. Normalized penetration depth vs. impact velocity
O: experimental data of AL alloy on lead; --: current model.; -: Tate's model

APPENDIX K

A ONE-DIMENSIONAL ANALYSIS OF THE PENETRATION OF SEMI-INFINITE 1100-0 ALUMINUM TARGETS BY RODS

S. E. Jones and Rhett B. Marlow
College of Engineering
The University of Alabama 35487

and

J. W. House and L. L. Wilson
Wright Laboratories, Armament Directorate
Eglin AFB, Florida 32542

ABSTRACT

The one-dimensional analysis of normal rod penetration, recently presented by Cinnamon, et al, 1992, is applied to a very soft target, 1100-0 aluminum. The results are shown to be satisfactory for impact velocities under about 2.5 km/sec. Since the analysis is based on the initial transient stage of penetration, the theory can be applied to impacts by rods with very low L/D ratios. The theory is entirely algebraic and the depths of penetration are predicted from crater volume/kinetic energy curves. To extend the theory to higher velocity impacts, a new distribution of pressure is introduced. These results are promising.

NOTATION

A initial cross-sectional area of the penetrator
a slope of the crater volume-kinetic energy line
b intercept of the crater volume-kinetic energy line
e engineering strain in the mushroom of the penetrator
e_0 engineering strain in the mushroom at impact
e_1 engineering strain in the mushroom at steady state
E_0 kinetic energy of the penetrator at impact
ℓ current undeformed section length
n pressure distribution exponent

P average pressure on the penetrator tip

P_1 average pressure on the penetrator tip at the end of
the transient stage

p pressure distribution on the penetrator tip

P_a pressure on the axis of the penetrator tip

q uniform pressure component

r radial distance from the axis of the penetrator

R radius of the undeformed penetrator

R_t dynamic strength of the target

t time elapsed since impact

u current penetration velocity

u_0 penetration velocity at impact

V_c volume of the crater

v current velocity of the undeformed section

v_0 impact velocity

Y_p dynamic strength of the penetrator

Z penetration depth

α dimensionless constant related to n

β constant related to n with the dimension of MPa

ρ penetrator density

μ^2 ratio of target density to penetrator density

INTRODUCTION

Jones, et al., 1987, presented an alternative formulation of the classic theory of Tate, 1967, and Alekseevskii, 1966, theory for normal penetration of semi- infinite targets by long rods. The new formulation contained a relative velocity term to account for mass loss from the undeformed section and an infinitesimally thin mushroom with an enlarged cross-sectional area. A new equation to account for conservation of mass across the plastic wave front of the penetrator was added by Wilson, et al., 1989. The penetration depths predicted by this theory were shown to be in fairly good agreement with experiment when the mean strain in the mushroom was estimated from the profile diameters of recovered targets. It should be pointed out, at this juncture, that all dynamic material properties were estimated by laboratory tests (e.g., Taylor impact tests, Split Hopkinson Bar tests, etc.) at high strain rates. The results were encouraging. However, there are several defects in the modeling process. One is that the entire penetration process is treated as steady, while the mushroom has constant strain. The constant strain assumption may be appropriate for the steady portion of the penetration process, but not for the entire event. This stimulated Cinnamon, et al., 1992, a, b, to investigate the initial transient stage of penetration. In this case, the initial transient stage shall refer to everything that precedes steady penetration. This includes the shock/impact stage in both the penetrator and the target and the complete mushrooming of the penetrator. By considering the pressure distribution p on the penetrator tip to be nonuniform

$$p = p_a \left(1 - \frac{r^2}{R^2}\right)^n \tag{1}$$

where p_a is the pressure on the rod axis, r/R is the dimensionless radial distance from the axis, R is the undeformed rod radius, and n is a dimensionless exponent, Cinnamon, et al., 1992, a, b, developed a one-dimensional analysis of penetration that was completely algebraic. The pressure distribution in equation (1) is referred to the original configuration of the rod, but is extended over the deformed configuration in the equation of motion by means of the mean mushroom strain, e. The equation of motion for the undeformed section of length ℓ can now be shown to take the form

$$\ell \dot{v} + \dot{\ell}(v - u) = \frac{-p_a}{\rho(n+1)(1+e)} \tag{2}$$

where v is the current velocity of the undeformed section. u is the penetration velocity, and ρ is the density of the penetrator. Dots over symbols denotes differentiation with respect to time t. When equation (2) is coupled with the equation for conservation of mass for the mushrooming material introduced by Wilson, et al [4]

$$e\dot{\ell} = v - u \tag{3}$$

and elementary theory for mushrooming was produced. It was shown that n was basically a function of target strength for the low to intermediate impact velocities, say 1 km/sec to 3 km/sec. Specifically,

$$n = \alpha + \frac{\beta}{R_t} \tag{4}$$

where α and β are constants and R_t is the dynamic strength of the target at a strain-rate appropriate to the penetration event. A good correlation was achieved for $\alpha = 9.2117 \times 10^{-2}$ and $\beta = 1835.117$ MPa. This hypothesis was tested for several target materials in [5]. The targets were: 2024-T4 Aluminum, 7075-T6 Aluminum, and 4340 Steel in hard and annealed states. The penetrators were of the same materials. In Cinnamon, et al., 1992, b, the hypothesis was shown to be valid for OFHC copper, 4340 steel, and tantalum penetrators into rolled homogeneous armor and 4340 steel targets.

The pressure exponent n rapidly increases with decreasing target strength. It is interesting to apply this reasoning to a very soft target, say 1100-0 aluminum.

PENETRATION OF 1100-0 ALUMINUM TARGETS

Christman, et al., 1964, reported penetration data for 1100-0 Aluminum targets. Their data will be used for comparison in this section. A static yield strength for 1100-0 aluminum is approximately 70 MPa. However, for strain-rates appropriate to mushroom formation, 250 MPa is acceptable. For $R_t = 250$ MPa, equation (4) indicates that $n = 7.41$. Figure 1 shows graphically the relationship between

n and target strength for all of the targets considered. Figures 2 and 3 show the engineering strain in the target e_1 when steady state is reached for 2024-T3 aluminum and C1015 steel penetrators. The dynamic yield stresses for the penetrator materials are assumed to be 750 MPa for 2024-T3 aluminum and 1000 MPa for C1015 steel. The strain e_1 has been estimated from [5] by

$$e_1 = \frac{-(v_0 - u_0)^2}{(v_0 - u_0)^2 + \frac{P_1}{\rho(n+1)}} \tag{5}$$

P_1 is the pressure at the initiation of steady penetration that can be estimated by the Modified Bernoulli Equation (e.g., Tate, 1967).

$$P_1 = \frac{1}{2}\mu^2\rho u_0^2 + R_t = \frac{1}{2}\rho(v_0 - u_0)^2 + Y_p \tag{6}$$

In this equation, Y_p is the dynamic strength of the penetrator, v_0 is the impact velocity, u_0 is the penetration velocity during mushroom formation (assumed to be approximately constant), and $\mu^2\rho$ is the target density. These equations can be used to find u_0 in terms of v_0 and the other physical parameters, as well as the pressure P_1.

Penetration depths can be estimated by assuming that the crater in the target is approximately a cylinder whose cross-sectional area can be computed from the engineering strain e_1 in equation (5). Experimental evidence suggests that in the range of impact velocities in question, the relationship between crater volume V_c and kinetic energy on impact E_0 is approximately linear.

$$V_c = aE_0 + b \tag{7}$$

This means that the penetration depth z can be estimated from

$$z = \frac{1}{A}(1 + e_1)V_c = \frac{1}{A}(1 + e_1)(aE_0 + b) \tag{8}$$

where A is the original cross-sectional area of the rod penetrator. The constants a and b are determined experimentally. Figures 4 and 5 show the penetration depth curve predicted by equation (7) for 2024- T3 aluminum and C1015 steel penetrators. The results are good up to impacts of about 2.5 km/sec. They deteriorate rapidly at velocities higher than that. This is partly due to the simple pressure distribution presented in equation (1). In the next section, we introduce a more general pressure distribution.

A DIFFERENT DISTRIBUTION OF PRESSURE

Following a suggestion made by Anderson, 1991, we consider an alternative form for the pressure distribution in equation (1). A uniform component q is added to the variable distribution in equation (1). The new distribution has the form

$$p = q + (p_a - q)\left(1 - \frac{r^2}{R^2}\right)^n \tag{9}$$

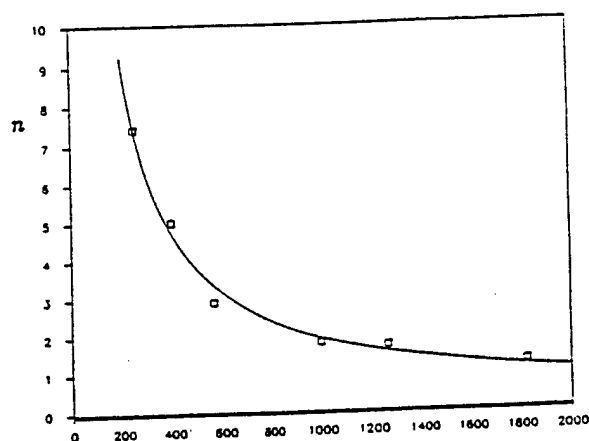Fig. 1. n vs. target strength R (MPa). The relationship between them is approximately given by $n = 8.544 \times 10^{-2} + 1830 / R$. $\square$ denotes a fit to experimental data.
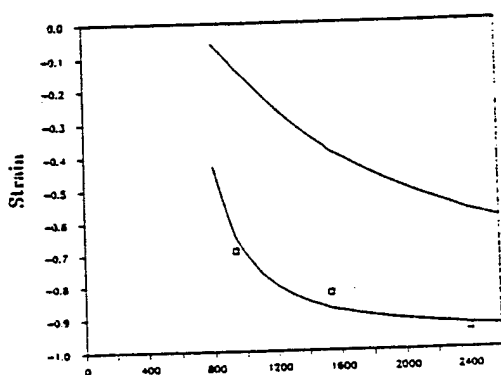

Fig. 2. Strain vs. impact velocity (m/s) for 2024-T3 Al (750 MPa) penetrators against 1100-0 Al (250 MPa) targets. $\square$ denotes experimental data points. e_1 (lower solid curve) is the predicted strain at the beginning of steady state and e_0 (upper solid curve) is the predicted strain at impact.
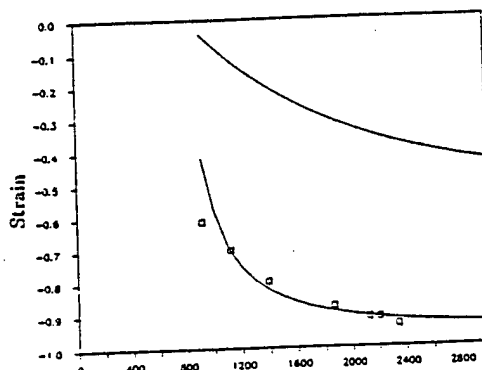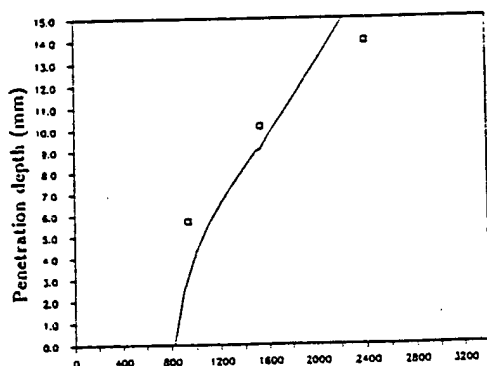

Fig. 3. Strain vs. impact velocity (m/s) for C 1015 st. (1000 MPa) penetrators against 1100-0 Al (250 MPa) targets. $\square$ denotes experimental data points. e_1 (lower solid curve) is the predicted strain at the beginning of steady state and e_0 (upper solid curve) is the predicted strain at impact.

Fig. 4. Penetration depth (mm) vs. impact velocity for 2024-T3 Al penetrators impacting 1100-0 Al targets. $\square$ denotes experimental data points for L/D=3 penetrators. The solid curve is a prediction based on the crater volume/kinetic energy relationship.
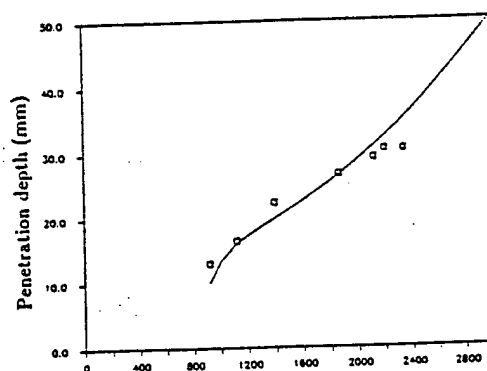
Fig. 5. Penetration depth (mm) vs. impact velocity (m/s) for C 1015 st. penetrators impacting 1100-0 Al targets. $\square$ denotes experimental data points for L/D=3 penetrators. The solid curve is a prediction based on the crater volume/kinetic energy relationship.

where p_a is the total pressure on the axis of the penetrator. Now, the average pressure P which appears in the equation of motion of Jones, et al [1], is easily shown to be

$$P = \frac{1}{A} \int_A p \, dA = \frac{nq}{n+1} + \frac{p_a}{n+1} \tag{10}$$

where A is the undeformed cross-sectional area of the penetrator. Using equation (10) for the average pressure revises the equation of motion for the undeformed section into the form

$$\ell \dot{v} + \dot{\ell}(v - u) = \frac{-1}{\rho(1+e)(1+n)}(nq + p_a) \tag{11}$$

This equation, coupled with equation (3), given a new system from which we can estimate the initial transient behavior of the penetrator in terms of two parameters, n and q. It should be noted, however, that n will no longer have the simple interpretation afforded by equation (4).

THE INITIAL TRANSIENT STAGE

Equations (3) and (11) can be used to estimate the initial transient behavior of the penetrator when suitable assumptions are made about the velocity of the undeformed section v and the penetration velocity u. Equation (5) was developed by Cinnamon, et al., 1992, a, by assuming that $v \approx v_0$ and $u \approx u_0$ (const.) during the mushrooming of the penetrator. These assumptions force equations (3) and (11) to take the form

$$e\dot{\ell} = v_0 - u_0 \tag{12}$$

and

$$\dot{\ell}(v_0 - u_0) = \frac{-1}{\rho(1+e)(1+n)}(nq + p_a) \tag{13}$$

When $\dot{\ell}$ is algebraically eliminated between these equations, we get a single equation for the mushroom strain, e.

$$e = \frac{-\rho(n+1)(v_0 - u_0)^2}{\rho(n+1)(v_0 - u_0)^2 + p_a + nq} \tag{14}$$

This equation expresses e in terms of the time- dependent pressure p_a, the uniform pressure component q, and the parameter n. The uniform pressure q could vary with time, but for this analysis we will assume that it is constant.

Equation (14) is valid throughout the mushrooming stage. At the transition point between mushrooming and steady state, we assume that the Modified Bernoulli Equation (6) applies. This suggests that equation (14) should reduce to

$$e_1 = \frac{-\rho(n+1)(v_0 - u_0)^2}{\rho(n+1)(v_0 - u_0)^2 + P_1 + nq} \tag{15}$$

and P_1 is taken from equation (6).

The two parameter strain equation (15) is used to match experimental data at high and low velocities. The parameters q and n are then determined algebraically. For C1015 steel penetrators impacting 1100-0 aluminum targets, the results are shown in Figure 6. In this instance, $n = 15.14$ and $q = 105.17$ MPa. The estimates for penetration depth using equation (8) are shown in Figure 7. They are somewhat disappointing, because even a slight variation in strain at percentages as high as those given in Figure 6, can produce considerable discrepancy in the penetration depth predicted by equation (8).

The two parameter strain equation was also applied to some of the cases for which only low velocity data was available. The results for hard 4340 steel penetrators impacting hard 4340 steel targets are shown in Figures 8 and 9. In this case, $n = 3.07$ and $q = 344.8$ MPa. For annealed 4340 steel penetrators impacting annealed 4340 steel targets, the results are shown in Figures 10 and 11. In this instance, $n = 2.58$ and $q = 705.89$ MPa.

Figures 12 and 13 show the results of tungsten (W10) penetrators impacting RHA targets at velocities between 1 km/sec and 3km/sec. The experimental comparison is taken from Silsby, 1984. For this comparison, $n = 8.42$ and $q = 1790$ MPa.

CONCLUSIONS

The results of Cinnamon, et al., 1992, a, have been extended to the penetration of 1100-0 aluminum targets. For lower impact velocities, say those under 2.5 km/sec, the correlation of pressure exponent n in equation (1), predicted by equation (4), produces very reasonable results. However, for higher impact velocities the results deteriorate rapidly. To accommodate higher velocities, the pressure was generalized in equation (9) and the strain at steady state e_1 was shown to correlate very well with independently reported experimental results [7] for two penetrators impacting 1100-0 aluminum targets. The penetration depth predictions using the elementary algebraic method introduced by Cinnamon, et al., 1992, a, are somewhat disappointing. However, this is understandable. At very large strains, even minor deviations from the experimental results will produce significant deviations in the cross-sectional area of the crater. As a result, equation (8) will produce estimates that differ from experiment. Such differences are not as visible at low velocities because the strains are smaller in magnitude. Future efforts will be directed toward improvement in this area. Future efforts will also center on other forms for the pressure distribution in equation (9). Some progress has already been made in the area.

A project of some interest to us is the physical interpretation of n and q. For the simple pressure distribution in equation (1), a low velocity interpretation can be provided by equation (4). However, for $q = 0$ and velocities higher than about 3 km/sec., n does not have this interpretation. It remains to be seen whether a
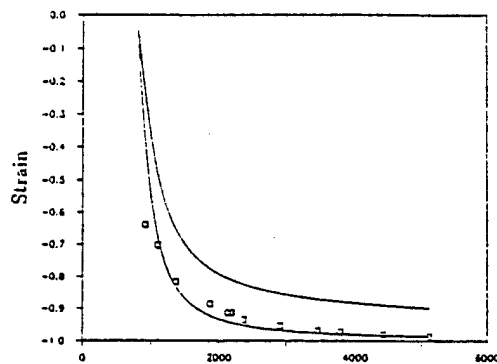
Fig. 6. Strain vs. impact velocity (m/s) for C 1015 st. (1000 MPa) penetrators against 1100-0 Al (250 MPa) targets. ☐ denotes experimental data points. e_1 (lower solid curve) is the predicted strain at the beginning of steady state and e_o (upper solid curve) is the predicted strain at impact.
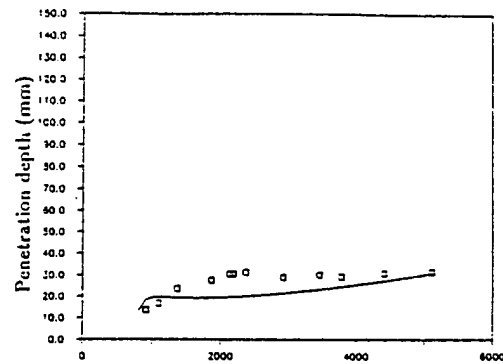

Fig. 7. Penetration depth (mm) vs. impact velocity (m/s) for C 1015 st. penetrators impacting 1100-0 Al targets. ☐ denotes experimental data points for L/D=3 penetrators. The solid curve is a prediction based on the crater volume/kinetic energy relationship. The disparity noted for the intermediate velocities is caused by small deviations in the predicted strain which can result in large deviations in the predicted cross-sectional area of the crater.
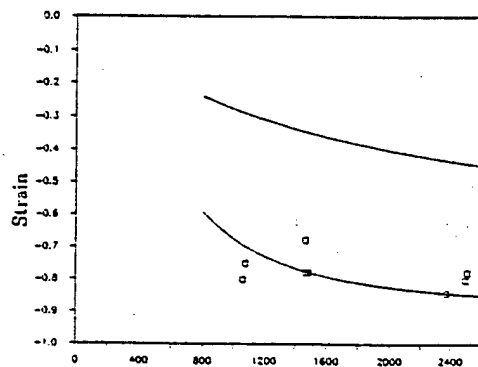
Fig. 8. Strain vs. impact velocity (m/s) for hard 4340 st. (1825 MPa) penetrators against hard 4340 st. (1825 MPa) targets. ☐ denotes experimental data points. e_1 (lower solid curve) is the predicted strain at the beginning of steady state and e_o (upper solid curve) is the predicted strain at impact.

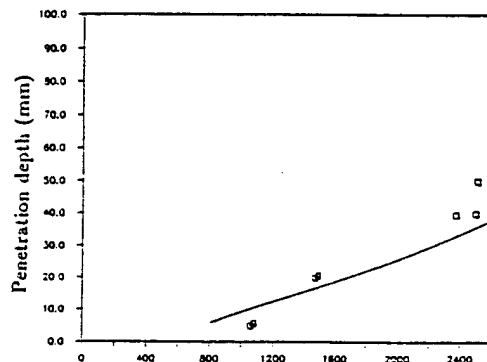
Fig. 9. Penetration depth (mm) vs. impact velocity (m/s) for hard 4340 st. penetrators impacting hard 4340 st. targets. ☐ denotes experimental data points for L/D=10 penetrators. The solid curve is a prediction based on the crater volume/kinetic energy relationship.

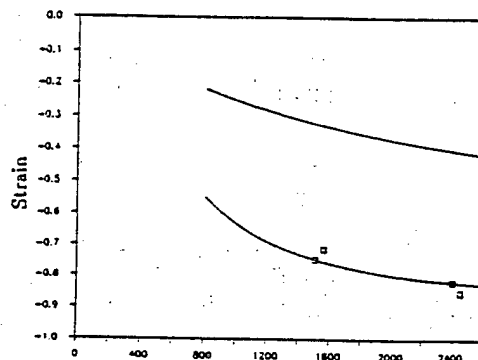
Fig. 10. Strain vs. impact velocity (m/s) for annealed 4340 st. (1263 MPa) penetrators against annealed 4340 st. (1263 MPa) targets. ☐ denotes experimental data points. e_1 (lower solid curve) is the predicted strain at the beginning of steady state and e_o (upper solid curve) is the predicted strain at impact.
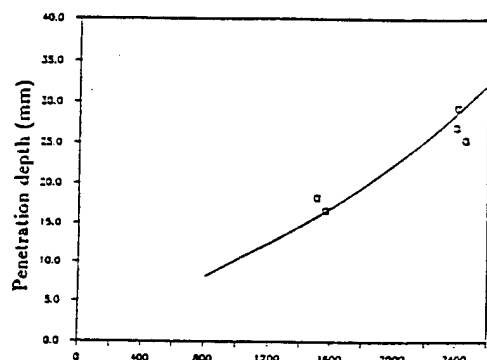

Fig. 11. Penetration depth (mm) vs. impact velocity (m/s) for annealed 4340 st. penetrators impacting annealed 4340 st. targets. ☐ denotes experimental data points for L/D=5 penetrators. The solid curve is a prediction based on the crater volume/kinetic energy relationship.

K-8
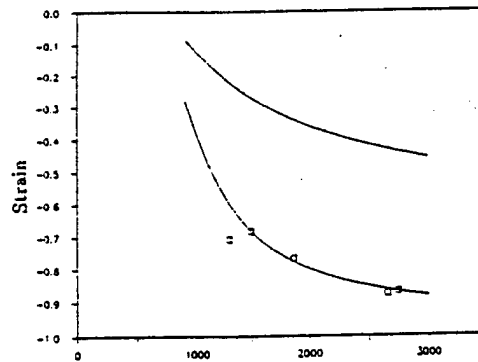
Fig. 12. Strain vs. impact velocity (m/s) for tungsten
W 10 (2500 MPa) penetrators against RHA (1000
MPa) targets. ☐ denotes experimental data points.
e_1 (lower solid curve) is the predicted strain at the
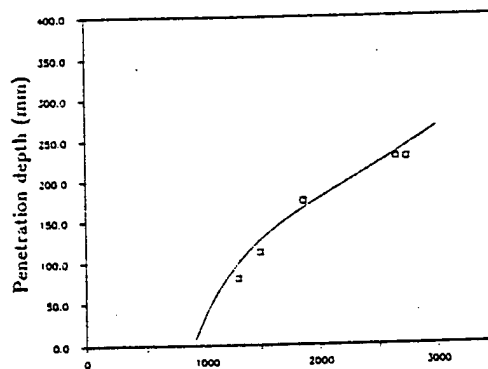beginning of steady state and e_o (upper solid curve) is
the predicted strain at impact.

Fig. 13. Penetration depth (mm) vs. impact velocity
(m/s) for Tungsten W 10 penetrators impacting RHA
targets. ☐ denotes experimental data points for
L/D=3 penetrators. The solid curve is a prediction
based on the crater volume/kinetic energy relationship.

K-9

APPENDIX L

AN ELEMENTARY THEORY OF ONE-DIMENSIONAL ROD PENETRATION
USING A NEW ESTIMATE FOR PRESSURE

P. Wang and S. E. Jones

Department of Engineering Science and Mechanics
University of Alabama, Tuscaloosa, AL 35487

ABSTRACT

A re-examination is made of the one-dimensional eroding-mushrooming rod penetration model proposed by Jones, et al. in 1987. The original equation of motion is decomposed into two parts to account for the motions of the mushroom region and undeformed portion of the penetrator separately. As a result of incorporating these two equations with the kinematic equation derived by Wilson, et al. in 1989, a new pressure law is proposed to replace the modified Bernoulli equation of Tate. This new estimate for pressure, taking the effect of mushroom strain in the penetrator tip into account, gives more physical insight into the interaction between the pressure and the penetrator during penetration.

Two different attempts are made to investigate the validity of the proposed pressure law. In the first case, the pressure is assumed velocity-independent and a new current velocity-penetration velocity relationship is constructed. Direct integration of the system leads to a closed form solution for the penetration depth. The constant pressure is obtained by matching the penetration depth and then further correlated to the target strength. The predicted results are fairly accurate in high velocity range.

In the second case, a velocity-dependent pressure with a shape factor is considered. Numerical integration is required to obtain the penetration depths. The shape factor is obtained by matching the penetration depths and can be hyperbolically correlated to the strain. The results from some typical calculations are shown in Fig. 1. Realistic estimates for material strengths have been used.
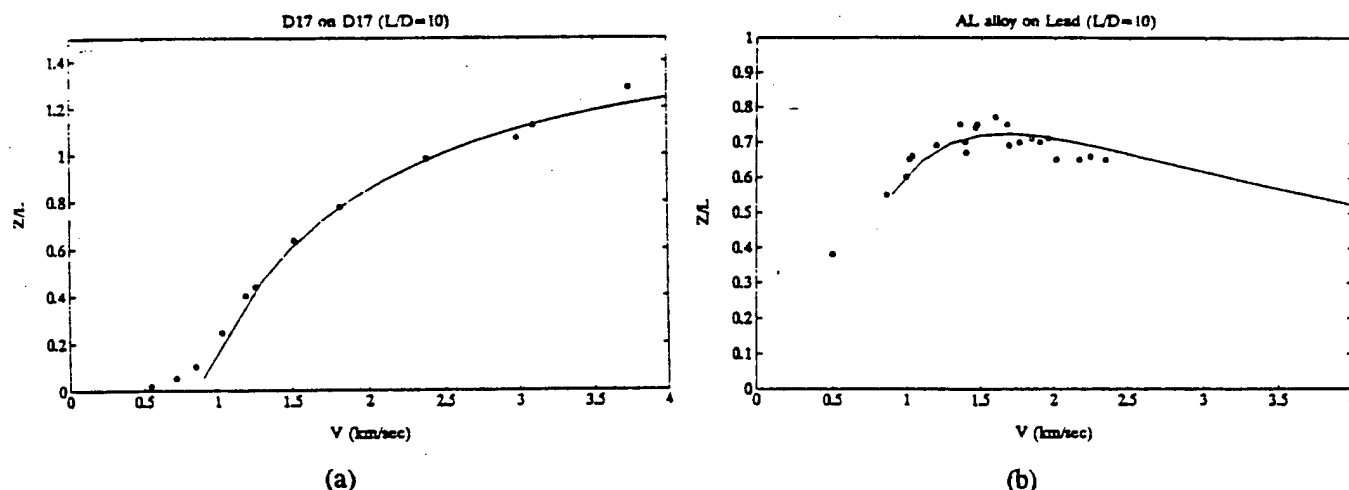
(a)

(b)

Figure 1. Normalized penetration (Z/L) depth vs. impact velocity (V). Circles represent the experimental data and the solid curve, the theoretical prediction. (a) Y=R=1600 MPA. (b) Y=275 MPA, R=60 MPA.

DISTRIBUTION LIST FOR TECHINAL REPORT AFRL-MN-EG-TR-1998-7044

Defense Technical Information Center (1)
ATTN: DTIC-OCA (Acquisitions)
8725 John Kingman Road, Suite 0944
Ft. Belvior, VA 22060-6218

AFRL/CA-N (1)

AFRL/MNMW (4)

AFRL/MNOC
Technical Library (1)

AFRL/MN0R
Case File (1)

Dr. S. E. Jones
University of Alabama
Department of Aerospace Engineering and Mechanics
Tuscaloosa, AL 35487-0280

Dr. P. P. Gillis
University of Kentucky
Department of Chemical and Material Science Engineering
177 Anderson Hall
Lexington, KY 40506-0046